Control of the Electron Energy Distribution and Plasma Ignition Delay in a Novel Dual Tandem Inductively Coupled Plasma

A Dissertation

Presented to

the Faculty of Department of Chemical & Biomolecular Engineering

University of Houston

In Partial Fulfillment

of the Requirements for the Degree

Doctor of Philosophy

in Chemical Engineering

By

Lei Liu

August 2016

Control of the Electron Energy Distribution and Plasma Ignition Delay in a Novel Dual Tandem Inductively Coupled Plasma

Lei Liu

Approved:

Co-Chair of the Committee
Vincent M. Donnelly, Professor,
Chemical & Biomolecular Engineering

Co-Chair of the Committee
Demetre J. Economou, Professor,
Chemical & Biomolecular Engineering

Committee Members:

William Epling, Professor,
Chemical & Biomolecular Engineering

Paul Ruchhoeft, Associate Professor,
Electrical & Computer Engineering

Lee Chen, Senior Member of Technical
Staff, Tokyo Electron Ltd.

Suresh K. Khator, Associate Dean,
Cullen College of Engineering

Michael P. Harold, Professor and Chair of
Chemical & Biomolecular Engineering

ACKNOWLEDGMENTS

First and foremost, I must thank my advisors Dr. Vincent M. Donnelly and Dr. Demetre J. Economou. I was fortunate enough to have had the opportunity to work in Plasma Processing Laboratory at University of Houston (UH) under the direction of them. They led me into the world of plasma processing and taught me how to think critically. They also provided me a lot of opportunities to interact with scientists in academia and industry. Their profound knowledge and enthusiasm in learning new disciplines have always inspired me. This work would not have been accomplished without their continued support, guidance, and encouragement in the past five years.

I must also thank Dr. William Epling, Dr. Paul Ruchhoeft and Dr. Lee Chen for serving on my thesis committee and for reviewing this manuscript.

I think one of the most important reasons for my success at UH is the support I have received from other members in my group. I especially would like to thank my coworker, Shyam Sridhar, for the great teamwork we have made. Shyam has become a particularly good friend through frequent dinners, movies and conference trips to Austin, Maryland, Baltimore, and Princeton. I am also thankful to other former and present group members of our lab: Dr. Hyungjoo Shin, Dr. Zuo Chen, Dr. Weiye Zhu, Dr. Se Youn Moon, Dr. Erdinc Karakas, Dr. Siyuan Tian, Dr. Ashutosh Srivastava, Dr. Vladimir Samara, Dr. Yongxin Liu, Dr. Wen Yan, Sanbir Kaler, Qiaowei Lou, Tianyu Ma, Tyler List, Eduardo Hernández, Hanyang Li, Emilia Hirsch, Yamin Chen, Tam Nguyen, Arthur Hernandez, Ryan Sawadichai, and anyone I may have forgotten.

I would like to express my sincere appreciation to our collaborators Dr. Mark Kushner and Dr. Michael Logue from University of Michigan for their great work in simulating our experiments.

I'm grateful to our excellent former and present machinists, Mr. John Costales, Mr. Mitchell Hawkins, and Mr. Gerald Blosser for their perfect work that helps me with setting up my experimental apparatus. I would also like to thank the staff of the Department of Chemical and Biomolecular Engineering for their kind assistance.

Finally and most importantly, I like to thank my parents for their enormous support and love. This work would not have been possible without them.

Dedicated to

my father, Mr. Jun Liu (刘军)

and my mother, Mrs. Lihua Zhou (周丽华)

"谁言寸草心， 报得三春晖。"

——孟郊《游子吟》

Control of the Electron Energy Distribution and Plasma Ignition Delay in a Novel Dual Tandem Inductively Coupled Plasma

An Abstract

of a

Dissertation

Presented to

the Faculty of Department of Chemical & Biomolecular Engineering

University of Houston

In Partial Fulfillment

of the Requirements for the Degree

Doctor of Philosophy

in Chemical Engineering

By

Lei Liu

August 2016

Abstract

The electron energy distribution function (EEDF) plays an essential role in non-equilibrium low-temperature plasmas. The EEDF governs the rate of electron-impact reactions and determines the plasma gas composition, which in turn, determines the fluxes of radicals, ions, and photons striking the substrate. As such, control of the EEDF is of paramount importance for both fundamental plasma studies and practical applications.

A novel dual plasma source was developed to control the EEDF in a main inductively coupled plasma (ICP) separated by a grid from a tandem auxiliary ICP. The auxiliary ICP was continuously powered while the main ICP power was pulsed. Langmuir probe measurement of the EEDFs during the afterglow of the main ICP, suggested that transport of hot electrons from the auxiliary plasma kept the tail of the EEDF and bulk electron temperature elevated. Results from a computer simulation of the trends in the evolution of the EEDFs agreed with experimental measurements.

For certain operating conditions, plasma ignition delays were observed in the main ICP. Power to the Faraday-shielded main ICP was pulsed with a frequency of 1 kHz, while the (also Faraday shielded) auxiliary ICP was operated in continuous wave (cw) mode. In chlorine plasmas, ignition delay was observed for duty cycles greater than 60% and, in contrast to expectation, the delay was longer with increasing duty cycle up to ~99.5%. The ignition delay could be varied by changing the auxiliary and/or main ICP power. Langmuir probe measurements provided the temporal evolution of electron temperature, and electron and positive ion densities. These measurements revealed that

the plasma that was ignited shortly after the decaying positive ion density (n_+) in the afterglow of the main ICP, reached the density ($n_{+,aux}$) prevailing when only the auxiliary ICP was powered. At that time, the production rate of electrons dominated their loss in the main ICP due to hot electron injection from the auxiliary ICP. As a result, n_e increased rapidly and the plasma was ignited. Plasma ignition delay occurred when the afterglow of the pulsed plasma was not long enough for the ion density to reach $n_{+,aux}$ during the afterglow. Besides Cl_2, plasma ignition delays were also observed in other electronegative gases (SF_6, CF_4/O_2 and O_2) but not in an electropositive gas (Ar).

Table of Contents

Acknowledgment iv

Abstract viii

Table of Contents x

List of Figures xiv

List of Tables xxiii

CHAPTER 1 1

INTRODUCTION 1

1.1 Etching technologies in semiconductor industry 1

1.1.1 Plasma etching 1

1.2 Critical roles of electron and ion energy distribution in plasma etching 3

1.3 Pulsed plasmas 5

1.4 Objective of this research 7

CHAPTER 2 9

LITERATURE REVIEW 9

2.1 Control of electron energy distribution function (EEDF) 9

2.2 Control of the ion energy distribution (IED) 20

2.3 Dynamics of pulsed plasma 26

2.4 Applications of pulsed plasma 34

2.4.1 Control of plasma chemistries 34

2.4.2 Extraction of negative ions in pulsed electronegative plasma 39

2.4.3 Atomic layer etching (ALE) 43

2.5 Plasma ignition delay 50

CHAPTER 3 51

EXPERIMENTAL SETUP 51

3.1 Plasma source 51

3.2 Operating conditions 53

3.2.1 Operating conditions for controlling EEDF in continuous wave Ar plasma 53

3.2.2 Operating conditions for controlling the EEDF in pulsed Ar plasma 54

3.2.3 Operating conditions for studying ignition delay in pulsed electronegative plasmas 54

3.3 Plasma diagnostics 55

3.3.1 Langmuir probe 55

3.3.2 Optical emission spectroscopy 57

CHAPTER 4 59

SYNERGISTIC BEHAVIOR OF DUAL TANDEM INDUCTIVELY COUPLED PLASMAS OPERATED IN A CONTINUOUS WAVE MODE 59

4.1 Spatial distribution of plasma potential (V_p) 59

4.2 Spatial distribution of plasma density 61

4.3 Spatial distribution of electron temperature (T_e) 64

4.4 Spatial distribution of EEPFs 64

4.5 Hysteresis of ion current with bias on boundary electrode 67

CHAPTER 5 69

EXTERNAL CONTROL OF THE ELECTRON ENERGY DISTRIBUTION USING DUAL TANDEM INDUCTIVELY COUPLED PLASMAS 69

5.1 External control of electron temperature T_e and electron density n_e 69

5.2 External Control of EEPF 71

CHAPTER 6 77

IGNITION DELAY OF A PULSED INDUCTIVELY COUPLED PLASMA (ICP) IN TANDEM WITH AN AUXILIARY ICP 77

6.1 Ignition delay vs. duty cycle in chlorine plasmas 81

6.2 Ignition delay vs. main and auxiliary ICP power 92

6.3 Effect of grid hole size on ignition delay 93

6.4 Ignition delays in other electronegative gas plasmas 96

CHAPTER 7 100

CONCLUSIONS AND FUTURE WORK 100

7.1 Summary and Conclusions 100

7.2 Recommendations for Future Work 102

7.2.1 New experimental dual tandem plasma reactor 102

7.2.2 Langmuir probe measurements in the auxiliary ICP 103

7.2.3 Dual biasable grids 104

Reference 105

APPENDICES 132

List of Figures

Figure 1.1 Scaling trend of the gate length of high-performance logic transistors [13]... 3

Figure 1.2 Schematic of pulsed plasma [38]... 6

Figure 1.3 Schematics of four kinds of pulsed plasma [38]. 7

Figure 2.1 A qualitative picture of the EEPFs estimated from a combination of Langmuir probe and trace rare gas optical emission spectroscopy (TRG-OES) measurements of electron temperature at (a) 10 mTorr and (b) 3.5 mTorr for the ICP and UHF plasma [56].. 11

Figure 2.2 EEPF evolution with argon pressure in a CCP at 13.56 MHz [57]............. 13

Figure 2.3 EEDFs at different times during the pulse cycle, shown in the bottom figure: (a) Near the higher frequency sheath, (b) in the bulk plasma and (c) near the lower frequency sheath. Averaged EEDF over one pulse period and under CW excitation are shown in the right column [58]..................................... 15

Figure 2.4 Time evolution of the calculated EEPF at the discharge center. Time t = 0 refers to the start of the active glow (plasma ON). A Maxwellian distribution would be a straight line on this plot [59]. 16

Figure 2.5 EEPFs for different times during the afterglow of a 10 mTorr Cl2 plasma. Open symbols denote the case with no bias; closed symbols denote the case with RF bias (70 W) on the substrate electrode. A Maxwellian distribution would be a straight line on this plot [60]. 17

Figure 2.6 Experimental setup with the chamber divided by a grid [62]. 18

Figure 2.7 Measured EEDFs as a function of grid bias [62]. 19

Figure 2.8 Selectivity of SiO_2/Si etching in a CHF_3(20 sccm)/H_2(5 sccm) plasma for three bias voltage wave forms: 5 and 20 MHz sinusoidal, and tailored. The dashed lines indicate the average bias voltage corresponding to the etching threshold for SiO_2 [70]. 21

Figure 2.9 Particle in cell (PIC) simulation results showing IEDs of helium ions hitting the target electrode of RF discharges driven at frequencies from 1 MHz to 100 MHz [79]. 22

Figure 2.10 (a) Model predicted pulse-averaged ion energy distributions. (b) Experimentally measured average ion energy distribution [83].................. 24

Figure 2.11 (a) Predicted energy distribution of extracted ions for different DC bias potentials applied in the afterglow [42]. (b) Experimental data of for the same conditions as in the simulation (FWHM=full width at half maximum) [23]. 25

Figure 2.12 Time evolution of plasma density, electron temperature, and excited atom (4s and 4p) densities for different periods t for a time-average power of 500 W and a duty ratio of 25%: (a) t=10 μs; (b) t=100 μs; (c) t=1000 μs [91]........ 28

Figure 2.13 Time dependent electron density in an argon plasma as a function of (a) duty cycle, (b) peak RF power, and (c) pulse repetition frequency. In all cases, the pressure was 20 mTorr [98].. 29

Figure 2.14 Time evolution of species densities and electron temperature predicted by a pulsed plasma model in chlorine. Only the major ion Cl_2^+ density is shown (Cl^+ is not included) [99]. 32

Figure 2.15 Predictions of a model of a pulsed CCP chlorine plasma. (top) Space and time evolution of the negative-ion Cl^- density during the first 20 μs of the active glow. (bottom) Space and time evolution of negative ion and electron densities during the first 20μs of the afterglow [99]. 33

Figure 2.16 Variation of poly-Si and SiO_2 etching rates with pulse interval for a constant 50% duty cycle [138]... 35

Figure 2.17 F/CF_2 radical density ratio in pulsed CHF_3, C_2F_6 and C_3F_8 plasmas as a function of pulse width for a constant 10 μs pulse interval [139]. 36

Figure 2.18 (a) The absolute CF_x density and the relative F density, and (b) the normalized density ratio CF_x/F as a function of the RF-on time. $T_{off} = \infty$ corresponds to the continuous mode. The measurements were done at the position 12.5 cm above substrate [140]. 37

Figure 2.19 Etch rates of SiO_2 and Si and the selectivity as a function of (a) RF-on time for $T_{off} = 15$ μs and (b) RF-off time for $T_{on} = 20$ μs. P = 0.76 kW, 10 mTorr of 50% CF_4/50% H_2, V_{dc}=2400 V, z=9 cm, and T_w=100 °C [140]............. 38

Figure 2.20 Temporal dynamics of electron temperature and electron density in (a) absence of bias and (b) presence of bias in Cl_2 ICP plasma. Sheath heating during the late after-glow leads to a capacitive discharge with higher electron temperature [113]. 41

Figure 2.21 Mass spectrometer signals for (a) Cl_2^+ and Cl^-, and (b) applied bias voltage measured in a 1 mTorr, 5 sccm Cl_2 ICP plasma. The bias operates at an excitation frequency of 20 kHz with a peak voltage of 225 V [152]. 42

Figure 2.22 Schematic of the ALET process. The filled circles represent Cl atoms; the open circles represent Si atoms, and + represent Ar^+ ions [156]................. 44

Figure 2.23 Schematic of the fast ALET process with pulse plasma and pulsed bias [100, 108].. 46

Figure 2.24 Etching depth per cycle (EPC) for silicon (open circles) and silicon oxide (solid circles) as a function of RF bias [162]. 47

Figure 2.25 Selectivity of single crystal silicon to thermal silicon oxide as a function of RF bias voltage. ALE results (full circles) and continuous process results (open circles) are compared [162]. 47

Figure 2.26 Example of thickness evolution during eight cycles of a SiO_2 ALE process [163]. 48

Figure 2.27 Thickness changes of SiO_2 during one cycle for two thicknesses of deposited FC layer achieved by changing the C_4F_8 pulse time from (a) 1.5 s to (b) 3 s. The FC pulse is injected at the beginning of the deposition step. Bias is applied Eight seconds after the pulse ends [163].. 49

Figure 2.28 Thickness removal during the cycle as determined by ellipsometry for ALE of Si and SiO_2 using C_4F_8 and CHF_3 at 25 eV ion energy and 40 s etching step length [164]. 49

Figure 3.1 Schematic of the experimental apparatus with dual tandem inductively coupled plasma (ICP) sources. The auxiliary (upper) ICP is separated from the main (lower) ICP by a metal grid... 53

Figure 4.1 The plasma potential (V_p) profile along z axis in the main ICP chamber with/without 90 V boundary electrode bias for main ICP only (500 W) and both ICPs on (auxiliary ICP power 100 W) at the pressure of 10 mTorr. (a): 0V bias. (b): 90V bias. 60

Figure 4.2 The electron density (n_e) profile along z axis in the main ICP chamber of argon discharge with/without 90 V boundary electrode bias at the pressure of 10 mTorr for main ICP only (500 W), auxiliary ICP only (100 W) and both ICPs on. (a): 0 V bias. (b): 90 V bias. 62

Figure 4.3 The ion density (n_i) profile along z axis in the main ICP chamber of argon discharge with/without 90 V boundary electrode bias at the pressure of 10 mTorr for main ICP only (500 W), auxiliary ICP only (100 W) and both ICPs on. (a): 0 V bias. (b): 90 V bias. 63

Figure 4.4 The T_e profile along z axis in the main ICP chamber with different boundary electrode bias and pressure for main ICP only and both plasma on. (a): 0V bias, 10 mTorr. (b): 0V bias, 20mTorr. (c): 0V bias, 40 mTorr. (d): 90V bias, 10 mTorr. (e): 90V bias, 20mTorr. (f): 90V bias, 40 mTorr. The main ICP was operated at 500 W and the tandem ICP was operated at 100W............ 65

Figure 4.5 EEPFs for main ICP only (500 W) and both plasmas on (Upper ICP power 100 W) with different boundary electrode at the position of 250 mm in the main ICP. (a): 0 V bias. (b): 20 V bias. (c): 40 V bias. (d): 55 V bias. The pressure is 10 mTorr with argon flow rate of 80 sccm. 66

Figure 4.6 Ion saturation current as a function of boundary electrode bias for auxiliary ICP only and both ICPs on at the position of z=300 mm and I-V curve for

both plasma on. (a): Upper ICP only. (b): Both ICPs on. (c): I-V curve for both plasmas on with different boundary electrode bias. 68

Figure 5.1 Time-resolved experimentally measured (a) electron temperature (T_e) and (b) electron density for the pulsed main ICP with and without the cw auxiliary ICP for argon at ≈15 mTorr. (c) Predictions of the electron temperature from the model.. 70

Figure 5.2 Time-resolved electron energy probability functions (EEPFs) when only the pulsed main ICP is on, obtained from the (a) experiment and (b) simulation. The times of the EEPFs relative to the start of the 20 μs power pulse are shown in the lower schematic... 72

Figure 5.3 Time-resolved electron energy probability functions (EEPFs) when the pulsed main ICP and the auxiliary ICP are both on, obtained from the (a) experiments and (b) simulations. The times of the EEPFs relative to the start of the 20 μs power pulse are shown in the lower schematic........................ 73

Figure 5.4 Plasma potentials along the axis passing through the central opening of the grid predicted by the model at the end of the active-glow and the end of the afterglow. Values are shown with and without the cw auxiliary ICP.......... 75

Figure 6.1 Estimated wall flux of electrons and electron loss rate by dissociative attachment as a function of time during a pulse. Base case conditions (Table 3.1), except duty cycle = 20%... 80

Figure 6.2 Optical emission intensity of the 837.5 nm line (Cl atoms) as a function of time during a pulse for different duty cycles. Other conditions were at their base case values (Table 3.1)... 82

Figure 6.3 Plasma ignition delay vs. duty cycle, for three different pressures and two different grids. Other conditions were at their base case values (Table 3.1). 83

Figure 6.4 Optical emission intensity of the 750.4 nm line (Ar atoms) as a function of time during a pulse, for different duty cycles at otherwise base case conditions (Table 3.1). 84

Figure 6.5 Plasma parameters as a function of time during a pulse cycle with a duty cycle of 20%. Dashed lines correspond to the positive ion density ($n_{+,aux}$), electron density ($n_{e,aux}$) and electron temperature ($T_{e,aux}$) when only the auxiliary ICP is on. 86

Figure 6.6 Plasma parameters as a function of time during a pulse cycle with a duty cycle of 80%. Dashed lines correspond to the positive ion density ($n_{+,aux}$), electron density ($n_{e,aux}$) and electron temperature ($T_{e,aux}$) when only the auxiliary ICP is on. 91

Figure 6.7 Plasma parameters as a function of time during a pulse cycle with a duty cycle of 99%. Dashed lines correspond to the positive ion density ($n_{+,aux}$), electron density ($n_{e,aux}$) and electron temperature ($T_{e,aux}$) when only the auxiliary ICP is on. 91

Figure 6.8 Plasma parameters as a function of time during a pulse cycle with a duty cycle of 20% and auxiliary ICP power of 200 W. Dashed lines correspond to the positive ion density ($n_{+,aux}$), electron density ($n_{e,aux}$) and electron temperature ($T_{e,aux}$) when only the auxiliary ICP is on. 92

Figure 6.9 Black squares,: Ignition delay vs. time-average power of main ICP. Red circles,: Ignition delay vs. cw power of auxiliary ICP. Other conditions were at the base case values (Table 3.1). Solid and open symbols correspond to grid A and grid B, respectively. 93

Figure 6.10 Plasma ignition delay vs. duty cycle, with different auxiliary ICP cw powers. Open symbols: grid B. Solid symbol: Grid A. Pressure, flow rates, and main ICP peak power were at base case values (Table 3.1). 95

Figure 6.11 Plasma ignition delay vs. duty cycle in different electronegative gases. The main ICP was pulsed with a pulse repetition frequency of 1 kHz. Grid C was used and the pressure was 5 mTorr. 96

Figure 6.12 Black symbols, left axis: ignition delay vs. time-average power of main ICP in SF_6 plasmas. Red symbols, right axis: ignition delay vs. cw power of auxiliary ICP. For all data points, grid C was used, and the pressure was 5 mTorr. 97

Figure 6.13 Black symbols, left axis: Ignition delay vs. time-average power of main ICP in 80%CF_4-20%O_2 plasmas. Red symbols, right axis: Ignition delay vs. cw power of auxiliary ICP. For all data points, grid C was used, and the pressure was 5 mTorr. 99

Figure 6.14 Black symbols, left axis: Ignition delay vs. time-average power of main ICP in O_2 plasmas. Red symbols, right axis: Ignition delay vs. cw power of auxiliary ICP. For all data points, grid C was used, and the pressure was 5 mTorr. 99

Figure 7.1 Schematic of the new experimental apparatus. 104

Figure A.1 Measured and fitted: (a) I-V characteristic, (b) its second derivative. 135

List of Tables

Table 3.1 Base case parameters and range investigated 55

Table 6.1 Ionic mobilities (N is the neutral gas density) [112]................................. 89

Table 6.2 The scattering cross sections for collisions of various chlorine species (10^{-20} m^2) [184].. 89

CHAPTER 1

INTRODUCTION

1.1 Etching technologies in semiconductor industry

Etching is a crucial process in semiconductor device manufacturing. It is used to remove unwanted material from the substrate surface [1-3]. There are three kinds of etching applications in microfabrication: patterned etching, unpatterned etching, and wafer cleaning. Patterned etching is used to remove material from selected areas on the wafer that are not protected by photoresist or a more durable mask (hard mask such as silicon nitride, silicon oxide, metals, etc.). Unpatterned etching can completely (such as photoresist, some oxides, and some nitrides) or partially (for example, spacer etching) remove a layer whose purpose is done. Etching can also be used for wafer cleaning. It can remove contaminants and residues from previous processing. Two kinds of etching technologies are employed in the semiconductor industry: wet etching and plasma (dry) etching. In this section, a brief discussion of plasma etching will be presented.

1.1.1 Plasma etching

Due to its unique properties, plasma is often thought of as the fourth state of matter, and in fact is more than 100 times more abundant in the universe than all the solid, liquid and gas combined [4]. It is defined as a collection of charged particles, neutrals, photons and electromagnetic fields that exhibit collective behavior. Plasma, which was

then called "radiant matter," was first discovered near the electrode in a Crookes tube by Sir William Crookes in 1879 [5]. British physicist Sir Joseph John Thomson systematically studied the nature of such "radiant matter" in 1897 and identified it as charged particles [6]. Irving Langmuir coined the term "plasma" to describe such partially ionized gas in 1928 [7, 8].

Plasma etching, which is also called dry etching, has been used for pattern transfer in the microelectronics industry for nearly 50 years. During plasma etching, a substrate with a patterned mask is immersed in a plasma of an appropriate gas mixture. Radicals and ions from the plasma remove material from the parts of the wafer that are exposed to plasma, leaving materials in the regions that are covered by the mask. The volatile etching products are pumped out of the reactor chamber. Plasma etching has replaced wet etching for most if not all the pattern transfer steps in the semiconductor manufacturing industry. The most important reason for using plasma etching for pattern transfer is that plasma etching can be directional or anisotropic, which is critical for achieving high-resolution pattern transfer [1, 9]. Another reason is that plasma etching can remove some materials which could not be easily removed by wet etching. For instance, etching of silicon nitride (Si_3N_4) cannot be easily accomplished by wet etching, but can be easily achieved in CF_4/O_2 plasma at a high etching rate without photoresist mask lift-off issues [10]. Adoption of plasma etching was also driven by the demand for reducing chemical waste produced by wet etching [11, 12].

1.2 Critical roles of electron and ion energy distribution in plasma etching

Over last 40 years, driven by Moore's law, the feature size of the semiconductor devices has shrunk by nearly two orders of magnitude, from 1.0 µm in the 1980s to 14 nm in 2016. According to the International Technology Roadmap for Semiconductors (ITRS), the next technology node will be 10 nm, followed by 7 nm and 5 nm (Figure 1.1) [13]. In the meantime, advanced chip architectures, such as FinFETs, 3D NAND and through-silicon vias (TSV), are being introduced to overcome scaling issues. The shrinking feature sizes and emerging advanced architectures pose new challenges for plasma etching [14]. These challenges include reducing plasma-induced damage (PID), achieving high uniformity with high throughput, etc. To address these challenges, precise control of the electron energy distribution function (EEDF), and the ion energy distribution (IED) on the substrate is of utmost importance.

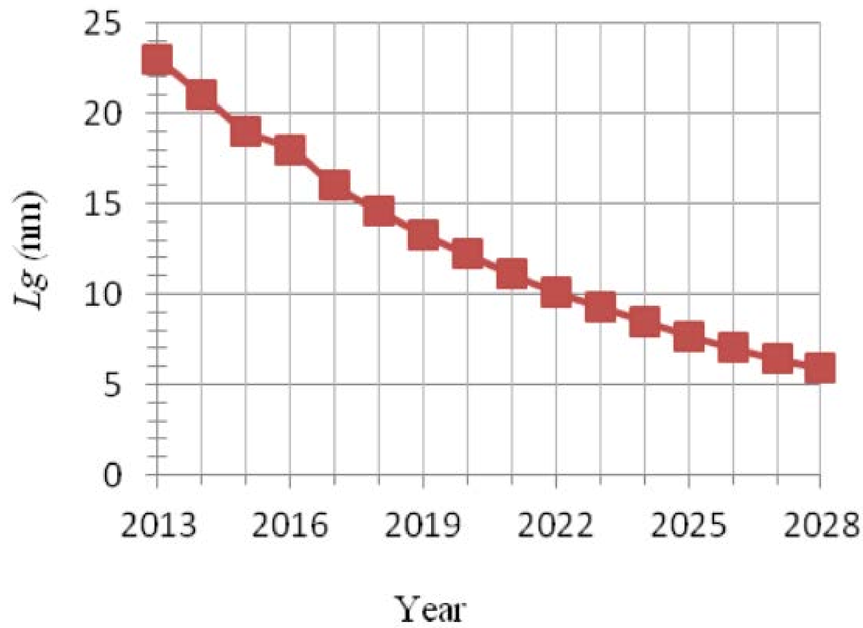

Figure 1.1 Scaling trend of the gate length of high-performance logic transistors [13].

The electron energy distribution function (EEDF) is central to any low-temperature plasma. It governs most of the reactions in plasma processing and determines the gas composition in the plasma, which in turn determines the fluxes of radicals, ions, and photons striking the substrate [15, 16]. As the feature size of semiconductor devices keeps shrinking, controlling the electron energy distribution function (EEDF) becomes increasingly critical to achieve desired etching outcomes such as selectivity and anisotropy, with less damage and more precise critical dimension control [16]. For example, Sugai et al. reported that by tailoring the shape of the EEDF, certain F/CF_x (x=1, 2 or 3) radical concentration ratios can be achieved, leading to high selectivity of etching Si over SiO_2 and Si_3N_4, or vice versa [17].

It is well known that energetic ion bombardment plays a critical role in ion assisted etching [1]. To achieve superior etching characteristics, the ion energy distribution (IED) must be precisely controlled to allow selective and anisotropic etching without damaging the mask or the underlying substrate. For example, Wendt et al. experimentally demonstrated that by applying tailored bias waveforms on the substrate during etching of SiO_2 and Si using fluorocarbon plasmas, narrow IEDs can be achieved on the substrate [18-20]. The peak of the IED can be precisely controlled to be above the threshold of ion assisted etching of SiO_2, but below the threshold of ion assisted etching of Si, leading to very high selectivity of SiO_2 over Si. Their experimental results were captured by Kushner et al. using a "Hybrid Plasma Equipment Model" (HPEM) [21]. In particular, for the purpose of achieving atomic layer etching which is believed to be an enabling technique for advanced etch applications, nearly monoenergetic IED is desired to obtain extreme etching selectivity of top modified layer over the underlying layer [22].

In summary, as the technology node advances to sub-10 nm, controlling the EEDF and IED is becoming increasingly more critical for plasma etching. Many studies have been published on controlling the EEDF and IED to achieve superior etching characteristics. Details are discussed in the literature review in Chapter 2.

1.3 Pulsed plasmas

Pulsed plasma was first investigated in the late 1980s. It offers additional ‘‘knobs’’ to control plasma parameters as well as plasma chemistries, thereby achieving fine etching characteristics (selectivity, uniformity, anisotropy etc.) [23-37]. It is believed to be a promising candidate to address the challenges of plasma etching such as plasma induced damage (PID) and uniformity [38-40]. In pulsed plasmas, the power delivered to the plasma is modulated in time. Figure 1.2 shows a typical case, [38] with τ_{ON} and τ_{OFF} as the durations of the power ON and OFF fraction of the cycle, respectively. The total duration of one pulse cycle is $\tau_P = \tau_{ON} + \tau_{OFF}$. Pulsed plasma offers two new parameters which are critical for the optimization of plasma processing: pulse frequency, $f_P = 1/\tau_P$, and duty cycle, $D = \tau_{ON}/\tau_P$, i.e., the fraction of active glow of one pulse cycle.

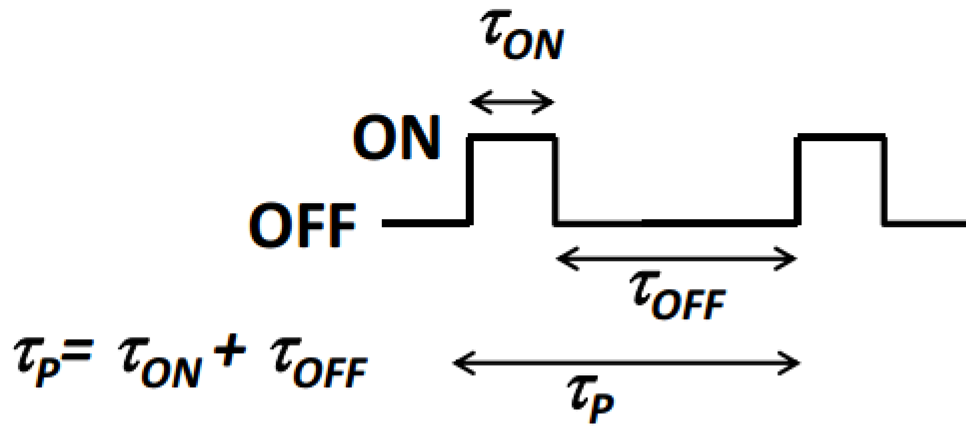

Figure 1.2 Schematic of pulsed plasma [38].

There are four common configurations of pulsed plasmas being employed for plasma etching, as shown in Figure 1.3: (a) source pulsing only with no bias (Figure 1.3(a)), (b) source pulsing with cw bias (Figure 1.3(b)), (c) pulsed bias with continuous wave (cw) source power (Figure 1.3(c)), (d) synchronized pulsed bias with pulsed source power (Figure 1.3(d)). The plasma source is usually powered with frequency from RF to microwave. The bias can be applied to the substrate or an external electrode that makes contact with plasma, and is usually RF or DC. In the configuration of synchronized pulsed bias with source pulsing, both plasma power and bias power are pulsed. But the duty cycle and pulse frequency can be different and usually there is a phase shift between bias power and source power.

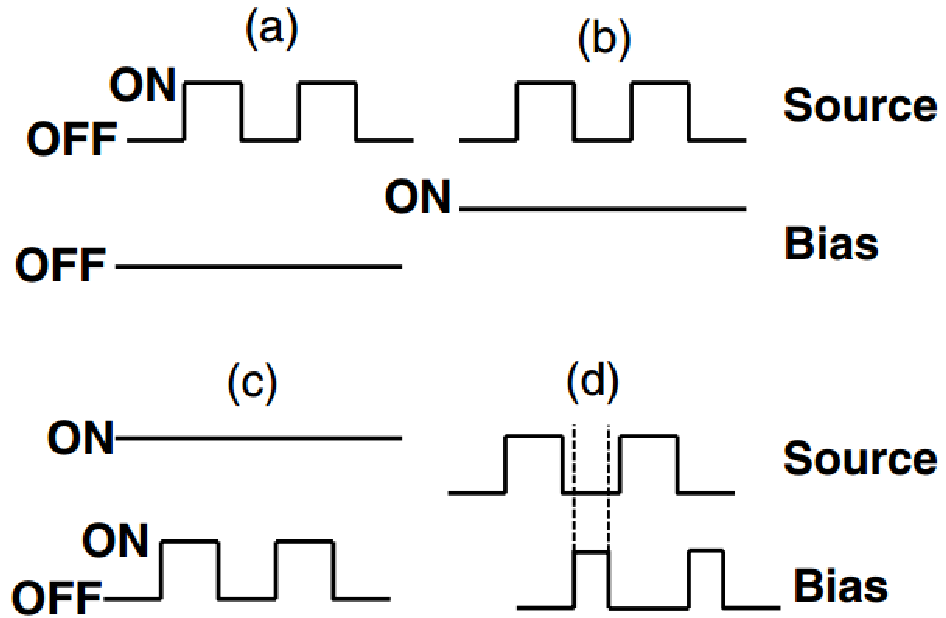

Figure 1.3 Schematics of four kinds of pulsed plasma [38].

By tuning the operating parameters such as pulse frequency and duty cycle, plasma proprieties such as T_e, n_e, IED and EEDF can be manipulated, which gives more flexibility in plasma processing [16, 41]. Recently, nearly monoenergetic IEDs by applying synchronized DC bias on a boundary electrode in the afterglow of a pulsed plasma have been obtained [1, 42-45]. Details of the dynamics and applications of pulsed plasmas will be discussed in Chapter 2.

1.4 **Objective of this research**

The major objective of this research was to control the electron energy distribution function (EEDF) in practical electronegative gas plasmas. For this purpose, we developed a novel dual plasma source consisting of a Faraday-shielded main ICP in

tandem with a Faraday-shielded auxiliary ICP. Operating one of the ICPs in pulsed plasma mode offered better flexibility in controlling the EEDF.

Interestingly, when pulsing the power to the main ICP while operating the auxiliary (ICP) in continuous wave mode, an unexpected delay in plasma ignition was observed under certain operating conditions. Langmuir probe measurements were conducted to understand the physics behind such ignition delay, and a mechanism was proposed.

CHAPTER 2

LITERATURE REVIEW

2.1 Control of electron energy distribution function (EEDF)

Numerous methods have been suggested to control or manipulate the EEDF or electron temperature (T_e) [46]. Some of these methods include varying the plasma operating parameters (e.g., frequency, power) [47, 48], pulsed plasma excitation [49-51], and the use of an external applied axial magnetic field to control T_e in an inductively coupled plasma (ICP) [51]. Magnetic field effects were discussed in a review paper by Godyak [52].

Samukawa et al. [53-56] studied the effect of driving frequency on the EEDF by comparing EEDFs in ICP (13.56 MHz) and UHF (500 MHz) chlorine plasmas with different pressures (3.5 mTorr and 10 mTorr) and a power of 1000 W. They measured T_e by using both Langmuir probe and trace rare gas optical emission spectroscopy (TRG-OES). The T_e obtained from Langmuir probe I-V curve is derived from the slope of the linear part of $\log(I - I_{sat})$–V curve by assuming a Maxwellian EEDF. This T_e is not contributed by high energy electrons ($T_e \gg V_{plasma} - V_{probe}$), because there are very few of them in the EEDF. On the other hand, TRG-OES is more sensitive to electrons with energies above 10 eV. T_e obtained by TRG-OES is contributed by both low energy and high energy electrons (above 10 eV). It should be noted that a Maxwellian EEDF is also assumed in the TRG-OES method. By combining the T_e obtained by both TRG-OES and

Langmuir probe, they derived a qualitative picture of the EEPFs for the ICP (13.56 MHz) and UHF (500 MHz) plasmas, as shown in Figure 2.1.

As seen in Figure 2.1, for UHF (500 MHz) plasma, a Maxwellian T_e of 2.4 eV at 3.5 mTorr and 2.0 eV at 10 mTorr were obtained by the Langmuir probe. T_e obtained by TRG-OES is higher than that obtained by Langmuir probe (3.3 eV at 3.5 mTorr and 2.5 eV at 10 mTorr), indicating that a small portion of high energy electrons (above 10 eV) is distributed above the Maxwellian distributions. The ICP (13.56 MHz) source, on the other hand, has a Maxwellian T_e of 5.3 eV(3.5 mTorr) and 3.7 eV (10 mTorr) for the low energy electrons (measured with the Langmuir probe). The Maxwellian T_e obtained by TRG-OES is lower than that obtained by Langmuir probe.(2.8 eV for 3.5 mTorr and 1.7 eV for 3.5 mTorr), indicating a depletion of high energy electrons(above 10 eV). Samukawa et al. concluded that EEPFs in both ICP and UHF plasmas are bi-Maxwellian. There is an enhanced high energy tail in the EEDF of UHF plasma, while a suppressed high energy electrons tail in the EEDF of ICP.

The reason for the differences between the EEDFs of the ICP and the UHF plasma is because the collision frequency of electrons with energy near 1 eV is about 6.3 MHz in 10 mTorr Cl_2. In UHF plasma, the driving frequency (500 MHz) is much larger than 6.3 MHz, slow electrons oscillate for many UHF periods without colliding with neutrals and gain energy from UHF fields. The high energy electrons, on the other hand, can get the energy from UHF electric field more efficiently because they have a much larger collision frequency (~135 MHz for 15 eV electrons in 10 mTorr Cl_2), resulting in an enhanced high energy tail in EEDF. In ICP source, high energy electrons cannot be heated by electric field efficiently because the collision frequency of high energy

electrons is much greater than RF driving frequency. High electrons will be lost due to inelastic collision and diffusion to the wall, leading to a suppressed high energy tail in EEDF.

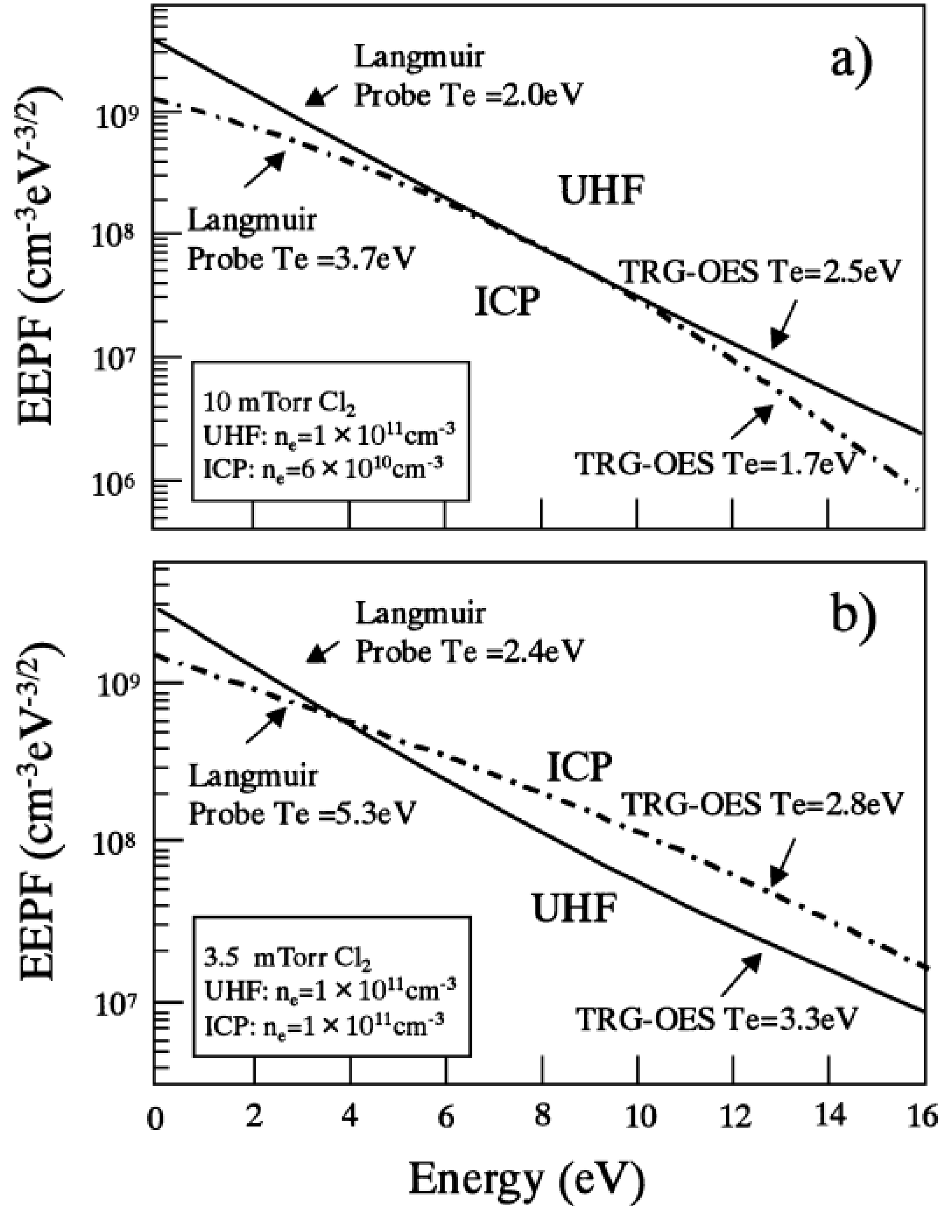

Figure 2.1 A qualitative picture of the EEPFs estimated from a combination of Langmuir probe and trace rare gas optical emission spectroscopy (TRG-OES) measurements of electron temperature at (a) 10 mTorr and (b) 3.5 mTorr for the ICP and UHF plasma [56].

The effect of the pressure on the EEDF was studied by Godyak et al. in argon plasmas sustained in a CCP source at 13.56 MHz [57]. They measured the EEDF at the center of the CCP with the pressure ranging from 100 mTorr to 1 Torr. The results are shown in Figure 2.2. It is observed that at high pressures, the EEDF is Druyvesteyn-like. This is because, at higher pressures, the plasma is sustained by collisional heating. As pressure decreases, electrons are heated in the sheath region (sheath oscillation heating) instead of the bulk plasma, and the shape of the EEDF shifts from Druyvesteyn to bi-Maxwellian. The reason for the formation of bi-Maxwellian EEDF is well understood. As the plasma shifts to sheath heating mode, electrons are heated in the region closed to the electrodes where strong RF and DC electric fields exist. Only high energy electrons can overcome the DC ambipolar potential barrier in the bulk plasma to arrive at the heating zone where they are heated by the strong RF electric field. The high energy electrons generated in the heating zone will then diffuse back to the bulk plasma causing excitation and ionization of the gas. Low energy electrons produced by such ionization are trapped in the bulk plasma by the ambipolar electric field and cannot be heated by the weak electric field in the bulk plasma, resulting in a bi-Maxwellian EEDF.

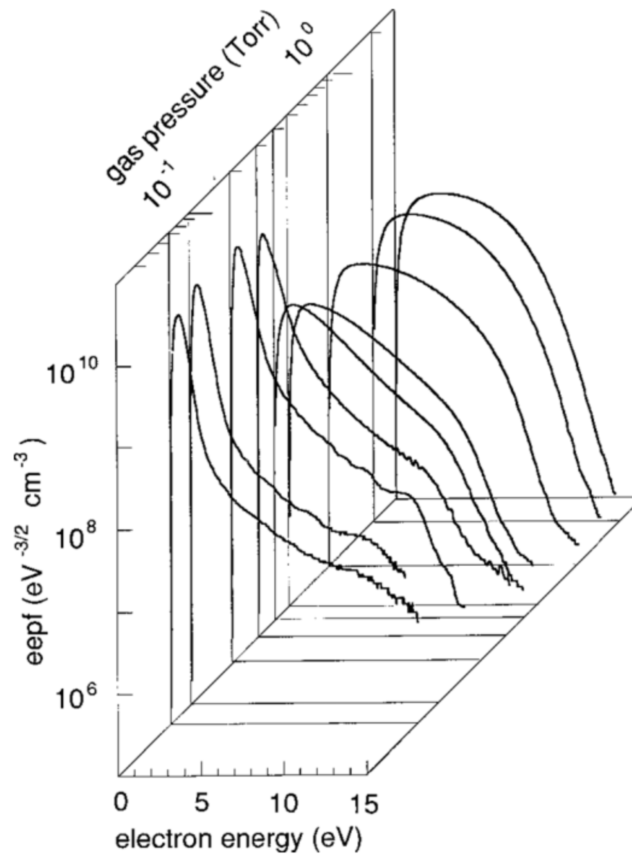

Figure 2.2 EEPF evolution with argon pressure in a CCP at 13.56 MHz [57].

It was suggested that the EEDF can also be controlled by using pulsed plasma. Song and Kushner conducted simulations of a dual-frequency CCP source with Ar or $Ar/CF_4/O_2$ (75/20/5) mixtures [58]. In their studies, the upper electrode was powered by a 40 MHz RF source operated in pulse mode with an averaged power of 500 W, pulse frequency of 50 kHz and duty cycle of 50%. The lower electrode was powered in cw mode with 500 W at 10 MHz. The pressure was kept at 40 mTorr with a total flow rate of 200 sccm. The gap between the parallel plate electrodes was 4 cm.

Figure 2.3 shows the calculated EEDF at different time during one pulse cycle and at three locations in the interelectrode gap: (a) near the higher frequency sheath, (b)

in the bulk plasma and (c) near the lower frequency sheath. The comparison of averaged EEDFs over one pulse cycle with the EEDFs when both electrodes were powered in cw mode is also shown in Figure 2.3. It is seen that the high energy tail of the EEDF can be modulated during one pulse cycle. The tail of the EEDF extends to much greater energies at the beginning of active glow. This is because, at the beginning of the active glow, the electron density is low since most of the electrons were lost during the afterglow of the previous pulse cycle. Thus, the power delivered to the plasma is distributed into a small number of electrons, creating a spike in the (effective) electron temperature when the power is turned ON to begin a new cycle. High electron temperature implies a high energy tail of the EEDF. During the afterglow, a depletion of the high energy tail of the EEDF was observed because high energy electrons are lost due to inelastic collision and diffusion to the wall. They also found that by tuning the duty cycle, the time-averaged EEDF can be manipulated. In addition, the EEDFs near the electrodes had more high energy electrons than the EEDFs in the middle of the gap, because electrons wee heated in the sheath region near the electrodes.

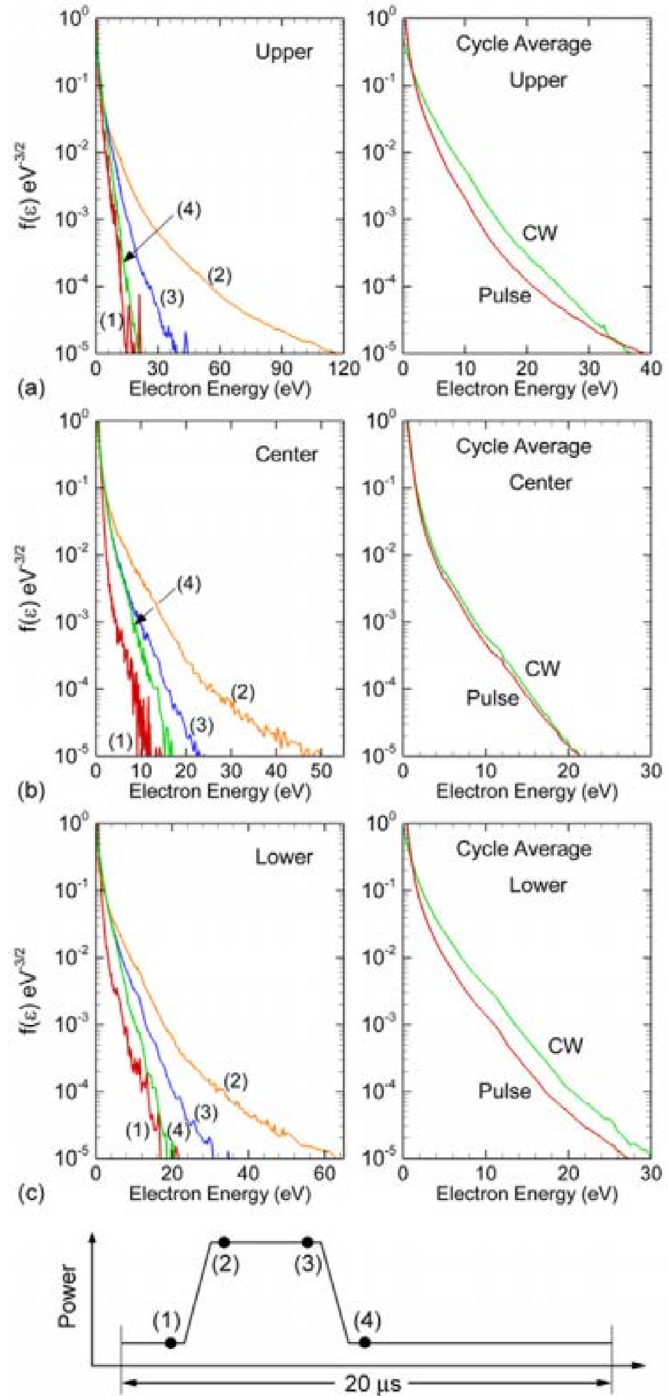

Figure 2.3 EEDFs at different times during the pulse cycle, shown in the bottom figure: (a) Near the higher frequency sheath, (b) in the bulk plasma and (c) near the lower frequency sheath. Averaged EEDF over one pulse period and under CW excitation are shown in the right column [58].

Diomede et al. reported that the EEDF can be manipulated by applying a DC bias on the powered electrode in a pulsed CCP source [59]. They simulated the time evolution of the EEDF during one pulse cycle. The plasma was pulsed at 10 kHz (100 μs pulse period) with a duty cycle of 50%. A DC bias of 50 V was applied to the powered electrode in the afterglow at t=70 μs for 15 μs, followed by a DC bias of 300 V till the end of the afterglow. The calculated EEDFs are shown in Figure 2.4. Once the 300 V DC bias was applied, electrons were heated and the EEDF was shifted from a bi-Maxwellian with a cold tail to a bi-Maxwellian with a hot tail. This is because by applying dc bias on the electrode, the sheath is expanded and more electrons are heated by the expanded sheath, resulting in an increase in the high energy tail of the EEDF.

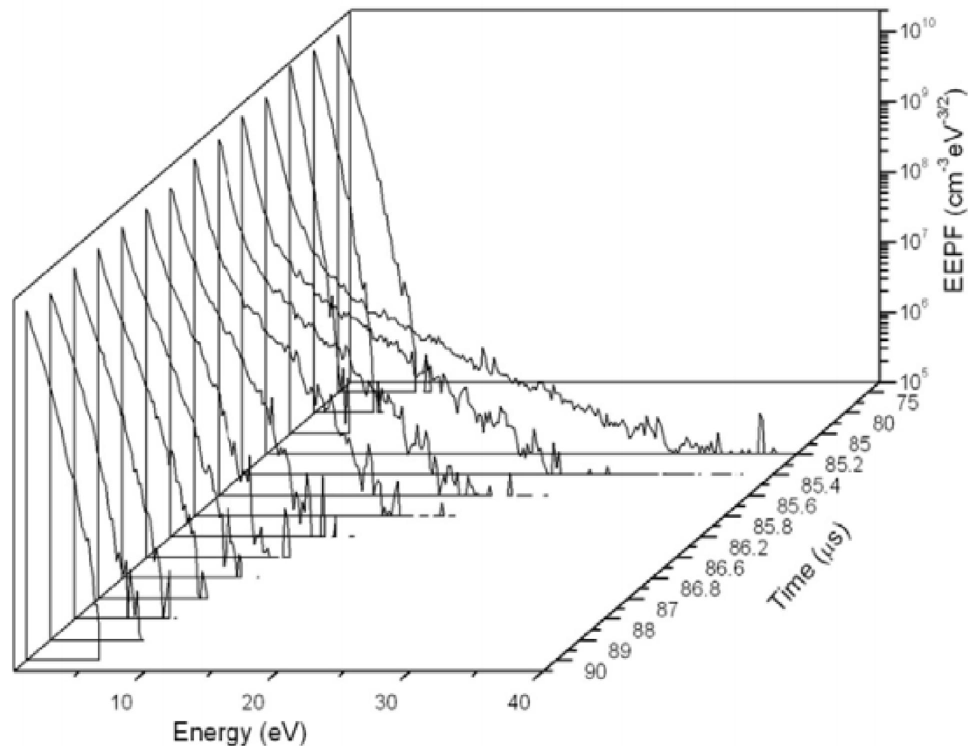

Figure 2.4 Time evolution of the calculated EEPF at the discharge center. Time t = 0 refers to the start of the active glow (plasma ON). A Maxwellian distribution would be a straight line on this plot [59].

Donnelly et al. studied the evolution of EEDF in pulsed Cl_2 plasma sustained in an ICP source with and without cw RF bias applied to the substrate [60]. The plasma was pulsed at 10 kHz with a duty cycle of 50% and average power of 300 W. The cw bias applied on the substrate was 70 W at a driving frequency of 12.5 MHz. The EEDF at different times during the afterglow measured by Langmuir probe are shown in Figure 2.5. It was found that, without bias, the EEDF exhibited the expected behavior as discussed above. In the presence of RF bias, at 70 μs (17 μs into the afterglow), EEDF starts to deviate from those with no bias and an enhanced high energy tail starts to emerge. That is because plasma transitioned to so-called "reactive ion etching mode," and are sustained solely by the capacitive bias power. Electrons are heated by oscillating sheath near the substrate, resulting in an enhanced high energy tail in EEDF. In the late glow, EEPF with bias become a typical bi-Maxwellian with an enhancement of the high-energy tail, which is typical in CCPs.

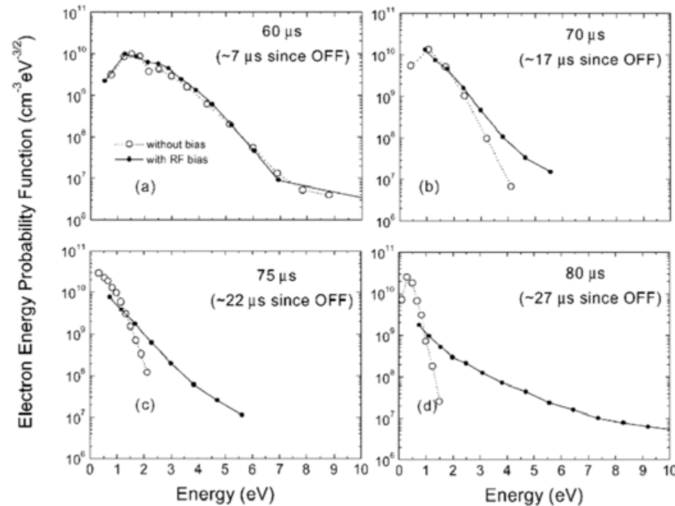

Figure 2.5 EEPFs for different times during the afterglow of a 10 mTorr Cl2 plasma. Open symbols denote the case with no bias; closed symbols denote the case with RF bias (70 W) on the substrate electrode. A Maxwellian distribution would be a straight line on this plot [60].

All of the methods discussed above may be considered "internal control" since the plasma is being directly acted upon. External control of the EEDF includes methods of control not directly applied to the plasma of interest. External control involves transport of species into the plasma. One such external control method for manipulating EEDFs is the use of a biased grid separating a plasma region from the ensuing downstream region [16, 61], a configuration investigated by Hong et al., as shown in Figure 2.6 [62]. Figure 2.7 shows EEDFs as a function of bias applied to the grid [62]. It is found that EEDFs are Maxwellian when the grid bias ranges between 20 V to -6 V. As the grid bias decreases from 20 V to -6 V, T_e decreases from 1.9 eV to 1.3 eV. This is because reduction in the grid bias leads to a reduction of low-energy electrons. As the grid bias decreases below -8 V, the EEDF transforms from Maxwellian to bi-Maxwellian, as the fast electrons are cooled down by inelastic collisions [63, 64]. The bulk electron density also decreases with decreasing grid bias, due to the reduction of low-energy electrons due to the negative grid bias.

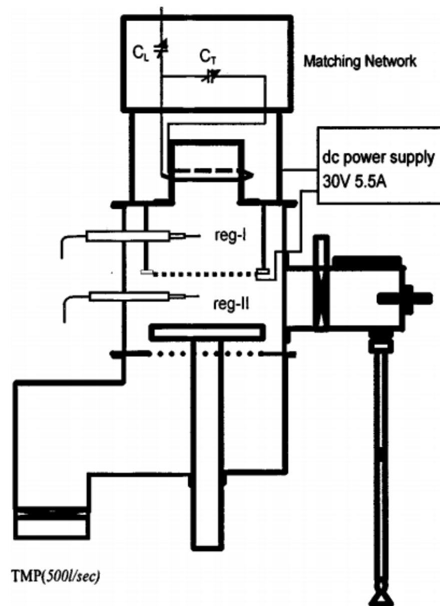

Figure 2.6 Experimental setup with the chamber divided by a grid [62].

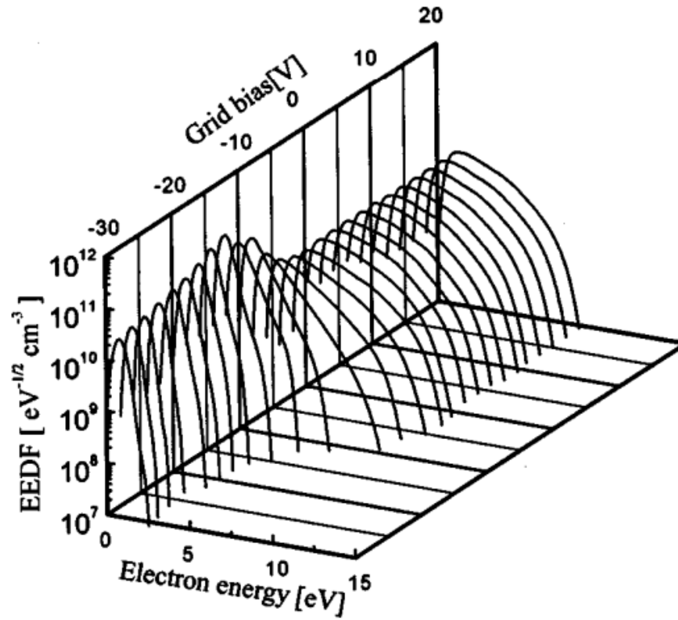

Figure 2.7 Measured EEDFs as a function of grid bias [62].

Dudin and Rafalskyi [65] employed a biased grid separating an ICP sustained in SF_6 from a cold diffuse plasma downstream. They identified the range of grid bias for which they could extract a continuous neutralized positive ion-negative ion beam. Sato et al. [66] injected electrons in a capacitively coupled plasma (CCP) reactor through a grid serving as the grounded electrode, to control the ion energy distribution (IED) incident onto the counter (powered) electrode. Uhm et al. [67] proposed a dual ICP system consisting of a remote ICP co-axial with a main ICP. By adjusting the value of a series variable capacitor at the end of the main ICP coil, they could vary the plasma density and T_e. It should be noted that there was no grid separating the two plasmas.

The EEDF can also be manipulated by "Maxwell demons," as proposed by MacKenzie et al. [68] In their experiments, they inserted a tungsten wire in a plasma and applied a voltage of 100 V to the wire with respect to the grounded chamber wall. Hot

electrons were confined in the plasma while cold electrons were absorbed by the tungsten wire, resulting in an increase of the high energy tail of the EEDF and increased T_e.

2.2 Control of the ion energy distribution (IED)

The ion energy at the surface of the substrate is determined by the sheath voltage and collisions between ions and neutrals within the sheath. To achieve superior etching characteristics, the ion energy must be precisely controlled to allow selective and anisotropic etching without damaging the mask or the underlying substrate. Wendt et al. [18-20] and Kushner et al. [21] achieved narrow IDEs by applying tailored bias waveforms on the substrate during etching of SiO_2 and Si using fluorocarbon plasmas. The application of tailored bias voltage waveforms to control the IED has been reviewed by Economou [69]. Ion energy can be precisely controlled to be above the threshold of ion assisted etching of SiO_2, but below the threshold of ion assisted etching of Si, leading to a very high selectivity of SiO_2 over Si, as shown in Figure 2.8 by Wendt et al. [70] Recently, obtaining nearly monoenergetic ion energy distributions for improved control of ion-bombardment-stimulated surface processes, especially near an energy threshold for such processes has been the subject of many works [16, 42, 71-73].

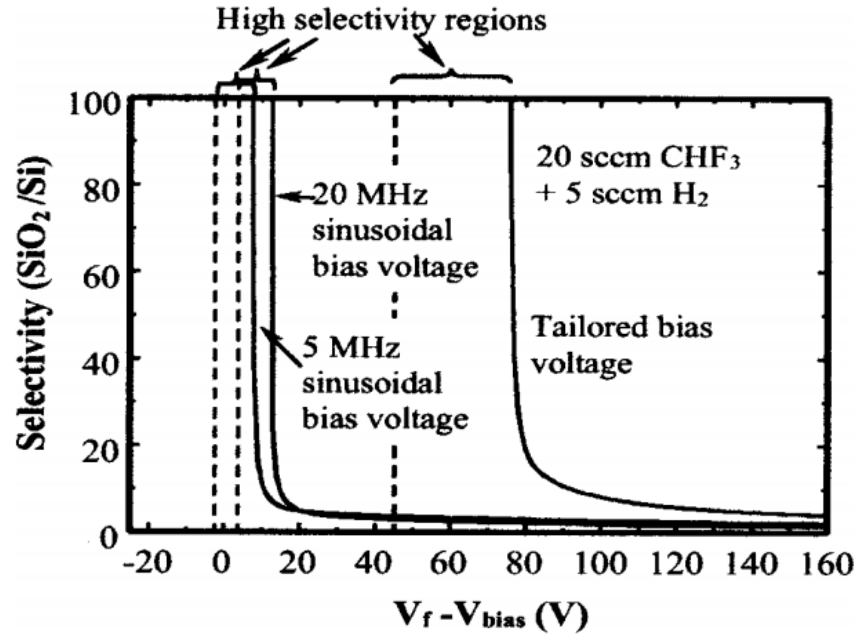

Figure 2.8 Selectivity of SiO_2/Si etching in a CHF_3(20 sccm)/H_2(5 sccm) plasma for three bias voltage wave forms: 5 and 20 MHz sinusoidal, and tailored. The dashed lines indicate the average bias voltage corresponding to the etching threshold for SiO_2 [70].

By applying a negative DC bias, the sheath voltage can be increased, causing ion energy to be increased [74]. For RF bias, the shape of IED is determined by the relationship between ion transit time τ_{ion} and the period of the RF voltage (the inverse of RF frequency ($\tau = 1/f$)) [75-82]. Ion transit time is defined as the time it takes for the ion to traverse the sheath (i.e., from the plasma to the surface). At low RF frequency, τ_{ion} is shorter than τ; the ion energy will be determined by the instantaneous sheath voltage at the time the ion enters the sheath, leading to a wide bimodal IED. On the other hand, at high RF frequency or relatively thick sheath, τ_{ion} is much longer than τ, and ions experience the time-average sheath voltage, yielding a narrow IED. Figure 2.9 shows particle in cell (PIC) simulation results of IED for a single sheath in a current-driven

helium discharge at frequencies from 1 MHz to 100 MHz [79]. It can be seen that as the RF frequency increases, the peak separation of the bimodal IED narrows.

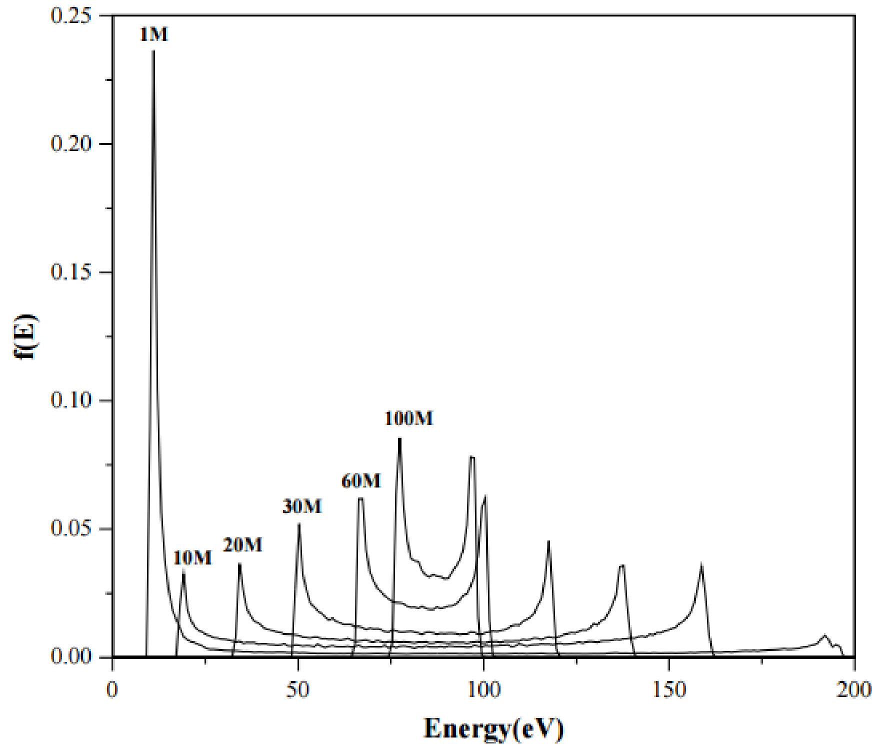

Figure 2.9 Particle in cell (PIC) simulation results showing IEDs of helium ions hitting the target electrode of RF discharges driven at frequencies from 1 MHz to 100 MHz [79].

IED on the substrate can also be modulated by modulating source power with constant bias power. By modulating the source power, plasma density is modulated. During the active glow, the ion density is high, leading to a larger ion current to the substrate compared with that in afterglow. With the same bias power delivered to the substrate, higher ion current leads to a lower voltage across the sheath, resulting in lower ion energy during the active glow compared with that during the afterglow. Agarwal et al. [83] conducted a simulation study of IEDs within a pulse cycle for an Ar/Cl_2 ICP pulsed

plasma with a peak power of 300 W, pulse frequency of 5 kHz, and duty cycle of 50%, as shown in Figure 2.10 (a). The peak bias power is 100 W. They found that the ion energy during the active glow peaks at ~100 eV. During the afterglow the ion energy ranges from 250 – 350 eV. The simulation results agree well with experimental date obtained by Zabeida et al. [84], as shown in Figure 2.10(b). Since the ion energy during the afterglow is much larger than that during the active glow, the etching rate during the afterglow can be larger than that during the active glow. Agarwal et al. reported that with the same bias power, the etching rate in a pulsed plasma with 50% duty cycle is larger than 50% of the etching rate obtained in cw plasma under otherwise the same conditions [83].

Another approach to controlling the IED is by applying a positive bias on a boundary electrode in contact with the plasma [85, 86]. Plasma potential (V_P) can be shifted by the bias which in turn increases the sheath voltage, leading to an increase in ion energy. Economou *et al.* [87] reported that by applying RF bias on a boundary electrode, the plasma potential (V_P) can be lifted by more than 100 V, which in turn accelerate ions out of plasma, leading to a positive ion flux of 100s of eV. The extracted energetic ions are neutralized when passing through a neutralizer grid, yielding a fast neutral beam.

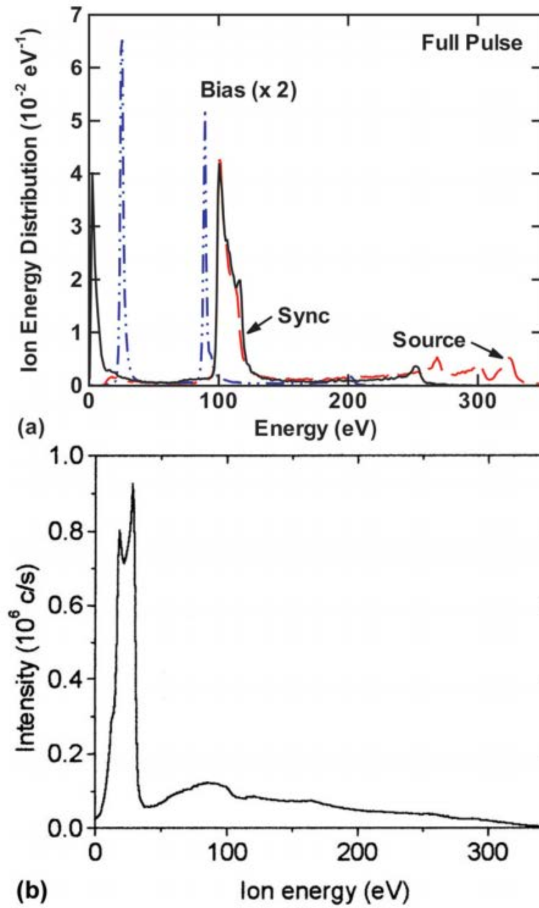

Figure 2.10 (a) Model predicted pulse-averaged ion energy distributions. (b) Experimentally measured average ion energy distribution [83].

In all approaches discussed above, ion energy distribution is controlled in continuous wave plasma. The shape of IED is limited by the spatial variation of the plasma potential, which is proportional to the electron temperature, T_e [21]. In other words, the energy of ion entering the sheath depends on where the ion was born. So even if the sheath potential waveform is designed to yield a narrow IED, the spread of the resulting IED can be several times T_e. To achieve a very narrow IED, extracting ions from plasma with very low T_e is required. One successful approach is to apply synchronized DC bias on a boundary electrode in the afterglow of pulsed plasma to

control the instantaneous plasma potential, as proposed by Xu et al.[23]. They obtained a narrow IED with a full width at half maximum (FWHM) of less than 3 eV in a pulsed capacitively coupled plasma (CCP). The peak energy of the resulting IED was approximately equal to the applied DC bias. Nam et al. did a particle in cell (PIC) simulation with Monte Carlo collisions using the same conditions as Xu's experiments. They captured Xu's experimental results, as shown in Figure 2.11 [88].

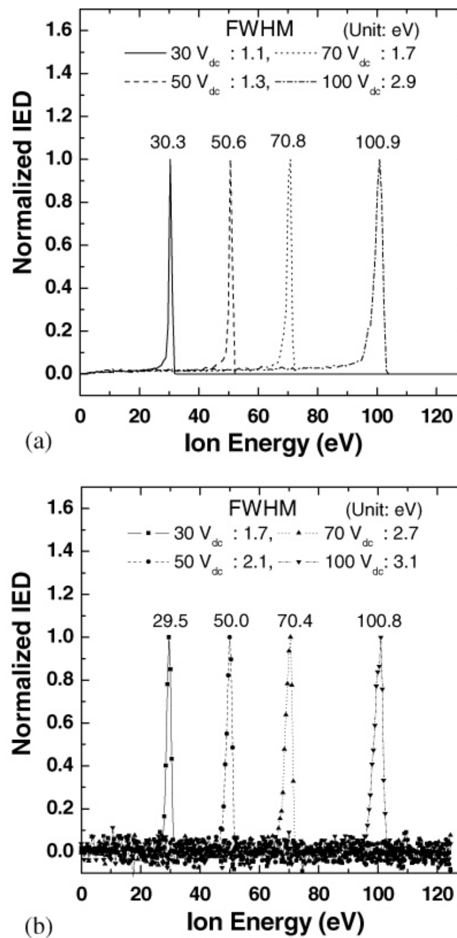

Figure 2.11 (a) Predicted energy distribution of extracted ions for different DC bias potentials applied in the afterglow [42]. (b) Experimental data of for the same conditions as in the simulation (FWHM=full width at half maximum) [23].

Shin et al. used Xu's approach in an inductively coupled plasma (ICP) and obtained narrow IED with a FWHM of less than 2 eV [44, 89]. Diomede et al. reported results using both Particle-in-Cell (PIC) simulation [59] and an equivalent circuit model [90]. Simulation and modeling results matched the experimental data very well. Logue et al. [76] performed a computational investigation of Shin's experiments using the hybrid plasma equipment model (HPEM). They also predicted the experimental measurements of plasma properties and IEDs.

It should be noted that in an ICP source, the IED is broadened by capacitive coupling from the high-voltage end of the coil, imposing an RF potential on the DC plasma potential [77]. The RF voltage can be eliminated with a Faraday shield. Especially with electronegative gases, however, it is challenging to ignite pulsed ICPs, since the electron density decays rapidly when power is turned OFF, and re-ignition requires large electric fields produced by high-voltage capacitive coupling.

2.3 **Dynamics of pulsed plasma**

Many researchers have studied the dynamics of pulsed electropositive plasmas, including simulations and experiments [91-97]. For example, Lieberman et al. published a computational investigation of pulsed argon plasmas using a spatially averaged (global) model [91, 95]. By solving the particle and energy balance equations, they could obtain the time evolution of the electron temperature and plasma density within one pulse cycle, as shown in Figure 2.12. Lymberopoulos et al. [92] investigate the spatial- and time-resolved properties of pulsed argon plasma using a one dimensional fluid model.

Subramonium and Kushner [93, 94] developed two and three dimensional fluid model to understand the dynamics of pulsed argon plasma. Results of all these studies match each other very well.

Figure 2.12 shows the global model results of the time evolution of plasma density, electron temperature, and excited atom (4s and 4p) densities with different pulse frequency. The time-averaged power is 500 W, and the duty cycle is 25%. It is found that with a pulse frequency of 100 kHz (pulsed period of 10 μs), electron temperature increases gradually in the active glow, and plasma density is almost constant within one pulse cycle. Both electron temperature and plasma density are close to those of cw plasma with power of 500 W. This is because the pulse period is too short for plasma density and electron temperature to respond to power modulation. As the pulse period increases (pulse frequency decreases), both electron temperature and plasma density follow the power modulation.

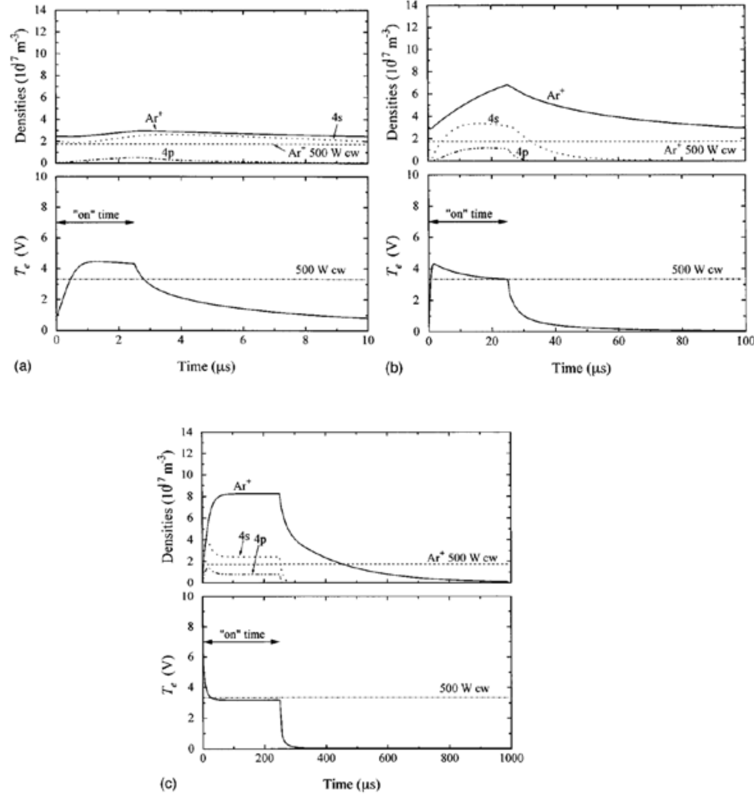

Figure 2.12 Time evolution of plasma density, electron temperature, and excited atom (4s and 4p) densities for different periods t for a time-average power of 500 W and a duty ratio of 25%: (a) t=10 μs; (b) t=100 μs; (c) t=1000 μs [91].

Hebner and Fleddermann [98] experimentally investigated the time evolution of electron density and plasma potential in a pulsed argon plasma, as shown in Figure 2.13. In Figure 2.13(a), time-resolved n_e is shown as a function of duty cycle. The duty cycle was 10, 30, 50, and 70% for a constant peak RF power of 300 W and the pulse frequency of 10 kHz. It is found that with low duty cycle (10%), n_e cannot reach the steady state at the end of active glow. For duty cycle larger than 50%, a plateau of n_e can be observed, and the value of n_e at the plateau is as the same as that of cw plasma with the same power. Figure 2.13(b) shows the effect of peak power on n_e. The peak power is 165, 190, and 290 W for a constant duty cycle of 30% and a pulse frequency of 10 kHz. It can be seen

that $n_{e.}$ cannot reach the plateau at the end of active glow for all of the three powers. That's because with the duty cycle of 30%, the duration of active glow is too short for the plasma to reach the steady state. In figure 2.13(c), the peak power and duty cycle are fixed at 300W and 50%, while the pulse frequency is varied from 5 kHz to 20 kHz. The electron density can reach the steady state with the pulse frequency of 5 kHz and 10 kHz. With the pulse frequency of 20 kHz, electron density cannot reach steady state because the active glow period is too short.

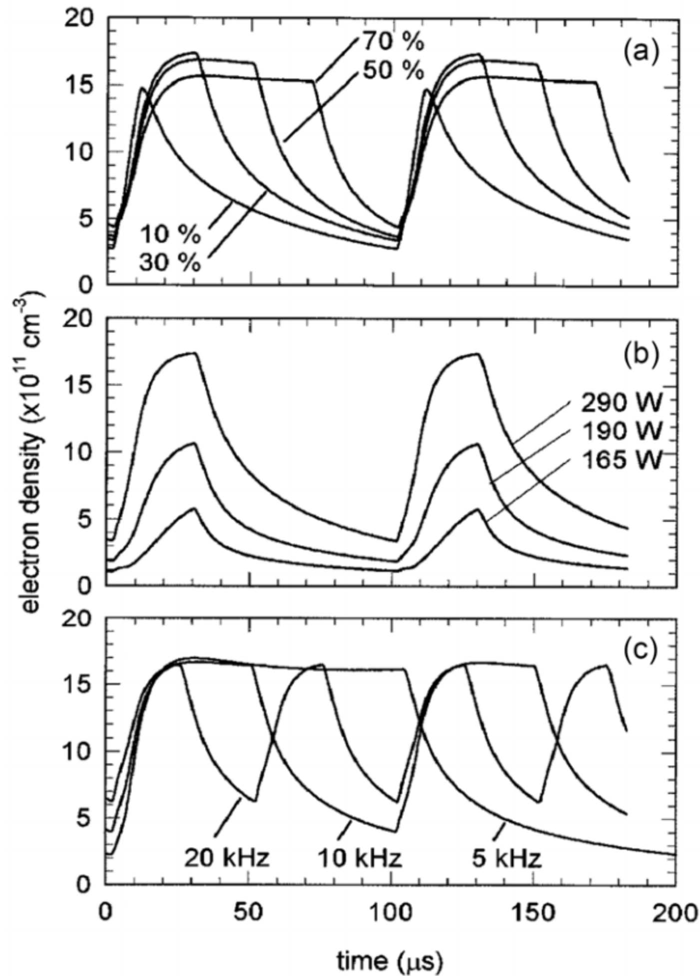

Figure 2.13 Time dependent electron density in an argon plasma as a function of (a) duty cycle, (b) peak RF power, and (c) pulse repetition frequency. In all cases, the pressure was 20 mTorr [98].

Electronegative gases such as Cl_2, SF_6 and CF_4 are widely used in semiconductor industry for plasma etching [73]. The dynamics of pulsed electronegative plasmas are much more complicated than that of electropositive plasmas because of the presence of negative ions [99, 100]. Ion-ion plasma formation during the afterglow of pulsed electronegative plasma has been reported [101-107]. The dynamics of pulsed electronegative plasmas including Cl_2 [94, 99, 106, 108-116], SF_6 [117, 118], O_2 [119-122] and CF_4 [115, 123] have been extensively studied by many researchers.

Midha and Economou reported one dimensional simulation results of pulsed Cl_2 plasma in an ICP source [99]. Figure 2.14 shows the time evolution of the densities of different species and electron temperature at the central plane of the reactor. The plasma source is pulsed with a period of 100 μs and duty cycle of 50%. The peak power is 320 W and the pressure is 20 mTorr. The simulation results match other researchers' experimental results very well [50, 106, 108].

In Figure 2.14, during early active glow period (0–15 μs), once the power is turned ON, T_e increases much more sharply compared with electropositive plasma (Figure 2.12(b)). That's because, in pulsed electronegative plasma, there are very few electrons remaining at the beginning of active glow due to the high loss rate of electrons by attachment and diffusion to the wall in the afterglow of the previous pulse cycle. On the other hand, ion-ion plasma is formed during the afterglow of last pulse period. Electrons can diffuse freely in ion-ion plasma according to the equation of the ambipolar electron diffusivity D_{ae} in an electronegative plasma given by Ref. [99, 100]:

$$D_{ae} \approx \left[\frac{1+2(n_n/n_e)}{[(\mu_n/\mu_e)+1]+2(n_n/n_e)}\right] D_e, \tag{2.1}$$

where n_n and n_e are density of negative ions and electrons, respectively. μ_n and μ_e are mobility of positive ions and electrons, respectively. D_e is free electron diffusivity. For ion-ion plasma, $n_n \gg n_e$ and $D_{ae} \approx D_e$, indicating that electrons diffuse freely, leading to a small electron density at the central plane of the reactor. The high T_e at the beginning of active glow promotes ionization and n_e starts to increase. The positive ion density also starts to increase by ionization. The sheath starts to form and the negative ions are squeezed towards the center of the plasma by the ambipolar field. In the meantime, negative ions are lost by detachment, leading to a minimum value of negative ions in the early active glow. Although the loss rate of negative ions by detachment is larger than the production rate of negative ions by attachment, the negative ion density increases at the center of the plasma in the active glow because they are squeezed towards the center of the plasma. (Figure 2.15, top) This mechanism have been theoretically studied by Kaganovich et al. [124, 125].

During the late active glow (15–50 μs), n_e, T_e and n_p reach a quasi-steady state. Negative ions are confined in the bulk plasma, forming an electronegative core which is surrounded by a region which is dominated by electrons and positive ions, followed by a sheath region in which only positive ions and much fewer electrons are present.

During the early afterglow (50–75 μs), once the power is turned OFF at t = 50 μs, T_e starts to decay sharply by inelastic collision and ambipolar diffusion to the wall. The decay rate of T_e slows down once T_e is below the inelastic collision threshold. As T_e keeps decreasing, the plasma sheath starts to collapse, and negative ions start to diffuse freely to the wall. (Figure 2.15, bottom) n_e also starts to decrease due to attachment and diffusion to the wall with a slower decay rate compare to T_e. However, negative ions are generated

by dissociative attachment at a high reaction rate because dissociative attachment has its peak cross-section at low T_e, making the plasma more and more electronegative [116]. At the end of this period, an ion-ion plasma forms.

During the late afterglow (75–100 μs), an ion-ion plasma is formed. Electrons are no longer trapped in the plasma and are lost to the wall by diffusion. (Figure 2.15, bottom) Positive and negative ions become the dominant charged species in the plasma and decay slowly by ion–ion recombination and diffusion to the wall. Since electron density is extremely low at the end of afterglow, it is very challenging to re-ignite plasma at the beginning of the next pulse cycle.

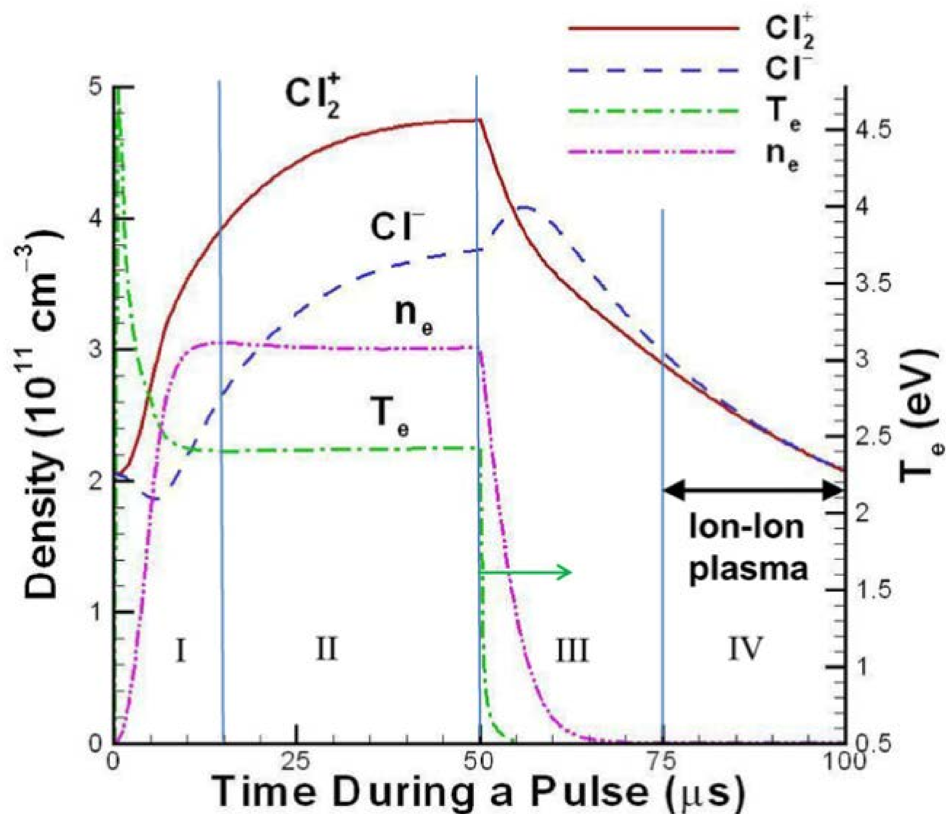

Figure 2.14 Time evolution of species densities and electron temperature predicted by a pulsed plasma model in chlorine. Only the major ion Cl_2^+ density is shown (Cl^+ is not included) [99].

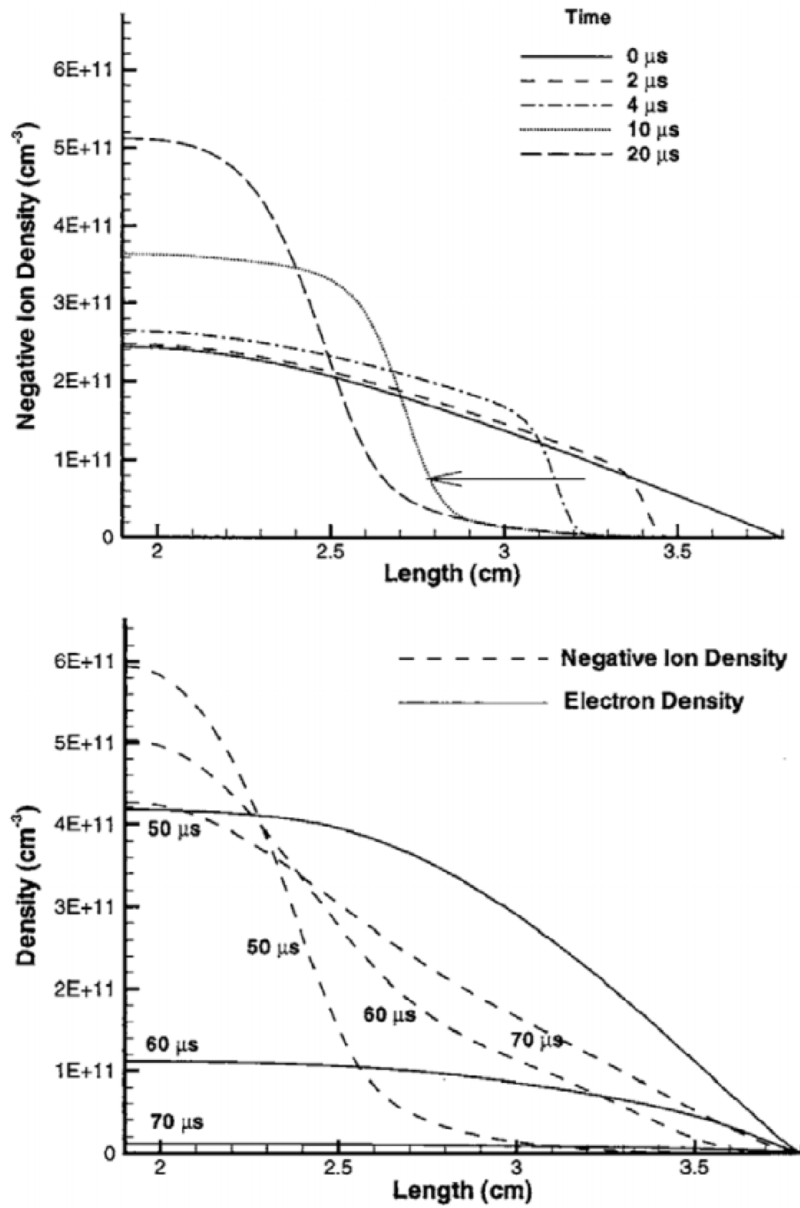

Figure 2.15 Predictions of a model of a pulsed CCP chlorine plasma. (top) Space and time evolution of the negative-ion Cl^- density during the first 20 μs of the active glow. (bottom) Space and time evolution of negative ion and electron densities during the first 20μs of the afterglow [99].

2.4 Applications of pulsed plasma

By tuning the operating parameters such as pulse frequency and duty cycle, the averaged plasma proprieties can be manipulated, which gives more flexibility in plasma processing. The potential benefits of pulsed plasma for plasma etching will be discussed in this section.

2.4.1 Control of plasma chemistries

Samukawa et al. [126-134] studied polycrystalline silicon etching in pulsed halogen-containing plasmas. They demonstrated that better uniformity, anisotropy, selectivity, lesser damage and more precise critical dimension control could be obtained by using pulsed plasma. In particular, pulsed electronegative plasma can also reduce or eliminate undesirable etching anomalies (such as notching) caused by differential charging in features by injecting negative ions into the feature to neutralize the positive charges [127-129, 131, 132, 135-138]. For example, they measured the etching rate of polycrystalline Si and SiO_2 in a pulsed Cl_2 plasma in an electron cyclotron resonance (ECR) plasma as a function of pulse width and pulse interval (duration of afterglow) and compared them with those obtained in a cw plasma [138]. The pressure is 1 mTorr and the peak power is 1 kW. Figure 2.16 shows the etching rate of Si and SiO_2 as a function of the pulse interval with the duty cycle fixed at 50%. The pulse interval of 0 μs corresponds to cw plasma. In this figure, it is found that with pulse interval less than 50 μs, the etching rate of Si is larger than 50% of that in cw plasma. As the pulse interval exceeds 50 μs, the etching rate of Si equals 50% of that in a cw plasma. That's because with pulse interval less than 50 μs, density of ions with energy of more than a few eV

does not decay too much during power OFF period, etching of Si can still happen even with power turned OFF. When the pulse interval is more than 50 μs, ion density will decay to a small value that cannot sustain etching of Si. Since etching of SiO_2 requires high ion energy and cannot happen during power OFF period, etching rate of SiO_2 in pulsed plasma is 50% of that in cw plasma and is independent of pulse interval. The selectivity of Si over SiO_2 can be manipulated by tuning the pulse interval.

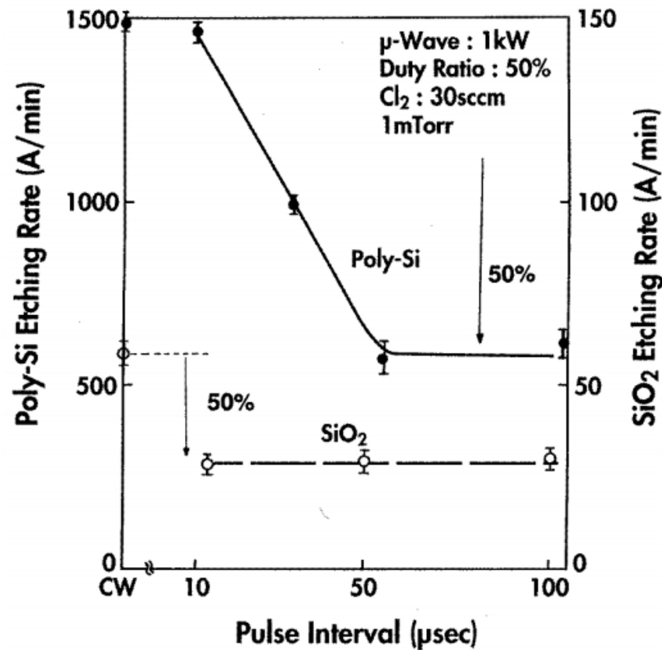

Figure 2.16 Variation of poly-Si and SiO_2 etching rates with pulse interval for a constant 50% duty cycle [138].

Samukawa et al. measured the dependence of the F/CF_2 radical density ratio in CHF_3, C_2F_6 and C_3F_8 gases on the pulse width, as shown in Figure 2.17 [139]. It is found that as the pulse width increases with a fixed pulse interval (10 μs), the duration of dissociation processes increases, leading to an increased F/CF_2 radical density ratio. However, the polymer deposition rate in C_2F_6 and C_3F_8 plasma is much higher than in

CHF_3 plasma, because of the larger amount of CF_2 radicals, leading to a higher etching selectivity of SiO_2 over Si.

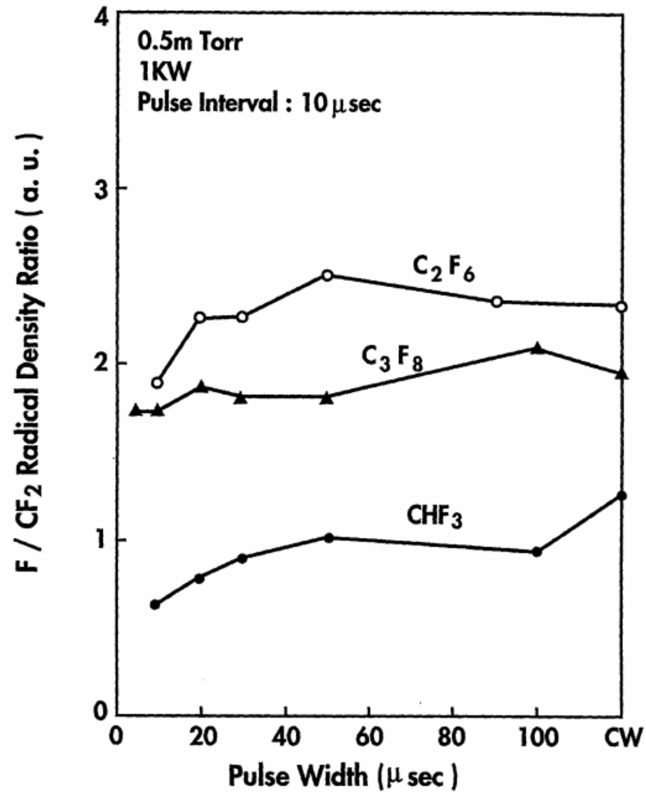

Figure 2.17 F/CF_2 radical density ratio in pulsed CHF_3, C_2F_6 and C_3F_8 plasmas as a function of pulse width for a constant 10 μs pulse interval [139].

Sugai et al. reported that by changing the duty cycle of pulsed CF_4/H_2 plasmas, the density ratio CF_x/F (x=2,3) can be controlled, which enables control of selectivity of etching Si over SiO_2, or SiO_2 over Si with reasonable etching rate [140]. Figure 2.18 shows averaged absolute values of CF_x densities obtained by mass spectrometry and the averaged relative density of F atom by actinometry as a function of active glow duration with afterglow fixed at 15 μs. In this figure, it is found that as the duration of active glow decreases, the density of all radicals decreases with different time constants. In particular,

the F density decreases faster than CF_2 and CF_3, leading to a larger density ratio of CF_x/F (x=2,3) with decreasing duration of the power ON time .

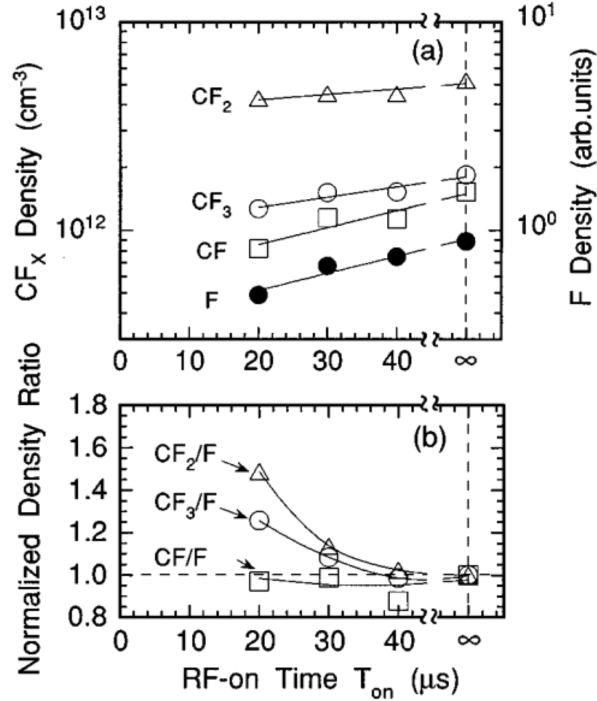

Figure 2.18 (a) The absolute CF_x density and the relative F density, and (b) the normalized density ratio CF_x/F as a function of the RF-on time. T_{off} = ∞ corresponds to the continuous mode. The measurements were done at the position 12.5 cm above substrate [140].

Figure 2.19 (a) shows the etching rate of SiO_2 and Si in 50% CF_4/50% H_2 pulsed plasma as a function of the duration of active glow. The duration of afterglow is fixed at 15 μs. The pressure is 10 mTorr and the peak power is 0.76 kW. In this figure, etching rate of SiO_2 and Si increase with increasing power ON period. However, etching rate of SiO_2 increases much slower than that of Si, resulting in a decreased etching selective of SiO_2/Si. Figure 2.19 (b) shows the etching rate of SiO_2 and Si as a function of the duration of afterglow period. The duration of active glow is fixed at 20 μs. It is found that

etching rate of SiO_2 and Si monotonically decreases with increasing afterglow period. The etching rate of SiO_2 decreases slower than that of Si, leading to an increased selectivity of SiO_2/Si.

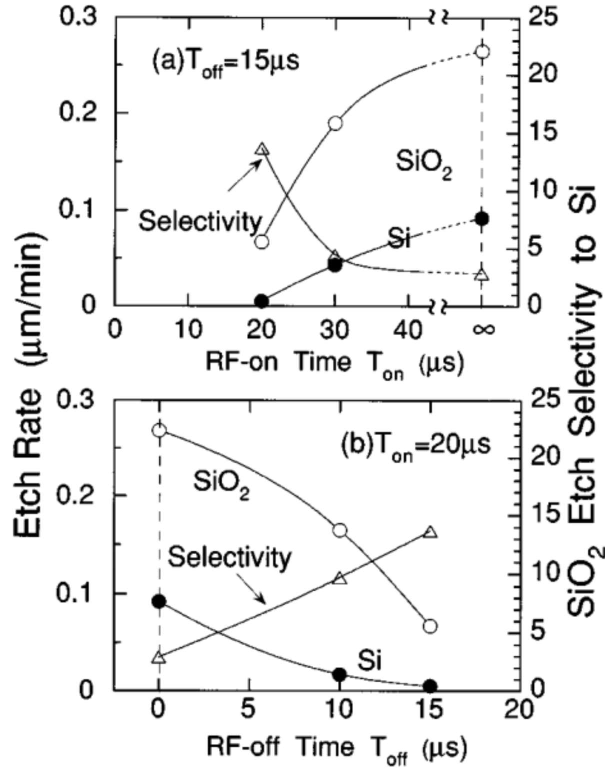

Figure 2.19 Etch rates of SiO_2 and Si and the selectivity as a function of (a) RF-on time for T_{off} = 15 μs and (b) RF-off time for T_{on} = 20 μs. P = 0.76 kW, 10 mTorr of 50% CF_4/50% H_2, V_{dc}=2400 V, z=9 cm, and T_w=100 °C [140].

Pulsed bias with cw source power can be used to reduce plasma-induced damage (PID) during plasma etching [100, 108]. In this configuration, ions with high energybombard the substrate only when the bias is ON to achieve anisotropic etching. Surface damage is reduced because ion bombardment time is reduced compared with continuous bias. During bias OFF period, plasma is still ON to produce reactants that re-saturate the surface. Plasma etching is alternating between anisotropic etching with ion

bombardment and surface saturation without ion bombardment, with reduce surface damage.

Pulsed bias is also believed to be a promising method to address aspect ratio dependent etching (ARDE). ARDE is due to the fact that the transport mechanisms of neutrals and ions inside microfeatures are different. The distribution of incident angles of neutrals is isotropic. However, the sidewall of the feature can block the diffusion of neutrals due to the so-called "shadowing effect," leading to a larger flux of neutrals at the bottom of the larger feature. Some of the neutrals can reach the bottom of the feature by reflecting from the sidewalls without reacting, through a well-known mechanism called "Knudsen transport". The flux of neutrals at the bottom of the feature is limited by such Knudsen transport mechanism and shadowing effect, which depends on the aspect ratio of the feature. Ion flux, however, is limited by differential charging, which can deflect or slow down bombarding ions before they reach the bottom of the feature [141, 142]. It has been shown that ARDE can be reduced by controlling ion/neutral ratio [143], which can be accomplished by using pulsed bias.

2.4.2 Extraction of negative ions in pulsed electronegative plasma

It is desired to extract negative ions out of plasma and onto the wafer to reduce charging effect which can cause profile distortion, such as notching, bowing, and micro-trenching during etching [144-147]. The mechanism of reducing differential charging in microfeatures by negative ions is well understood [148, 149]. Positive and negative ions have similar mass, so the fluxes of both positive and negative charges arriving at the substrate are similar. Differential charging on the sidewall of the trench can thus be

reduced. However, with cw bias applied on the substrate to enhance the etching rate, a capacitively coupled plasma may be ignited during the afterglow. Electrons are heated by such capacitive power and a plasma sheath is formed. Negative ions are confined by the plasma sheath and cannot reach the substrate.

Malyshev and Donnelly [60] investigated the dynamics of pulsed Cl_2 plasma in an ICP source with continuously RF bias applied on the sample stage. They found that in the late afterglow, the RF bias can sustain the plasma by a capacitively coupled discharge. Subramonium and Kushner [113, 150] conducted simulations using the same conditions and captured the experimental results of Malyshev and Donnelly, as shown in Figure 1.9. It is found that during the active glow and early afterglow, the temporal behaviors of n_e and T_e are almost same with and without RF bias applied on the sample stage. At the beginning of afterglow, both n_e and T_e decay quickly once the power is turned OFF. Without bias, n_e and T_e reach a very small value in the late afterglow. However, in the presence of RF bias, T_e turns around after 20 μs into the afterglow and n_e decays to a value that is higher than that without RF bias. That's because the power is distributed in a small number of electrons, leading to a relatively high T_e, and in turn causing the production rate of electrons by ionization to exceed the loss rate by attachment and diffusion to the wall. In the late afterglow, the plasma is sustained by the RF bias power and n_e reaches a steady state. They also found that with larger RF bias power, the capacitive mode occurs earlier.

Malyshev and Donnelly concluded that a bias using a high RF frequency would sustain a plasma, preventing negative ions from reaching the substrate. In order to allow negative ions to reach the substrate, a low RF frequency bias may be used. However, the

low RF frequency bias will broaden the ion energy distribution (IED). This is supported by Samukawa's experiments [151], where the etching rate of polysilicon in Cl_2 pulsed microwave plasma with continuous RF bias as a function of the RF frequency was investigated. It was found that with 600 kHz RF bias, the etching rate was greatly enhanced compared to that with no bias applied. However, the etching rate did not increase with the application of 2 MHz RF bias. That's because 2 MHz RF power would ignite a plasma, forming a sheath that prevents negative ions from reaching substrate surface to reduce charging effect.

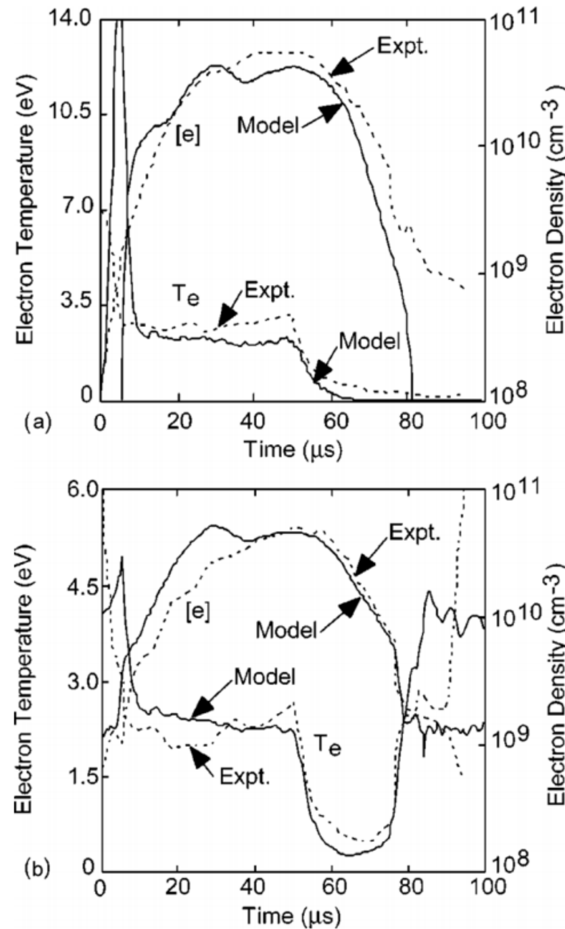

Figure 2.20 Temporal dynamics of electron temperature and electron density in (a) absence of bias and (b) presence of bias in Cl_2 ICP plasma. Sheath heating during the late after-glow leads to a capacitive discharge with higher electron temperature [113].

Kanakasabapathy et al. [152] reported that by applying RF bias in the afterglow of a pulsed plasma, positive and negative ions can be extracted out of the plasma and onto the substrate. In their experiment, they applied a low frequency RF bias (20 kHz) with a peak voltage of 225 V on the substrate in the afterglow of a pulsed Cl_2 plasma. The plasma was pulsed at 1 kHz with a duty cycle of 50%. The positive ions (denoted as letters in the figure below) are extracted during the cathodic half of the RF cycle and the negative ions (denoted as numbers) are extracted during the anodic half, as shown in Figure 2.21.

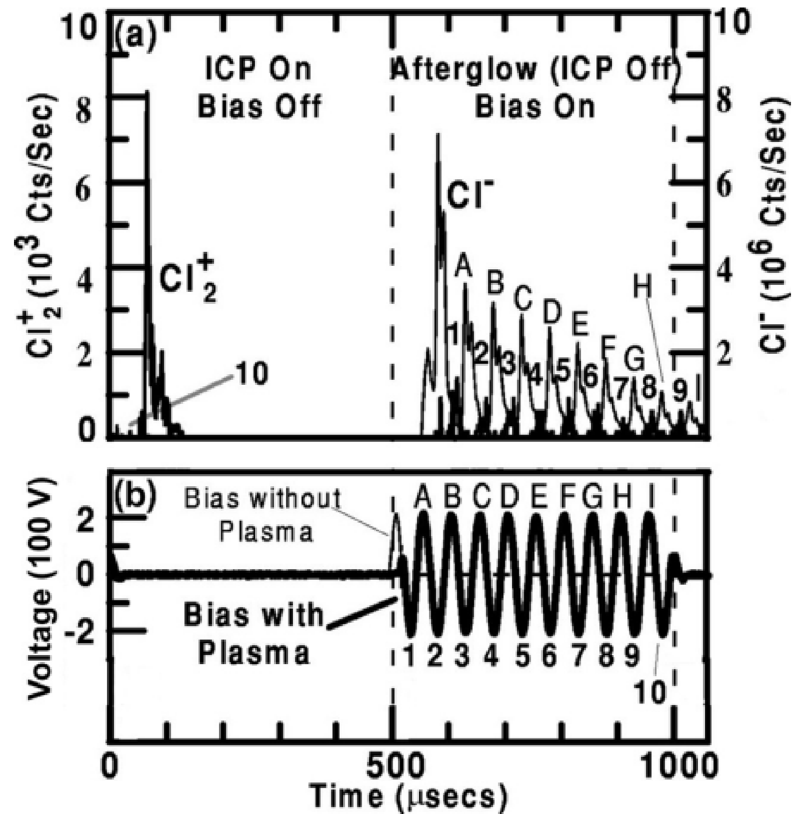

Figure 2.21 Mass spectrometer signals for (a) Cl_2^+ and Cl^-, and (b) applied bias voltage measured in a 1 mTorr, 5 sccm Cl_2 ICP plasma. The bias operates at an excitation frequency of 20 kHz with a peak voltage of 225 V [152].

2.4.3 *Atomic layer etching (ALE)*

Pulsed plasmas may find application in atomic layer etching (ALE). Atomic layer etching has been studied for more than 25 years. It was first reported by Meguro et al., using an electron beam to etch GaAs with Cl_2 absorbed on the surface [153]. Maki and Ehrlich, used an excimer laser instead of electron beam to etch GaAs with Cl_2 gas [154]. Sasaue et al. used ion bombardment to remove silicon with F atoms absorbed on the surface, but they found that the etching rate per cycle was less than a monolayer [155]. Atomic layer etching of silicon with one monolayer etched per cycle was first reported by Athavale and Economou. [156] They also studied the mechanism of atomic layer etching of silicon using molecular dynamics simulation [157]. According to their study, atomic layer etching consists of four consecutive steps, as shown in Figure 2.22:

(1). A clean single crystal silicon surface is exposed to chlorine gas and forms a monolayer of chlorine by chemisorption. It should be noted that the gas is turned ON only during this step and that chemisorption is self-limiting. It means that once all available surface sites are occupied, chemisorption stops. Only one monolayer of chlorine is formed on an intact crystalline silicon surface.

(2). The reactor chamber is evacuated, so that only the chlorine which is chemisorbed on the surface of silicon in step (1) can be involve in subsequent reaction.

(3). Use Ar^+ ion beam to bombard the chlorine modified surface. During this step, adsorbed gas react with underlying solid and a monolayer of the solid is removed. This step is also expected to be self-limiting. Ar^+ bombardment only removes the surface layer of silicon which is bonded to the chemisorbed chlorine. Once the top chlorinated layer is

removed, ion bombardment does not react or sputter the underlying silicon layer (selectivity). This step is best executed with monoenergetic Ar^+ ions.

(4). The etching product during step (3) is pumped out of the chamber, completing one cycle of etching. The cycle can be repeated to etch the desired number of monolayers.

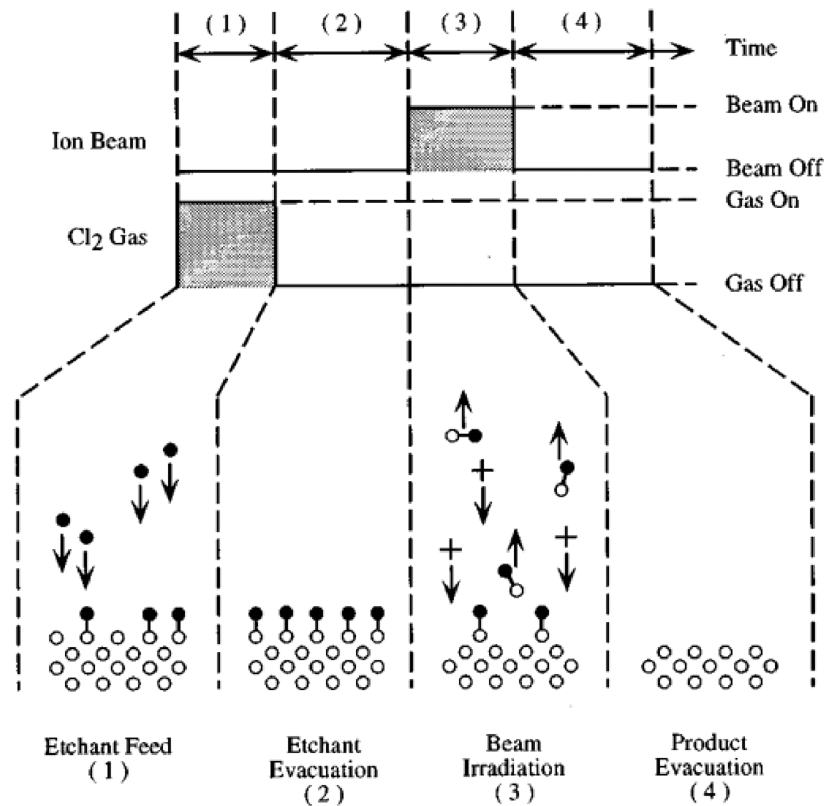

Figure 2.22 Schematic of the ALET process. The filled circles represent Cl atoms; the open circles represent Si atoms, and + represent Ar^+ ions [156].

This approach of atomic layer etching requires very long time for each cycle (~150 s) [158]. Even though pulsed gas valves and fast switching mass flow controllers

have well developed, the process is still too slow to be widely used in manufacturing [159-161].

A new method of atomic layer etching was proposed by Economou and Donnelly, as shown in Figure 2.23 [100, 108]. The main plasma can be switched between continuous wave (cw) mode and pulse mode. The duration of cw and pulse mode is 1 s and 0.5 s, respectively ("RF Main" in Figure 2.23). During the pulsed mode, an auxiliary source can be employed to help sustaining the plasma ("RF AUX" in Figure 2.23). When the main plasma is operated in cw mode with halogen containing gas, a self-limiting halogenated layer is formed on the surface without etching since the ion energy is below the ionassisted etching threshold. Once the surface of silicon is halogenated, the main plasma is switched to pulse mode with synchronous DC ("Pulse DC-1" in Figure 2.23) bias or cw DC bias ("Pulse" DC-2 in Figure 2.23) on the top boundary electrode. Monoenergetic ions are formed and bombard the halogenated silicon surface, removing the layer of halogenated silicon. Since the ion energy is monoenergetic with narrow energy spread, ions will only sputter away the halogenated layer without damaging the silicon under the top layer. Compared with the traditional atomic layer etching, this method can overcome the problems of slow etching cycle time and substrate damage.

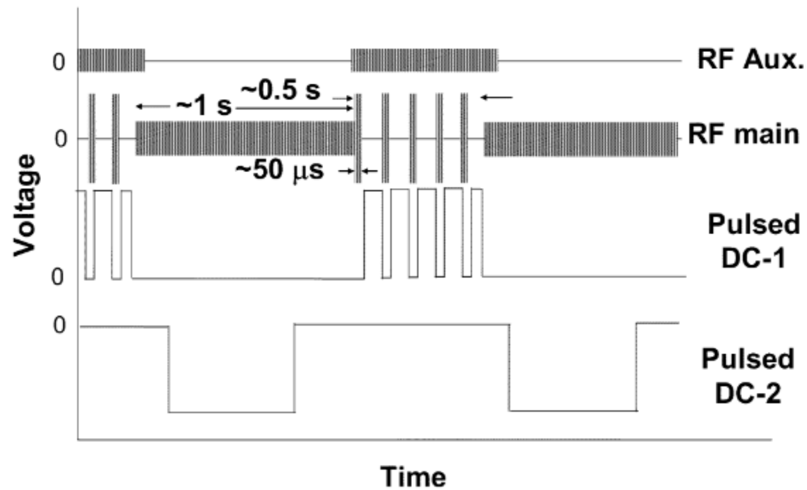

Figure 2.23 Schematic of the fast ALET process with pulse plasma and pulsed bias [100, 108].

Atomic layer etching of Si and SiO_2 using Cl_2/Ar plasma was reported by Gottscho et al. They used Lam Research's commercial etching tool 2300 Kiyo plasma etching chamber with a transformer coupled plasma source [162]. By changing bias voltage from 0 V to 120 V, they could achieve etching depth per cycle of 5 A to 20 A for silicon and 0 A to 2 A for SiO_2, as shown in Figure 2.24. They also reported that by using atomic layer etching, they can achieve infinite selectivity of single crystal silicon to thermal silicon oxide, which cannot be obtained by using continuous plasma, as shown in Figure 2.25.

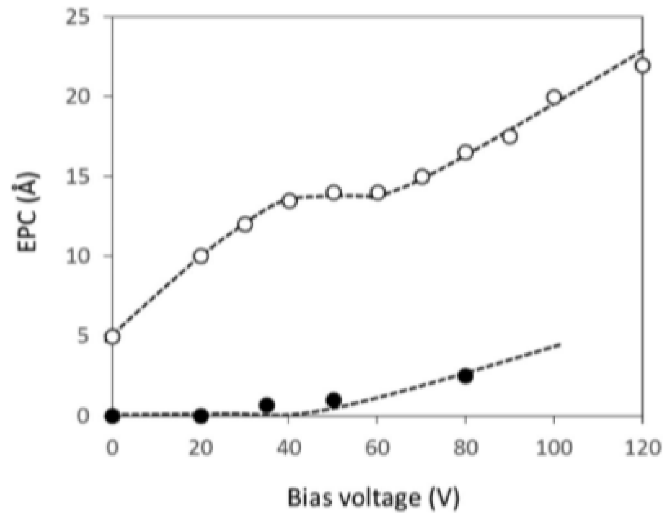

Figure 2.24 Etching depth per cycle (EPC) for silicon (open circles) and silicon oxide (solid circles) as a function of RF bias [162].

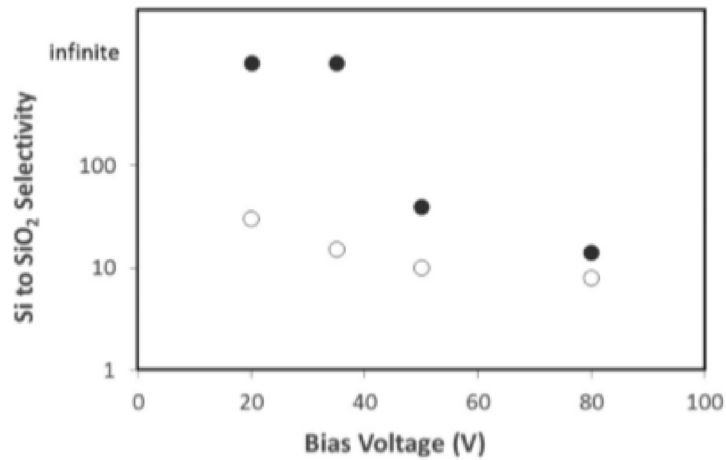

Figure 2.25 Selectivity of single crystal silicon to thermal silicon oxide as a function of RF bias voltage. ALE results (full circles) and continuous process results (open circles) are compared [162].

Oehrlein et al. [163] reported atomic layer etching of SiO_2, with selectivity over Si, using fluorocarbon gas [164]. They injected a defined number of C_4F_8 molecules in a steady-state Ar plasma to form a fluorocarbon (FC) layer, and applied synchronized bias to enable Ar^+ bombardment to induce reaction of SiO_2 with the fluorocarbon layer,

thereby etching SiO_2. Surface characterization was done using XPS and in-situ ellipsometry.

Figure 2.26 shows a typical thickness evolution of the SiO_2 layer. Initially, Ar plasma is operated in cw mode for 10 seconds. Then C_4F_8 gas is injected into the steady-state Ar plasma for 1.5s. Fluorocarbon (FC) layer with a thickness of 5 A is formed on the surface of SiO_2 during the remaining 8.5 s of Ar plasma. After 10 seconds, a small RF self-bias voltage (5, 10, and 15 V) is applied for 35 s, yielding maximum ion energies of 20, 25, and 30 eV. Ar^+ ions bombard the SiO_2 surface modified by the fluorocarbon (FC) layer, etching the SiO_2 film. Physical sputtering of the unmodified SiO_2 with such low ion energies is negligible. Within one cycle, the etching rate of SiO_2 decreased from 1.3 A/s to 0.2 A/s as the fluorocarbon (FC) layer was removed, as measured by in-situ ellipsometry, as shown in Figure 2.27. They also obtained selective etching of SiO_2 over Si by using C_4F_8 and CHF_3 gas, as shown in Figure 2.28.

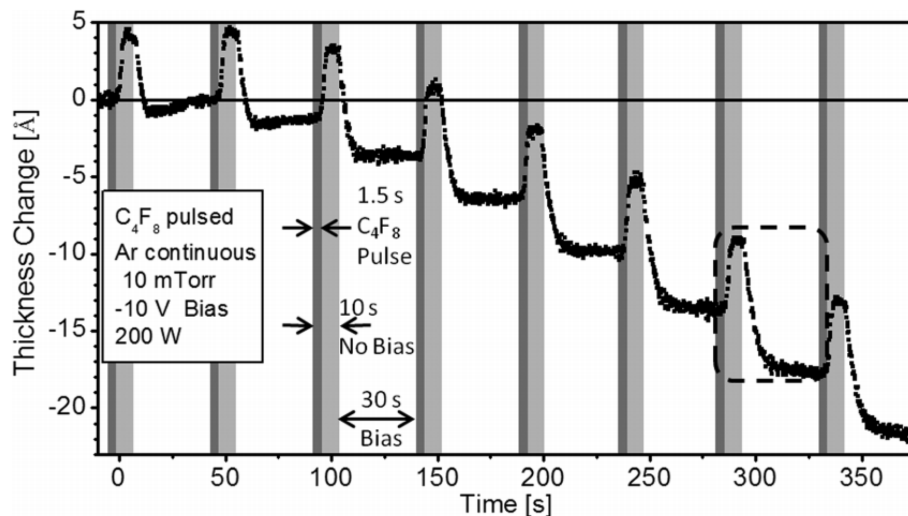

Figure 2.26 Example of thickness evolution during eight cycles of a SiO_2 ALE process [163].

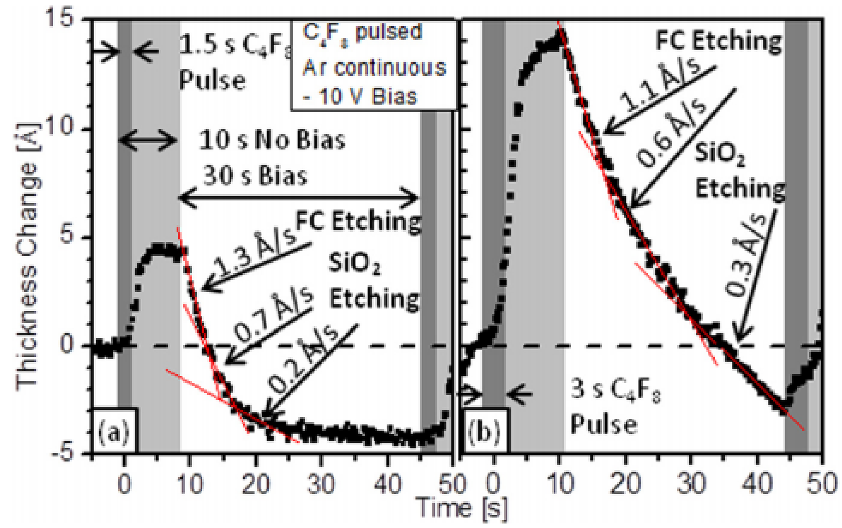

Figure 2.27 Thickness changes of SiO_2 during one cycle for two thicknesses of deposited FC layer achieved by changing the C_4F_8 pulse time from (a) 1.5 s to (b) 3 s. The FC pulse is injected at the beginning of the deposition step. Bias is applied Eight seconds after the pulse ends [163].

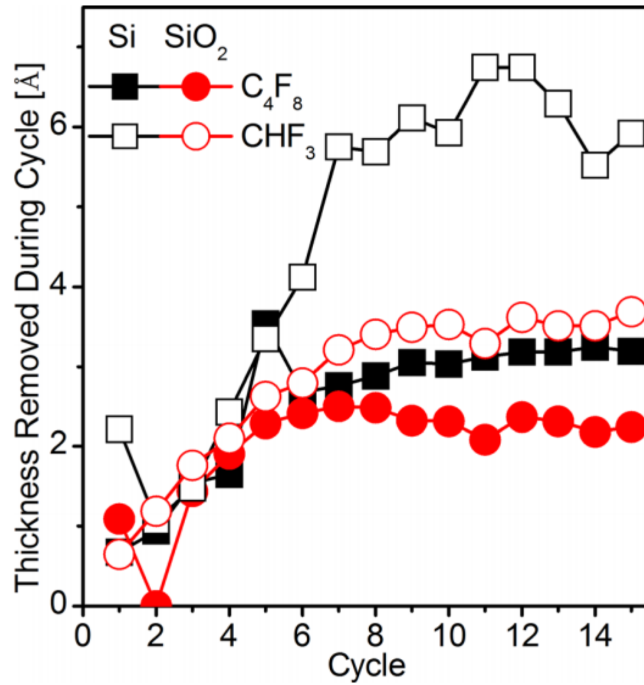

Figure 2.28 Thickness removal during the cycle as determined by ellipsometry for ALE of Si and SiO_2 using C_4F_8 and CHF_3 at 25 eV ion energy and 40 s etching step length [164].

2.5 Plasma ignition delay

Ignition delays in pulsed CF_4/Ar ICPs in the absence of a Faraday shield have been reported by Wang et al. [165], and attributed to a capacitive-to-inductive (E-H) mode transition. Tuszewski [166] reported instabilities in low-pressure electronegative discharges. Liebermann [167] and Chabert [130, 168] subsequently showed, using a global model, that these instabilities were a result of E-H transitions. E-H transition instabilities were attributed to differences in the production/loss rate of electrons and negative ions, causing the plasma to oscillate between inductive and capacitive discharge modes. Electron density builds up rapidly due to ionization and a quasi-equilibrium 'inductive' state (high electron density) of discharge is attained. Negative ion density continues to increase at a much slower rate, disturbing the equilibrium. Electrons are then lost rapidly due to attachment and the discharge operates in a quasi-equilibrium low electron density 'capacitive' mode. Negative ions are lost at a much slower rate until the inductive mode is re-established [130, 167, 168]. In the present work, the observed ignition delay in the tandem plasma system was not caused by an E-H mode transition since both plasma sources were equipped with a Faraday shield that precluded the E mode of the discharge.

CHAPTER 3

EXPERIMENTAL SETUP

3.1 Plasma source

Figure 3.1 shows a schematic of the experimental apparatus, consisting of two co-axial (tandem) inductively coupled plasma (ICP) sources. The main ICP (lower plasma) was powered by a 3-turn spiral coil in a 17.8 cm long, 8.6 cm inside diameter water-cooled Al_2O_3 tube [24, 89]. The discharge tube was connected to a cubical stainless steel chamber through a water-cooled adaptor flange. The 5.08 cm-diameter water-cooled stainless steel sample stage had a 2.64 cm-diameter hole in the center, allowing a Langmuir probe to pass through. An auxiliary ICP (upper plasma) was ignited by a 11.5-turn coil in a 33 cm long, 7.94 cm inside diameters water-cooled Al_2O_3 tube through an L-type matching network. The two ICPs were powered individually, each using a separate radio frequency (RF) power amplifier (ENI, model A500) driven by a function generator (Hewlett-Packard 3325A). Forward and reflected power was monitored by in-line power meters (Bird, model 43). The main ICP was powered at 13.56 MHz and the auxiliary ICP was powered at 13.26 MHz. The 300 kHz difference in frequency between the two sources is large enough that noise in the electronics, including the Langmuir probe signal, due to RF pickup on wires and ground loops are not a serious problem, yet 13.26 MHz is close enough to 13.56 MHz that the RF chokes in the Langmuir probe (designed for 13.56 MHz) still provide some blockage of any residual small RF currents collected at the fundamental and harmonics so that the probe provides reliable results.

Nonetheless, there is some added noise when both sources are operated, due to this effect. Faraday shields on the outside cylindrical surfaces of the alumina tubes of both ICPs minimized capacitive coupling between the coils and the plasmas. The Faraday shields were electrically grounded. A biasable "boundary electrode" was placed on the top of the upper source with a quartz window 100 mm in diameter. A Kepco bipolar DC power supply was used to provide DC bias up to ± 100 V.

The plasma sources were separated by a 9.53 cm-diameter grounded grid. Three different grids were used: Grid A used for Cl_2 and Ar plasma was made of woven tungsten wire, and was 90% transparent with square holes 2.4 mm on a side. Grid B was also made of woven tungsten wire, and was 81% transparent with 230 μm square holes. Grid C, used for SF_6, CF_4/O_2 and O_2 plasmas, was made of woven stainless steel wire (tungsten would be etched in F atom containing plasmas) and was 68.9 % transparent with 2.1 mm square holes. This arrangement allowed cross-talk between the two plasmas depending on their relative plasma potentials, V_p [169]. The grid also provides additional grounded surface in the plasma to help minimize changes in the plasma potential during Langmuir probe measurements when large electron currents are drawn.

Process gas was injected through a hole in the boundary electrode at the upper end of the auxiliary ICP and was pumped through the lower end of the main ICP by a 300 l/s turbomolecular pump (EBARA ET300WS) backed by a dry pump (Edwards IH80). The base pressure was in the low 10^{-6} Torr range, as measured by an ion gauge (JC Controls IG4500). The operating pressure (set by a throttle valve) was monitored by an MKS 629 (0.1 Torr full scale) capacitance manometer.

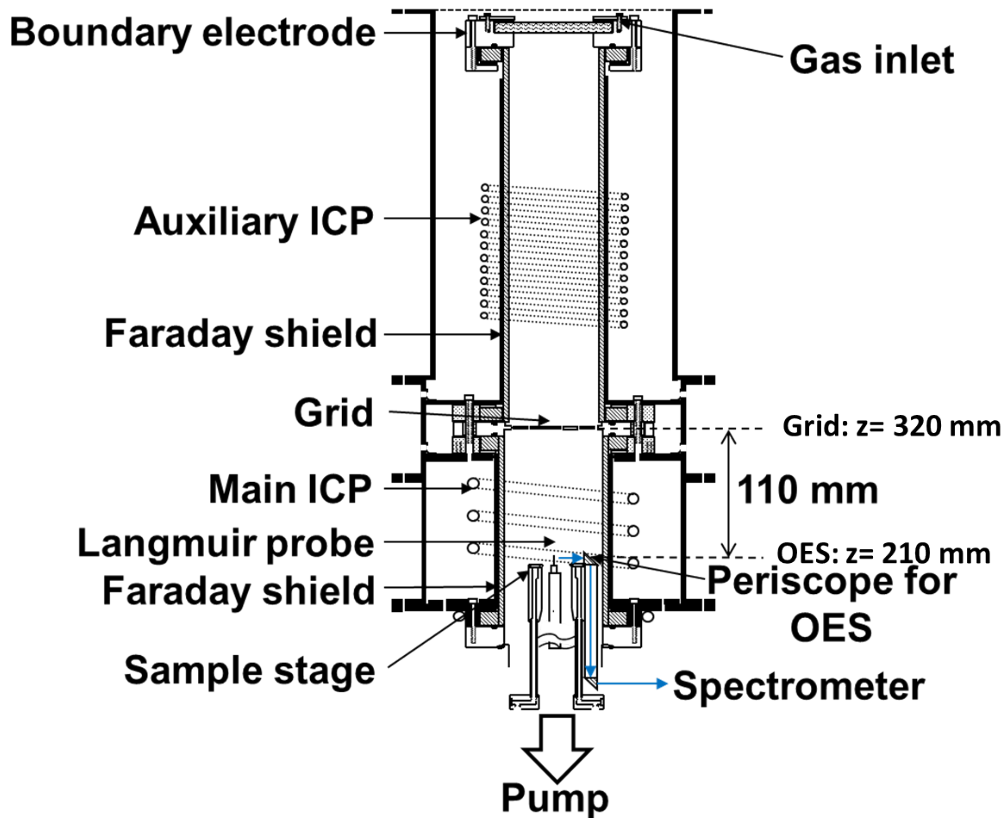

Figure 3.1 Schematic of the experimental apparatus with dual tandem inductively coupled plasma (ICP) sources. The auxiliary (upper) ICP is separated from the main (lower) ICP by a metal grid.

3.2 Operating conditions

3.2.1 Operating conditions for controlling EEDF in continuous wave Ar plasma

During the experiments of controlling EEDF in continuous wave Ar plasma, the flow rate of Ar gas was 80 standard cm^3/min (sccm). The pressure was maintained at 10 mTorr, 20 mTorr or 40 mTorr by a throttle valve. The boundary electrode was either grounded or biased with 90 V DC. Both plasmas were powered in continuous wave mode. The main ICP in which the EEPFs were investigated was supplied with 500 W of 13.56 MHz RF power. The auxiliary ICP was operated with a power of 100 W at 13.26 MHz.

3.2.2 *Operating conditions for controlling the EEDF in pulsed Ar plasma*

For the study of controlling EEDF in pulsed Ar plasmas, the flow rate of Ar gas was 80 sccm. For a measured pressure of 14 mTorr at the center of the lower plasma, the pressure at the center of the upper plasma was estimated to be 16 mTorr. The 13.56 MHz power supplied to the main ICP in which the EEDFs were investigated was pulsed at 10 kHz (100 μs pulsed period) with a duty cycle of 20% (20 μs power on, 80 μs power off). The nominal time-averaged power to the main plasma was 100 W. The auxiliary plasma was operated in a continuous wave (cw) mode with a power of 500 W at 13.26 MHz. The sheath thickness near the grid was estimated to be ~200 μm, which is much smaller than the holes of the grid A used to separate the two sources.

3.2.3 *Operating conditions for studying ignition delay in pulsed electronegative plasmas*

For the studies of ignition delay in pulsed electronegative plasmas, the following working gases were employed: 25 sccm, Matheson 99.99% purity Cl_2, 25 sccm SF_6, 30 sccm O_2, or 30 sccm Matheson 80% CF_4/20% O_2). The pressure drop between the center of the upper source and the center of the lower source was estimated to be ~ 2 mTorr for Cl_2 gas. The power supplied to the main ICP was pulsed at a frequency of 1 kHz (1000 μs pulse period), with variable duty cycle. The auxiliary ICP was powered continuously with a given power. Base case conditions (Table 3.1) were: pressure = 5 mTorr, peak power to the main ICP = 500 W (13.56 MHz), and continuous wave (cw) power to the auxiliary ICP = 500 W (13.26 MHz).

Table 3.1 Base case parameters and range investigated

Parameter	Base case	Range Investigated
RF frequency of main ICP	13.56 MHz	
RF frequency of auxiliary ICP	13.26 MHz	
Pulse frequency of main ICP	1 kHz	
Gas flow rate	25 sccm	
Pressure	5 mTorr	2.5 ~ 20 mTorr
Duty cycle of pulsed main ICP	99 %	20 % ~ 99.9 %
Peak power of pulsed main ICP	500 W	100 W~ 500 W
CW power of auxiliary ICP	500 W	100 W ~ 500 W
Metal grid	(A)	(A) 2.4 mm holes, 90% transparency (B) 230 μm holes, 81% transparency (C) 2.1 mm holes, 68.9% transparency

3.3 Plasma diagnostics

3.3.1 Langmuir probe

Langmuir probes (LP) are widely used to measure plasma parameters such as plasma density, electron temperature, plasma potential, and the electron energy distribution function (EEDF). A Langmuir probe consists of a bare wire or metal disk, which is immersed in the plasma. By ramping a bias voltage on the probe with respect to a reference electrode, an I-V curve is collected, which can be used to determine plasma parameters.

A Langmuir probe (Scientific Systems Smartprobe, with modifications to reduce the probe size, as discussed in ref. [170]) was used to measure electron and positive ion densities (n_e and n_+), electron temperature (T_e) and the electron energy probability function (EEPF). The cylindrical tungsten probe tip had a diameter of 0.18 mm and an

exposed length of 2 mm for Ar plasmas and 6.5 mm for chlorine plasmas. A reference electrode and RF chokes minimized distortion of the *I–V* characteristic due to any residual oscillations of the plasma potential. Fast data acquisition electronics enabled averaging of 100s of *I-V* characteristics (at a given location and for given plasma conditions) to reduce noise. Plasma parameters (n_e, n_+, *and* T_e) were obtained by different procedures depending on the plasma electronegativity ($\alpha=n_-/n_e$). For a highly electronegative plasma ($\alpha \geq 1000$) that formed during the afterglow period, the plasma parameters were obtained by fitting the *I-V* curve and its second derivative using the procedure outlined by Bredin et al. [171] (see Appendix).

For plasmas with low electronegativity or electropositive plasma (argon), n_e and T_e were extracted from the EEPF. The EEPF is given by $f_p(\varepsilon) = \varepsilon^{-1/2} f(\varepsilon)$, where $f(\varepsilon)$ is obtained from the second derivative of the probe electron current I_e [1], written as

$$f(\varepsilon) = \frac{2m_e}{e^2 A}\sqrt{\frac{2\varepsilon}{m_e}}\, d^2 I_e/dV^2. \qquad (3.1)$$

In eq. (3.1), m_e is the electron mass, A is the probe exposed area, and e is the elementary charge. Voltage V is the applied probe voltage referenced to the plasma potential at the probe location. For a Maxwellian distribution of electron energies, a semi-log plot of $f_p(\varepsilon)$ vs. ε yields a straight line. The electron density (n_e), and the average electron energy $<\varepsilon>$ are calculated by integrating the electron energy distribution function $f(\varepsilon)$ as

$$n_e = \int_0^\infty f(\varepsilon) d\varepsilon \text{ and} \qquad (3.2)$$

$$<\varepsilon> = \frac{1}{n_e}\int_0^\infty \varepsilon f(\varepsilon) d\varepsilon. \qquad (3.3)$$

The effective electron temperature (T_e) is computed as 2/3<ε>. The ion density is obtained using Laframboise's orbital motion limited (OML) theory for a collisionless sheath [136] :

$$n_i^+ = \xi\left(\frac{r_p}{\lambda_d}, \frac{V-V_p}{kT_e}\right)\frac{I_i^+}{eA}\sqrt{\frac{2\pi M_i}{kT_e}}\,, \tag{3.4}$$

where ξ is a correction factor that depends on a dimensionless potential and the ratio of cylindrical probe radius to plasma Debye length, I_+ is the ion saturation current, and M_i is the ion mass.

To obtain the spatial distribution of plasma properties, the probe was moved in the main ICP along the z-axis (Figure 3.1) from 120 mm below the grid (z = 200 mm) to 20 mm below the grid (z = 300 mm). To obtain time-resolved plasma properties, the probe was operated in 'boxcar' mode using an external trigger signal. Plasma parameters were collected on the discharge axis ($r = 0$), in the main ICP, 110 mm (z = 210 mm) below the grid separating the two sources.

3.3.2 Optical emission spectroscopy

Optical emission spectroscopy is one of the basic tools used for plasma diagnostics. It can be used to identify and monitor the number density of different chemical species in plasma by measuring the intensity of light from the electronic transitions of atoms and molecules. It was first used in plasma etching application by Harshbarger et al. in 1977 [172].

Optical emission spectroscopy was also used in this work to monitor key plasma species. A periscope consisting of two prisms was used to direct the light from the plasma to the entrance slit of a monochromator. The slit width was set to 1000 μm, which, with a 1200 grooves/mm grating, provided a resolution of about 2 nm. Light dispersed by the grating was detected by a GaAs photomultiplier tube (RCA C31034). The current output of the photomultiplier tube was measured as a voltage across a 3 kΩ load resistor, using an oscilloscope. The time constant of the detector circuit was estimated to be ~ 0.3 μs, which is much smaller than the observed rise time of the plasma emission signal (10 μs). Atomic emission lines of Cl (837.5 nm; 4p $^4D^o \rightarrow$ 4s ^4P), O (777.1 nm; 3p $^5P \rightarrow$ 3s $^5S^o$), and Ar (750.4 nm, $2p_1$ Paschen series) were used to monitor the ignition and extinction of pulsed chlorine, oxygen, and argon plasmas, respectively. F emission at 685.6 nm (3p $^4D^o$ $\rightarrow$ 3s ^4P) was used to monitor fluorine-containing (SF_6 and 80% CF_4/20% O_2) plasmas.

CHAPTER 4

SYNERGISTIC BEHAVIOR OF DUAL TANDEM INDUCTIVELY COUPLED PLASMAS OPERATED IN A CONTINUOUS WAVE MODE

In this chapter, synergistic behavior of the dual tandem ICPs operated in continuous wave (cw) mode is discussed. Langmuir probe measurements were carried out in the main ICP. Spatial plasma parameters such as plasma potential, plasma density and EEPFs in the main ICP were obtained as a function of gas pressure and bias applied to a boundary electrode.

4.1 Spatial distribution of plasma potential (V_p)

The spatial distribution of plasma potential V_p at 10 mTorr was measured by Langmuir probe with only the main ICP on, and both ICPs on, with and without 90 V boundary electrode bias, as shown in Figure 4.1. The highest V_p is at the center of the main ICP without any applied bias on the boundary electrode. It is seen that V_p is higher with both plasmas ON. That's because the grid opening size (2.4 mm) is much larger than the sheath thickness (~300 μm by Child Law). At the center of the grid opening, V_p is ~16 V (Figure 5.4). The grid then acts as a boundary electrode which is biased with positive voltage, shifting the V_p of the main ICP when both plasmas are powered. When a 90 V bias is applied on the boundary electrode, V_p is shifted to a higher value. The mechanism of shift in V_p with applied bias on a boundary electrode is well understood

[173-175]. Electrons are extracted by the positive bias, resulting in an increase in V_p; thus, all but the highest energy electrons will be confined in the plasma.

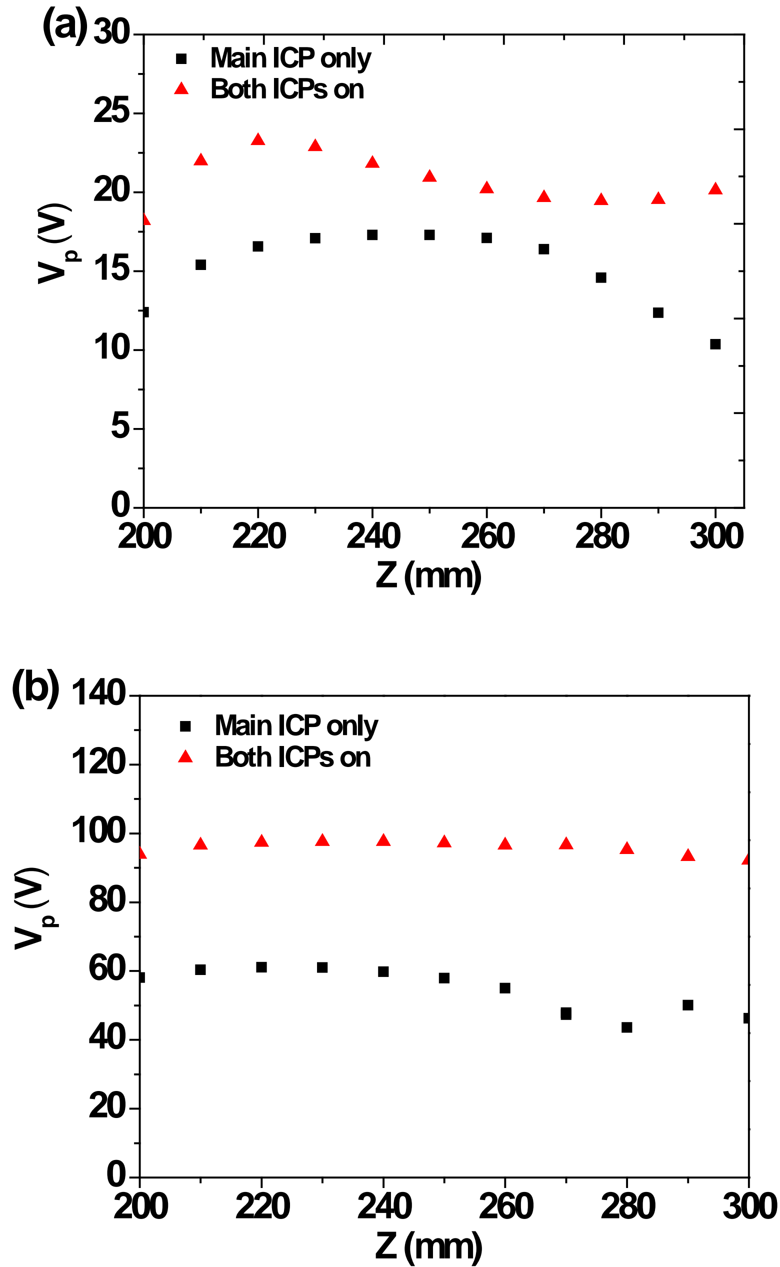

Figure 4.1 The plasma potential (V_p) profile along z axis in the main ICP chamber with/without 90 V boundary electrode bias for main ICP only (500 W) and both ICPs on (auxiliary ICP power 100 W) at the pressure of 10 mTorr. (a): 0V bias. (b): 90V bias.

4.2 Spatial distribution of plasma density

Figures 4.2 and 4.3 present space-resolved electron and ion (n_e and n_i) densities along the z axis of the main ICP at 10 mTorr with and without 90 V boundary electrode bias, respectively. The highest n_e and n_i were recorded at z = 240 mm. n_i and n_e differ by less than 20%. The plasma density with only the lower plasma ON is larger than with both plasmas ON. This is likely due to the net effect of bidirectional plasma transport through the metal grid. With a 90 V boundary electrode bias, n_e and n_i in the lower plasma increase substantially because of the shift in plasma potential, which results in better confinement of electrons. Without any boundary electrode bias, the plasma density drops when both plasmas are on. With both plasmas on, and with 90 V applied to the boundary electrode, n_e and n_i are higher than the summation of the densities when each of the sources is acting alone. That's probably because, with 90 V bias applied on the top boundary electrode, the two plasmas become more isolated because the potential barrier between the plasmas is increased. Only electrons with very high energy in the auxiliary ICP can overcome the potential barrier and be injected into the main ICP. Such electrons cause ionization in the main ICP. The electron generation rate in the main ICP exceeds the loss rate by transport from the main ICP to the auxiliary ICP, leading to an increase in both electron and ion density in the main ICP.

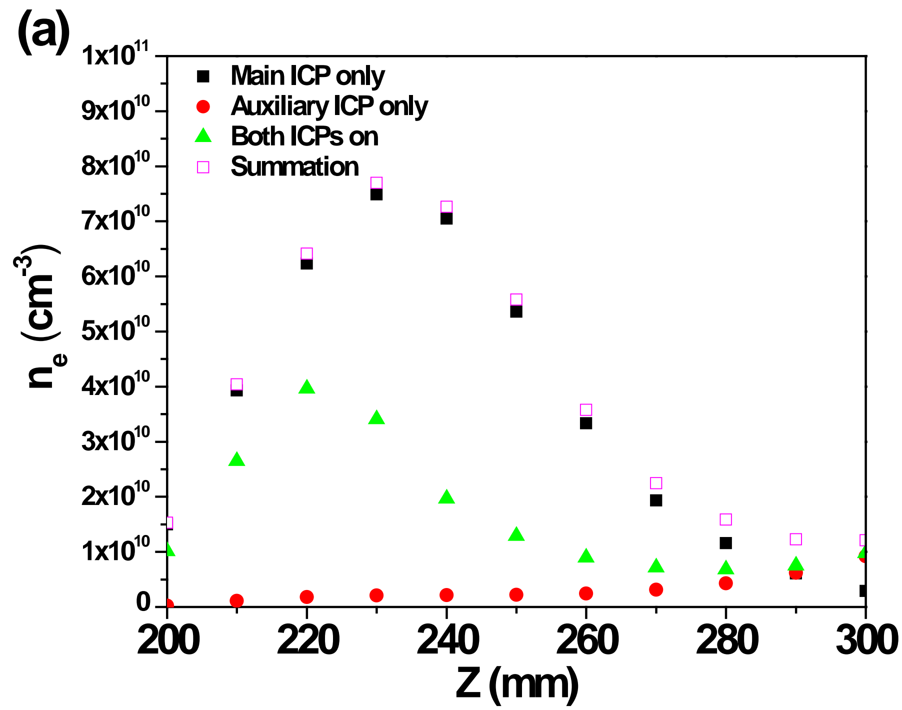

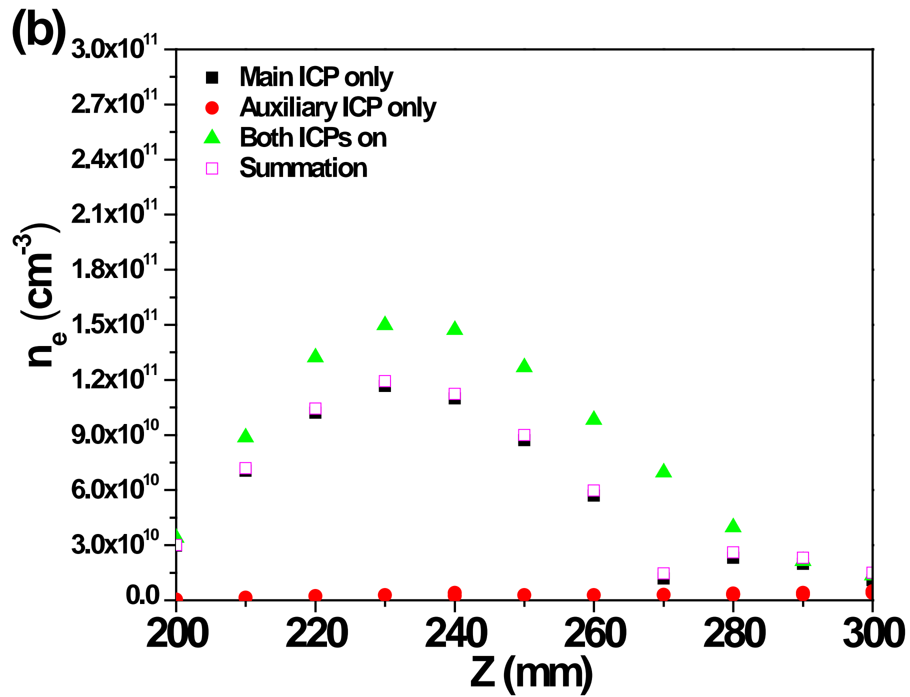

Figure 4.2 The electron density (n_e) profile along z axis in the main ICP chamber of argon discharge with/without 90 V boundary electrode bias at the pressure of 10 mTorr for main ICP only (500 W), auxiliary ICP only (100 W) and both ICPs on. (a): 0 V bias. (b): 90 V bias.

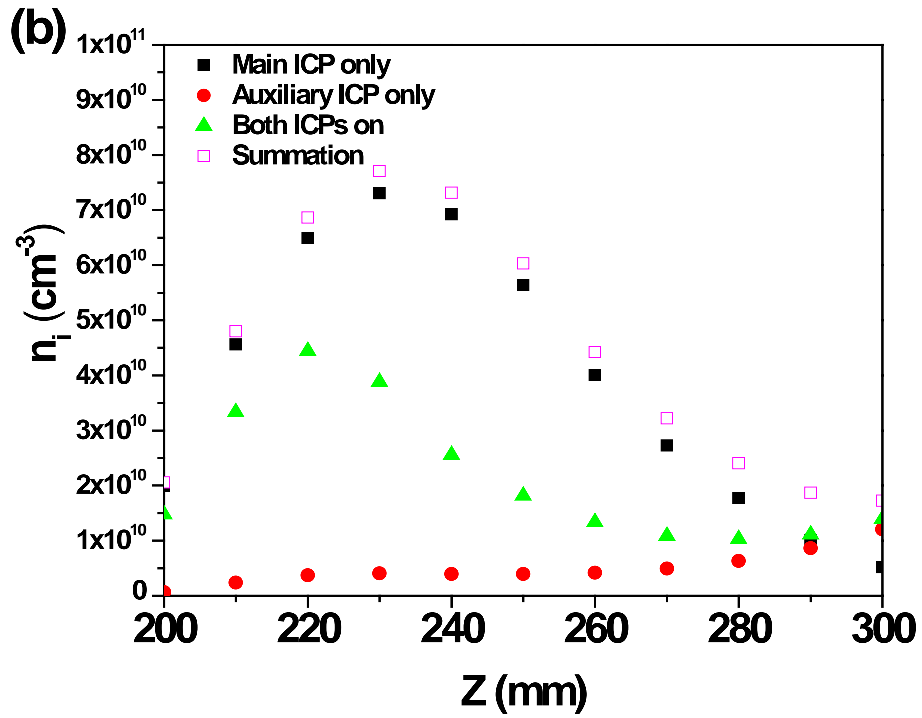

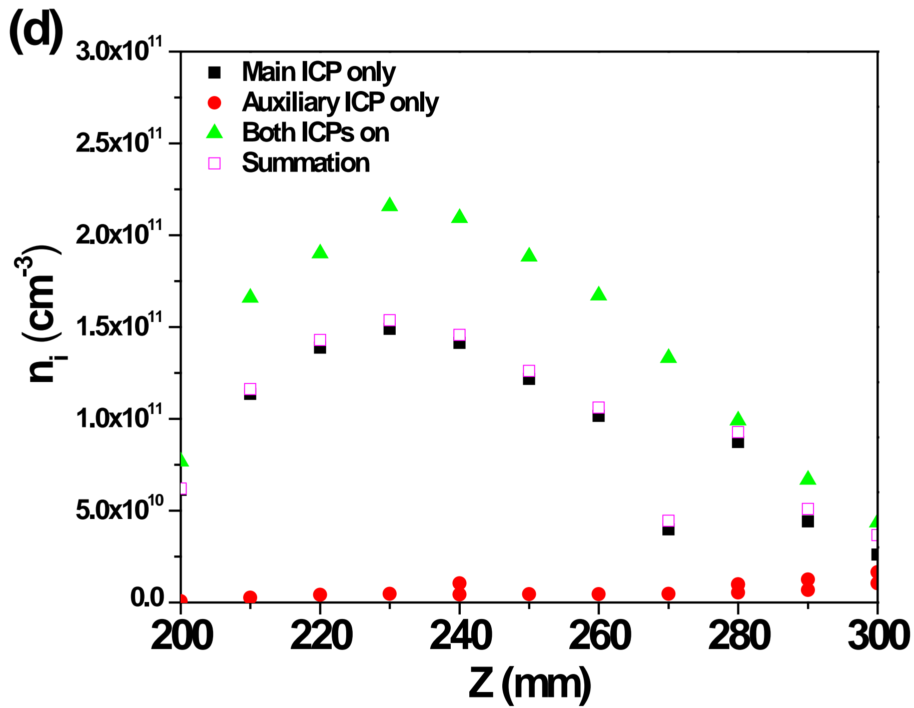

Figure 4.3 The ion density (n_i) profile along z axis in the main ICP chamber of argon discharge with/without 90 V boundary electrode bias at the pressure of 10 mTorr for main ICP only (500 W), auxiliary ICP only (100 W) and both ICPs on. (a): 0 V bias. (b): 90 V bias.

4.3 Spatial distribution of electron temperature (T_e)

The spatial distribution of T_e for different pressures (10 mTorr, 20 mTorr or 40 mTorr) and bias on the boundary electrode (0 V and 90 V) is presented in Figure 4.4. Bias on the boundary electrode did not have an effect on electron temperature for only the main ICP on, and for both plasmas on. In the middle (z = 240 mm) and top edge (z = 300 mm) of the main ICP, T_e with both ICPs on is the same as that with only the main ICP on. However, at the bottom edge of the main ICP (z = 200 mm), T_e with both ICPs on is higher than that with only the main ICP on. As the pressure increases, the electron temperature decreases because the ion losses are reduced at higher pressure and the plasma can be self-sustained at lower T_e.

4.4 Spatial distribution of EEPFs

EEPFs at the center of the lower plasma (z = 250 mm) at 10 mTorr with different boundary electrode bias are shown in Figure 4.5. The EEPFs are found to be typical bi-Maxwellian. Without any bias on the boundary electrode, the low energy electrons are depleted. This is likely because low energy electrons in the main ICP are replaced by hot electrons injected from the auxiliary ICP. As the boundary electrode bias voltages increases, the low energy electron population also increases; with 90 V bias on boundary electrode, ultrahigh energy electron flux injected from auxiliary ICP to the main ICP prompts ionization process, producing more low energy electrons. A seemingly substantial enhancement in the total electron density occurs with increasing bias on boundary electrode, which is consistent with the electron density (n_e) measurements.

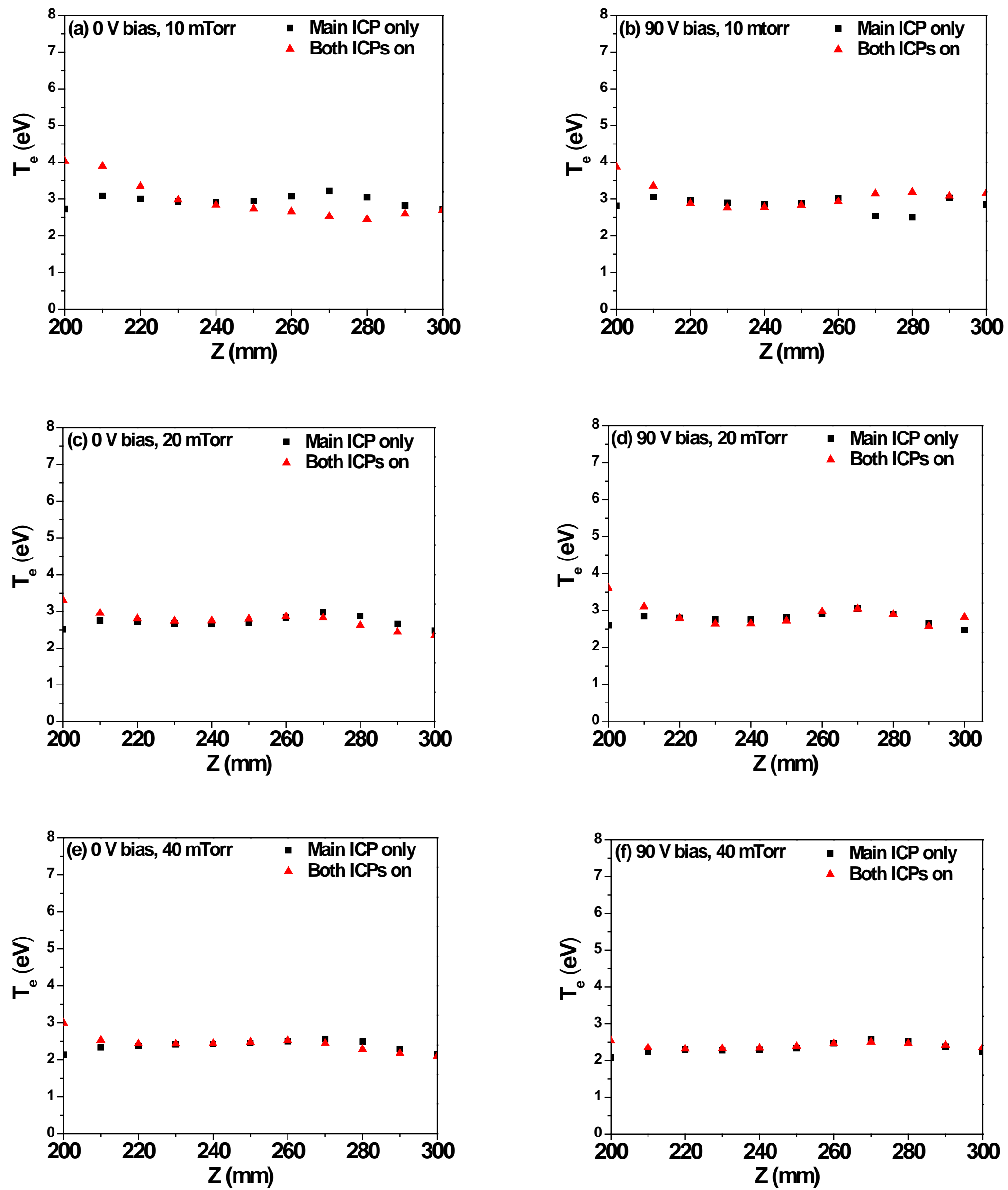

Figure 4.4 The T_e profile along z axis in the main ICP chamber with different boundary electrode bias and pressure for main ICP only and both plasma on. (a): 0V bias, 10 mTorr. (b): 0V bias, 20mTorr. (c): 0V bias, 40 mTorr. (d): 90V bias, 10 mTorr. (e): 90V bias, 20mTorr. (f): 90V bias, 40 mTorr. The main ICP was operated at 500 W and the tandem ICP was operated at 100W.

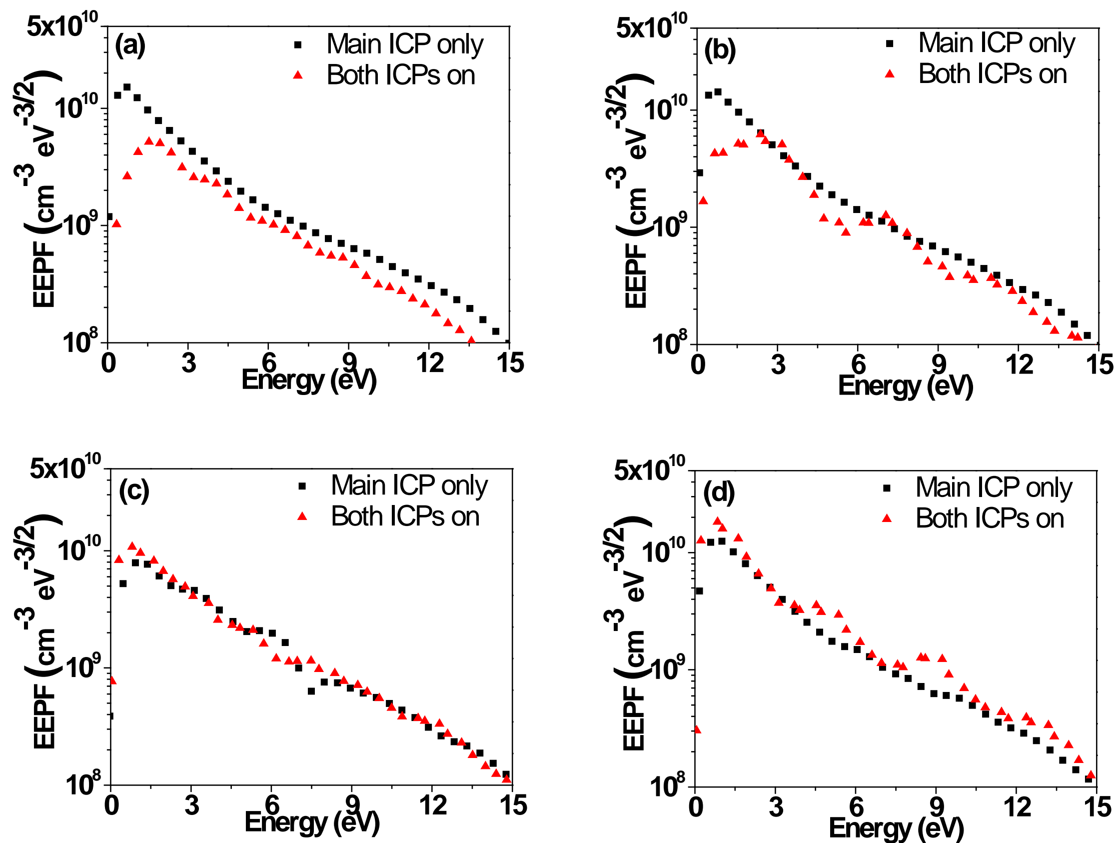

Figure 4.5 EEPFs for main ICP only (500 W) and both plasmas on (Upper ICP power 100 W) with different boundary electrode at the position of 250 mm in the main ICP. (a): 0 V bias. (b): 20 V bias. (c): 40 V bias. (d): 55 V bias. The pressure is 10 mTorr with argon flow rate of 80 sccm.

4.5 Hysteresis of ion current with bias on boundary electrode

The evolution of I-V curves close to the grid (z = 300 mm, 20 mm below the grid) obtained from Langmuir probe as a function of the bias voltage applied to the boundary electrode was studied. I-V curves with different boundary electrode bias are shown in Figure 4.6(c). At high bias voltages, two steady states of ion saturation current are observed close to the grid, one with ~ 4X higher current than the other. However, the electron currents are identical.

It was found that the ion saturation current exhibits hysteresis. As the bias voltage is increased, the ion current increases slowly up to ~95 V. At that voltage a sudden jump (by a factor of 3) is observed. As the bias voltage is decreased, the ion current slowly decreases down to ~40 V at which point it suddenly drops to the corresponding value recorded with ascending bias voltage. Figure 4.6(a) and Figure 4.6(b) show hysteresis behavior when only the upper plasma is on, and with both plasmas on, respectively.

The hysteresis behavior of E mode to H mode transition in ICP has been reported by Liebermann et al. [176] They concluded that the hysteresis is because two modes of operation can exist in an ICP discharge, namely, a low-density mode knows as the E mode and a higher density mode known as the H mode. The transition between these two modes exhibits hysteresis. In our case, when boundary electrode bias is zero, only a small amount of ions that can overcome the potential barrier at the position of the grid will be injected from the auxiliary ICP to the main ICP. As the bias on boundary electrode increases, the plasma potential of auxiliary ICP increases and ions are accelerated towards the main ICP. When the bias on boundary electrode increase to ~95V, ions are extracted out of the auxiliary ICP into the main ICP, leading to a sharp increment in ion

current collected by Langmuir probe. In the meantime, high energy ions bombard the grid, causing secondary electrons emission form the grid, reducing the potential barrier near the grid [177]. As the boundary electrode bias decreases from 95 V, the energy of ions that are accelerated towards the main ICP decreases. However, ions can still overcome the potential barrier which is reduced by secondary electrons, resulting in a remaining large ion current collected by Langmuir probe until the boundary electrode bias decreases to ~40 V.

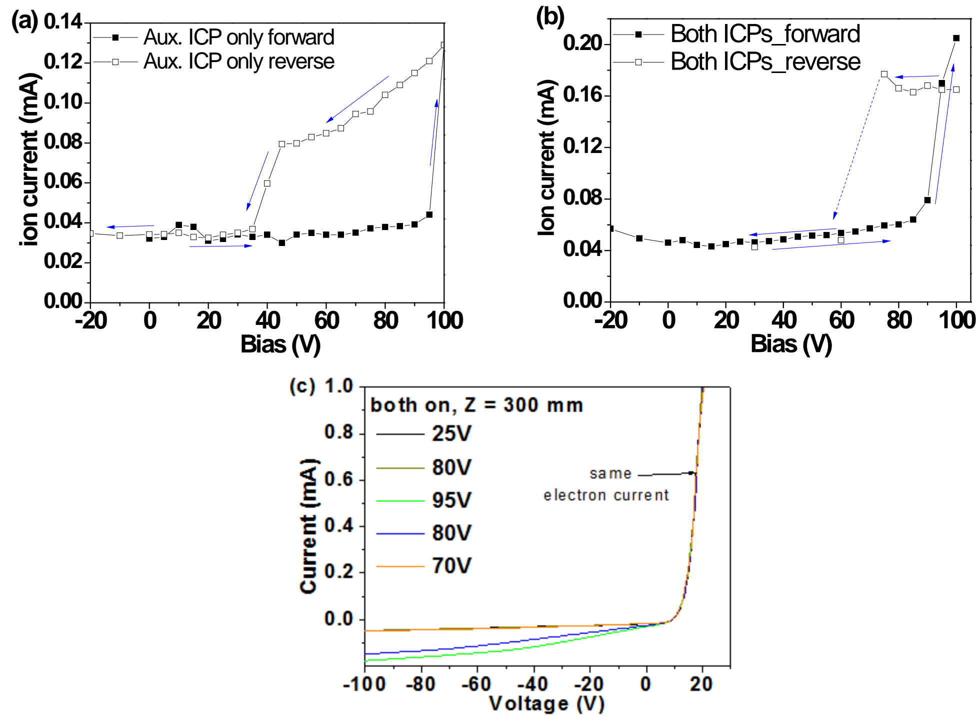

Figure 4.6 Ion saturation current as a function of boundary electrode bias for auxiliary ICP only and both ICPs on at the position of z=300 mm and I-V curve for both plasma on. (a): Upper ICP only. (b): Both ICPs on. (c): I-V curve for both plasmas on with different boundary electrode bias.

CHAPTER 5

EXTERNAL CONTROL OF THE ELECTRON ENERGY DISTRIBUTION USING DUAL TANDEM INDUCTIVELY COUPLED PLASMAS

In this chapter, an external control method to manipulate the EEPF in a pulsed, low pressure ICP plasma sustained in Ar at pressures of 15 mTorr is discussed. The reactor consists of two ICP sources in a tandem geometry separated by a grid. One of the ICPs is operated in a continuous wave mode while the other is operated in a pulsed plasma mode. Langmuir probe measurements were performed along the axis of the reactor in the main ICP, 11 cm below the grid. We found that during the afterglow of the pulsed plasma, the EEPF in the main ICP could be controlled by hot electron transport from the auxiliary ICP [170].

5.1 External control of electron temperature T_e and electron density n_e

Experimentally measured time-resolved electron temperature T_e and electron density n_e are shown in Figure 5.1(a) and Figure 5.1(b) for only the main (lower) ICP on and auxiliary ICP off; and with both ICPs on. The main ICP was turned ON to start the active-glow at time $t \approx 0$ μs and turned OFF (start of 80 μs of afterglow) at $t \approx 20$ μs. During the active-glow, T_e rapidly overshoots its steady state value and then reaches a quasi-steady state for the duration of the plasma-on period. The overshoot results from the need to avalanche the plasma density, and this phenomenon has been previously observed experimentally and predicted computationally [50, 178]. n_e increases by 3 to 4

times from the pre-pulse value, reaching 5.4 $\times 10^{11}$ cm^{-3} when only the main ICP is on and 4×10^{11} cm^{-3} when both ICPs are on. When only the main ICP is on, after the power is turned OFF (at $t \approx 20$ μs), T_e decreases, and within 20 μs reaches an almost constant value of 0.7 eV for the remainder of the afterglow. When the upper, auxiliary cw ICP is also on, after an initial decay to 1.0 eV, T_e increases to 1.7 eV at the end of the afterglow.

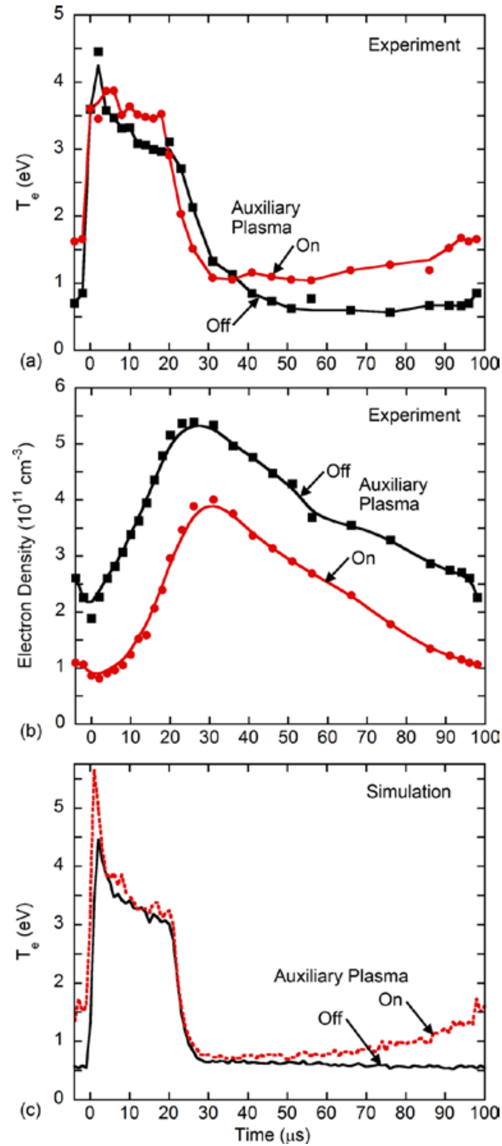

Figure 5.1 Time-resolved experimentally measured (a) electron temperature (T_e) and (b) electron density for the pulsed main ICP with and without the cw auxiliary ICP for argon at ≈15 mTorr. (c) Predictions of the electron temperature from the model.

5.2 External Control of EEPF

Experimentally measured and computed time-resolved EEPFs are shown in Figure 5.2 for only the main lower (pulsed) ICP being on. EEPFs are shown in Figure 5.3 for when the auxiliary upper (cw) ICP is also on. EEPFs are shown for t = 18 μs (≈2 μs before the end of the active glow), t = 23 μs (≈3μs into the afterglow), t = 51 μs (in the middle of the afterglow), and t = 94 μs (late in the afterglow).

The time-dependent behavior of T_e and the EEPF with only the main ICP on is well understood [32, 34, 179]. T_e increases when applying power, and overshoots the quasi-steady value as power is initially delivered to a smaller number of electrons. To avalanche the electron density to a higher value during the power pulse, T_e must at some point exceed the steady-state value. If the power pulse is long enough, T_e approaches the lower, quasi-steady value. The tail of the EEPF is extended to high energy and the electron distribution is fairly Maxwellian during the power on pulse. When the plasma power is turned OFF, inelastic collisions and diffusion cooling result in a fast decay of T_e, first in the tail of the EEPF, where inelastic collisions dominate, and later in the bulk. The EEPF microseconds after terminating power is a bi-Maxwellian with the temperature of the bulk relatively unchanged from the power on period due to its low rate of power loss, while the temperature of the tail rapidly decreases. After about 10 μs into the afterglow, T_e is too low for electrons to undergo significant inelastic collisions in argon. At this point, elastic thermalization collisions and diffusion cooling are the dominant cooling mechanisms. The EEPFs at this point appear Maxwellian as the plasma density is still high enough for electron-electron collisions to thermalize the distribution. On the timescale of the inter-pulse period, the asymptotic value of T_e = 0.7 eV is sustained by

superelastic heating by quenching of long-lived metastable excited states of argon. For example, from calculations of the electron energy distribution by solving Boltzmann's equation, for $T_e \approx 0.7$ eV, the thermalization (cooling) rate is about 25 eV/s. This cooling rate can be balanced by superelastic heating for an excited state density of 10^{10} cm^{-3}, which is commensurate with what is expected (and computed) for these conditions. The predictions for T_e from the simulations by Kushner et al. using the Hybrid Plasma Equipment Model (HPEM), shown in Figure 5.1(c), accurately capture the experimental trends.

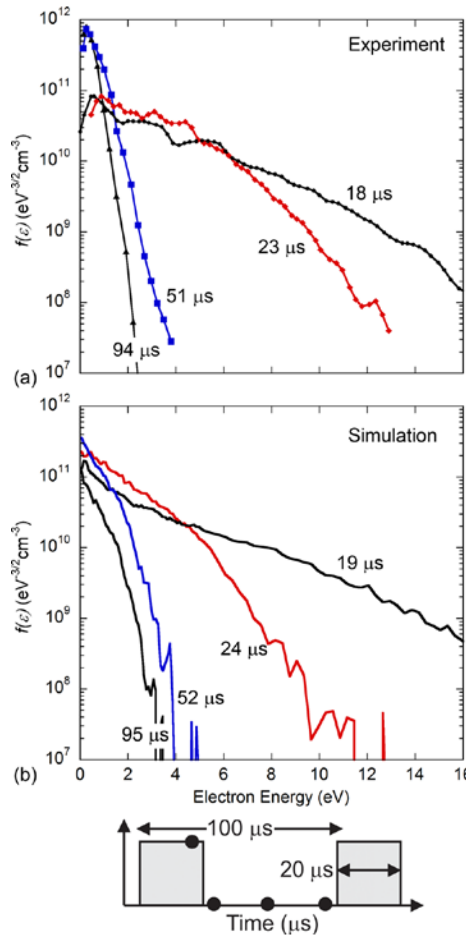

Figure 5.2 Time-resolved electron energy probability functions (EEPFs) when only the pulsed main ICP is on, obtained from the (a) experiment and (b) simulation. The times of the EEPFs relative to the start of the 20 μs power pulse are shown in the lower schematic.

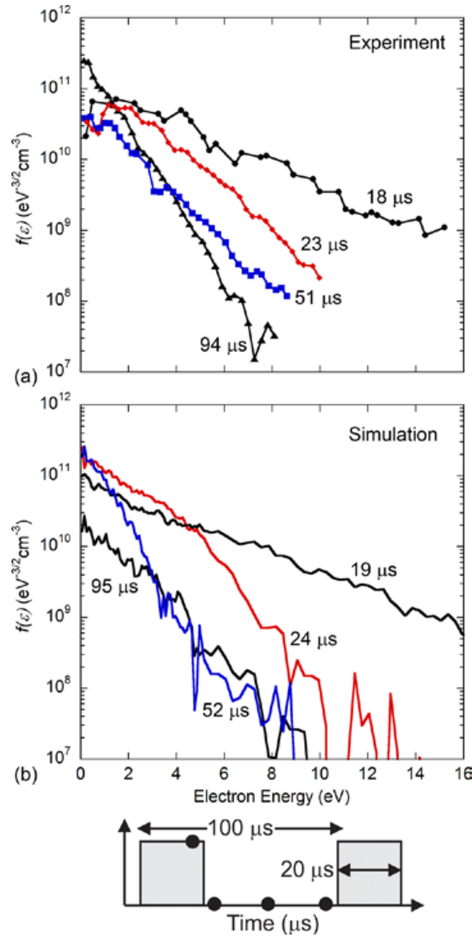

Figure 5.3 Time-resolved electron energy probability functions (EEPFs) when the pulsed main ICP and the auxiliary ICP are both on, obtained from the (a) experiments and (b) simulations. The times of the EEPFs relative to the start of the 20 μs power pulse are shown in the lower schematic.

When the auxiliary (upper) ICP is on there is the possibility to exchange electrons between the two plasma sources. Due to the confining plasma potential of each individual plasma source, the electrons which escape from one source and transport to the other source (auxiliary-to-main or main-to-auxiliary) are from the tail of the EEPF. Only the more energetic electrons are able to scale the plasma potential barrier at the boundary of one plasma source to transfer to the other plasma source. If the boundary regions on either side of the grid are not collisional, then the electron that loses energy scaling the potential hill from one source gains back energy being accelerated into the volume of the

adjacent source by its plasma potential. This flux of electrons originating from the adjacent plasma source is termed the *external heating flux*. The absolute value of the external flux is small since this flux originates in the tail of the EEPF.

The plasma potential near the axis (passing through the center of the open portion of the grid) as computed by the model is shown in Figure 5.4 for the auxiliary ICP being on and off. There is no active control of the plasma potential in either of the sources. Values are shown at the end of the active-glow power pulse and at the end of the afterglow. During the active-glow of the pulse, the plasma potential is predicted to be 3-4 V higher in the auxiliary ICP. This difference is likely larger in reality as the measured ($T_e \approx 3.5$ eV) in the main ICP is lower than that in the auxiliary ICP ($T_e \approx 4.5$ eV) by 1 eV. High energy electrons that overcome the potential barrier in the auxiliary ICP and, passing through the grid, are accelerated into the main ICP. Energetic electrons also overcome the potential barrier of the main ICP and are accelerated into the auxiliary ICP. The higher plasma potential of the auxiliary ICP compared to the main ICP, leads to a net loss of high energy electrons from the lower main ICP to the upper auxiliary ICP. (Note that the minimum in plasma potential between the grids presents a relatively low barrier compared to the plasma potential barrier in the absence of the adjacent plasma.) Although the absolute flux of these electrons is small, they are from the tail of the distribution function, which would otherwise be reflected by the plasma potential hill and return to produce ionization. The end result is a decrease in n_e in the main ICP when both ICPs are on, as shown in Figure 5.1, due to the lower potential barrier. Positive ions are injected from the auxiliary ICP to the main ICP. In the opposite direction, however, positive ions from the main ICP accelerate in the region below the grid, but cannot

overcome the larger potential barrier of the auxiliary ICP in the region above the grid.

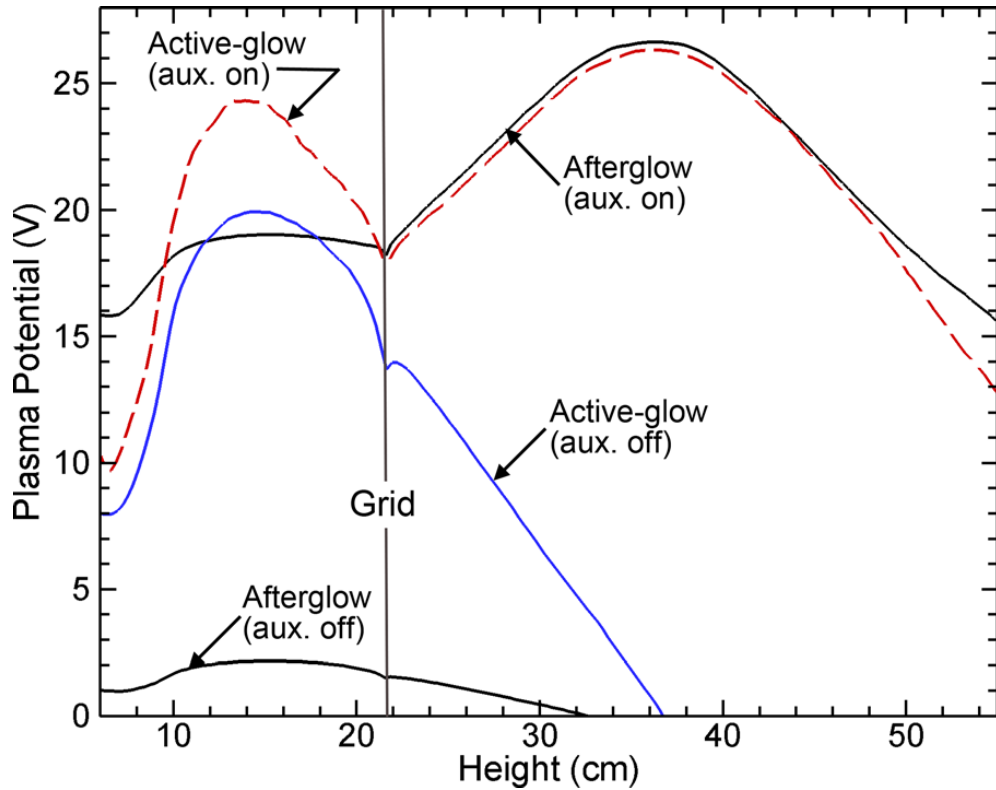

Figure 5.4 Plasma potentials along the axis passing through the central opening of the grid predicted by the model at the end of the active-glow and the end of the afterglow. Values are shown with and without the cw auxiliary ICP.

Since T_e of the auxiliary ICP is higher than that of the main ICP during the afterglow, there is a net injection of high energy electrons from the auxiliary ICP to the main ICP – the *external heating flux*. When both ICPs are on, the magnitude of the external heating flux entering the main ICP is small compared to the heating by its own inductively coupled electric fields. As a result, there is only a nominal effect on the shapes of the EEPFs. Experimentally and computationally, the shapes of the EEPFs in the main (lower) plasma source when its power is on depends little on whether the auxiliary (top) ICP source is on or off. However, during the afterglow of the pulsed main ICP when the far more dominating ICP heating source is off, superelastic collisions and the external

heating flux are the main source of electron heating. The magnitude of the external heating flux remains relatively constant while the electron density and superelastic heating source in the main plasma source decrease. By 60-70 μs (40-50 μs into the afterglow), the external heating flux produces a net increase in the T_e of the main ICP, reaching 1.7 eV at the end of the afterglow. The computed values of T_e, shown in Figure 5.1, also reflect the contributions of the external heating flux.

The consequences of the external heating flux from the auxiliary ICP on the main ICP during the afterglow are clearly evident in the EEPFs, shown in Figure 5.3, compared to the EEPFs without the auxiliary ICP, shown in Figure 5.2. Note that the displayed EEPFs result from collecting pseudo-particles in slices of 1/200th of the pulsed period averaged over a volume at the location of the probe of about 0.5 cm in radius and height. This time and spatial resolution introduces some noise. The EEPFs during the active-glow while the main plasma power is on have the same characteristic shape regardless of whether the auxiliary ICP is on or off. However, during the afterglow when the auxiliary plasma is on, the tails of the EEPFs of the main plasma are elevated, extending to energies of 8-10 eV. In the absence of the auxiliary plasma, the tails of the EEPFs late in the afterglow extend to only 2-4 eV. The computed EEFPs show these same trends.

CHAPTER 6

IGNITION DELAY OF A PULSED INDUCTIVELY COUPLED PLASMA (ICP) IN TANDEM WITH AN AUXILIARY ICP

As discussed above, Faraday shielded pulsed electronegative plasmas are very challenging to re-ignite, especially after a relatively long afterglow phase. The Faraday shield prevents capacitive coupling and the long afterglow results in low electron density due to dissociative attachment and diffusion to the walls. For example, the electron loss rate by dissociative attachment to Cl_2 plasma can be estimated by Equation 6.1[180]:

$$R_{att} = k_{att} n_e n_{Cl_2}, \tag{6.1}$$

where $k_{att}(m^3 s^{-1}) = 3.43 \times 10^{-15} Te^{-1.18} e^{-\frac{3.98}{Te}} + 3.05 \times 10^{-16} Te^{-1.33} e^{-\frac{0.11}{Te+0.014}}$

is the rate constant of dissociative attachment, n_e is electron density and n_{Cl_2} is Cl_2 density. The electron loss rate by diffusion to the wall Γ_e can be calculated from charge conservation at the walls: [116]

$$\Gamma_+ = \Gamma_e + \Gamma_-, \tag{6.2}$$

where Γ_+ is the flux of positive ions to the wall, Γ_- is the flux of negative ions to the wall. The flux of negative ions is essentially zero. Neglecting this term yields:

$$\Gamma_e = \Gamma_+ = \frac{h_{L,Cl^+} A_L + h_{R,Cl^+} A_R}{A_L + A_R} n_{Cl^+} u_{B,Cl^+} + \frac{h_{L,Cl_2^+} A_L + h_{R,Cl_2^+} A_R}{A_L + A_R} n_{Cl_2^+} u_{B,Cl_2^+}, \tag{6.3}$$

where n_{Cl^+} is density of Cl^+ ions and $n_{Cl_2^+}$ is density of Cl_2^+ ions. $A_L = \pi R^2$ and $A_R = 2\pi RL$ are the axial and radial wall surface areas, respectively. Wall loss factors $h_{L,j}$ and $h_{R,j}$ which represent the ratios of the density of positive ion j (Cl^+, Cl_2^+) at the axial and circumferential sheath to the averaged positive ion density in the bulk plasma were calculated by Lieberman et al. [1, 181, 182] as

$$h_{L,j} = \frac{n_{+sL,j}}{n_{+0,j}} \approx \frac{1+\frac{2\alpha_s}{\gamma_T}}{1+\alpha_s} 0.86 \left\{3.0 + \frac{L}{2\lambda_j} + \left(\frac{0.86 L u_{B,j}}{\pi \gamma_T D_j}\right)^2\right\}^{-1/2} \text{ and} \tag{6.4}$$

$$h_{R,j} = \frac{n_{+sR,j}}{n_{+0,j}} \approx \frac{1+\frac{3\alpha_s}{\gamma_T}}{1+\alpha_s} 0.80 \left\{4.0 + \frac{R}{\lambda_j} + \left(\frac{0.8 R u_{B,j}}{2.405 J_1(2.405) \gamma_T D_j}\right)^2\right\}^{-1/2}, \tag{6.5}$$

where $n_{+0,j}$ is volume averaged density of positive ion j (Cl^+, Cl_2^+) in the bulk plasma, and $n_{+sL,j}$ and $n_{+sR,j}$ are the densities of positive ion j at the axial and circumferential sheath edge, respectively. $u_{B,j} = \left[\frac{eT_e(1+\alpha_s)}{m_j(1+\alpha_s\gamma_T)}\right]^{1/2}$ is Bohm velocity of ion j, α_s is the electronegativity at the sheath edge, given by $\alpha_s = n_{Cl^-,s}/n_{e,s}$ where $n_{Cl^-,s}$ and $n_{e,s}$ are the negative ion and electron densities at the sheath edge, respectively. α_s is calculated by Ref. [1]:

$$\alpha_b = \alpha_s \exp\left[\frac{(1+\alpha_s)(\gamma_T - 1)}{2(1+\gamma_T\alpha_s)}\right], \tag{6.6}$$

where α_b is the bulk and $\gamma_T = T_e/T_i$ is the ratio of electron temperature to ion temperature.

As discussed by Liebermann et al., [116] in a typical pulsed Cl_2 plasma (10 kHz pulse frequency, 50% duty cycle, 5 mTorr, 400 W peak power), T_e decays to ~0.1 eV and

n_e decays to 1×10^{16}m^{-3} in 30 μs after the power is turned OFF ($\alpha_b \approx 12.0$, $\alpha_s \approx 7.82$ and $\gamma_T \approx 3.84$). The electrons loss rate by dissociative attachment is 1.0×10^{22} m^{-3}s^{-1}. The flux of electrons to the wall is 2.0×10^{19} m^{-2}s^{-1}. By multiplying the volume (0.005 m^3) and surface area (0.21 m^2) of the chamber (radius R = 0.15 m, length L = 0.075 m), the number of electrons lost per second by dissociative attachment and diffusion to the wall are estimated to be 5.0×10^{19} and 4.2×10^{18}, respectively. Obviously, the electron loss rate by dissociative attachment is much larger (~ 10 times) than the flux of electrons to the wall.

On the other hand, in a pulsed argon plasma, electrons are lost mainly by flux to the wall, which can be estimated by [1]

$$\Gamma_e = 0.61 n_e \left(\frac{eT_e}{M_{Ar}}\right)^{0.5}, \tag{6.7}$$

where M_{Ar} is the mass of argon atom. Take plasma parameters at t = 50 μs (30 μs into the afterglow) in Figure 5.1 as an example (T_e = 0.7 eV, $n_e = 4.0\times10^{17}$m^{-3}), the flux of electrons to the wall is calculated to be 3.17×10^{20} m^{-2}s^{-1}. By multiplying the surface area (0.06 m^2) of the chamber, the number of electrons lost to the wall is 1.9×10^{19}.

In our case, the flux of electrons to the wall and the electron loss rate by dissociative attachment are comparable. Figure 6.1 shows calculated electron loss rate by dissociative attachment and flux of electrons to the wall in Cl_2 plasmas in one pulse cycle with a pulse frequency of 1 kHz and duty cycle of 20 %. The auxiliary ICP power is at 500 W. The grid opening size is 230 μm. It is assumed that 50% of Cl_2 is dissociated at the pressure of 5 mTorr. The other parameters such as T_e, T_i, n_e and n_+ are from Langmuir probe measurement which will be discussed in Figure 6.5. At t = 230 μs, the

electrons loss rate by dissociative attachment is 3.8 $\times 10^{19}$ $m^{-3}s^{-1}$ and the flux of electrons to the wall is 1.5 $\times 10^{18}$ $m^{-2}s^{-1}$ ($\alpha_b \approx 1048$, $\gamma_T \approx 1.88, \alpha_s \approx 821$) The number of electrons lost per second by dissociative attachment and diffusion to the wall are estimated to be 3.9×10^{16} and 8.85×10^{16} by multiplying the volume (0.001 m^3) and surface area (0.06 m^2) of the chamber, respectively. Electrons are lost faster by diffusion to the wall than by dissociative attachment. This is different from normal pulsed electronegative plasma in which electrons loss rate by attachment is much faster than that by diffusion, as discussed above. That's due to the hot electron injected from auxiliary ICP, T_e does not drop to a very low value, leading to a large value of loss rate by diffusion. Also, pressure is quite low (5 mTorr), which yields a high T_e.

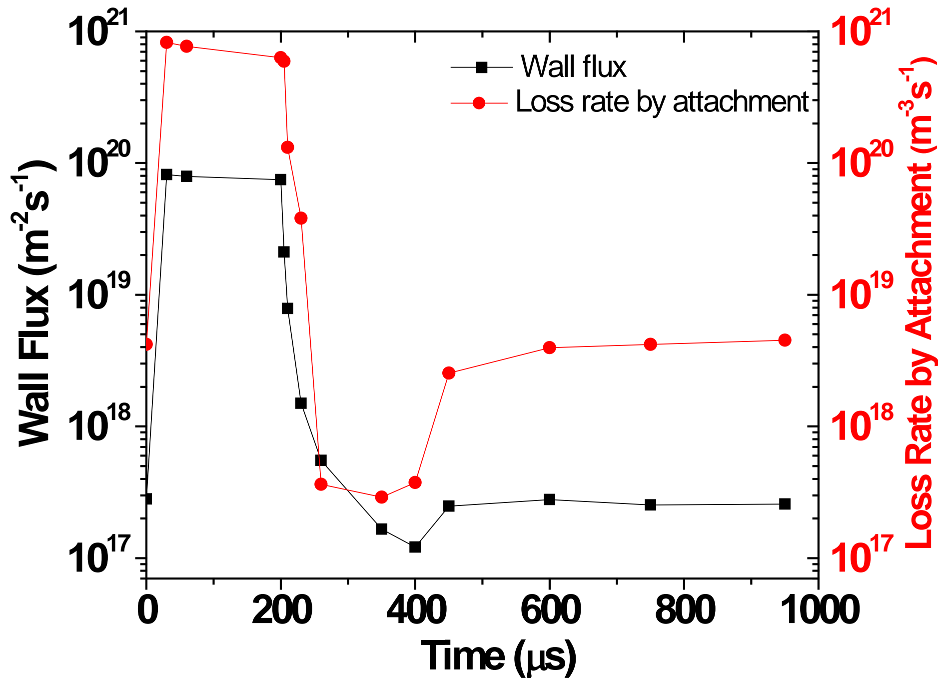

Figure 6.1 Estimated wall flux of electrons and electron loss rate by dissociative attachment as a function of time during a pulse. Base case conditions (Table 3.1), except duty cycle = 20%.

In this chapter, we explored the use of an auxiliary ICP operating in tandem with a main ICP to sustain pulsed electronegative plasma with long pulse period (1000 μs) in the presence of Faraday shield. Although the auxiliary source enabled the prompt ignition of pulsed Ar plasmas under all conditions, with electronegative plasmas, a delay in plasma ignition, referenced to the time when the main ICP power was turned ON, was observed in the main source, under certain operating conditions. Langmuir probe measurements provided the temporal evolution of electron temperature, and electron and positive ion densities and revealed the physics behind such ignition delay [183].

6.1 Ignition delay vs. duty cycle in chlorine plasmas

Plasma ignition and extinction as a function of time were monitored using the Cl λ = 837.5 nm line emission intensity. At the base case conditions (Table 3.1), the auxiliary ICP was powered continuously with 500 W and the main ICP was pulsed at 1 kHz (period = 1000 μs). For the chlorine plasma experiments, the two plasmas were separated by the tungsten grids with either 2.4 mm or 230 μm square holes (Grids A and B in Table 3.1). The pulsed RF waveform was delivered from the function generator to the amplifier at t = 0 μs. The voltage delivered to the coil had a 1/e rise (and fall) time of ~3 μs. Power remained on for a percent of the pulse period (duty cycle) that was varied from 20% to 99.9%. At 20% duty cycle, emission from Cl atoms appears within a few μs after the plasma is turned ON (i.e., no significant plasma ignition delay, see Figure 6.2). The emission intensity rises rather quickly at first, and continues to increase at a slower rate until the power is turned OFF at t=200 μs. At this time emission falls precipitously

on the time scale of the decay of T_e (several μs, see ref. [106]). Similar behavior was observed for duty cycles up to 60% (Figure 6.3).

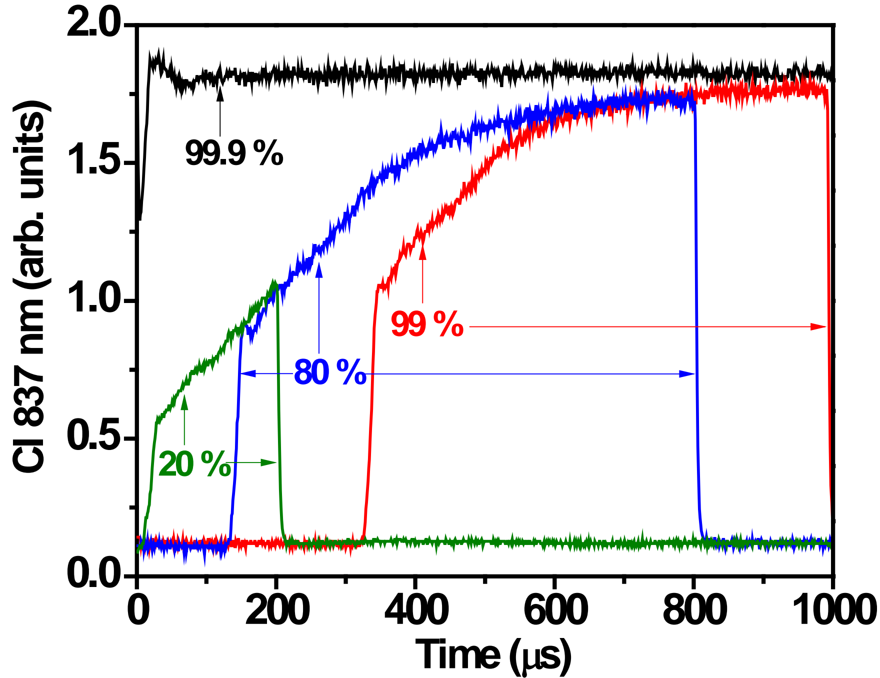

Figure 6.2 Optical emission intensity of the 837.5 nm line (Cl atoms) as a function of time during a pulse for different duty cycles. Other conditions were at their base case values (Table 3.1).

For duty cycles greater than 60%, however, a delay in plasma ignition was observed, i.e., the emission intensity was at the baseline level for the significant amount of time after the power was switched on at t = 0. After this induction period, a rapid rise in emission signified plasma re-ignition (Figure 6.2 for duty cycles of 80% and 99%). The ignition delay was found to increase almost linearly with duty cycle, for duty cycles larger than 70% (Figure 6.3). A maximum ignition delay of ~320 μs is observed for 99% duty cycle (plasma on/off time = 990/10 μs). Further increase in duty cycle to 99.5% (plasma on/off time = 995/5 μs) resulted in a nearly continuous plasma with no ignition

delay. Generally, the ignition delay was found to be nearly independent of pressure in the 2.5 ~ 20 mTorr range investigated (Figure 6.3).

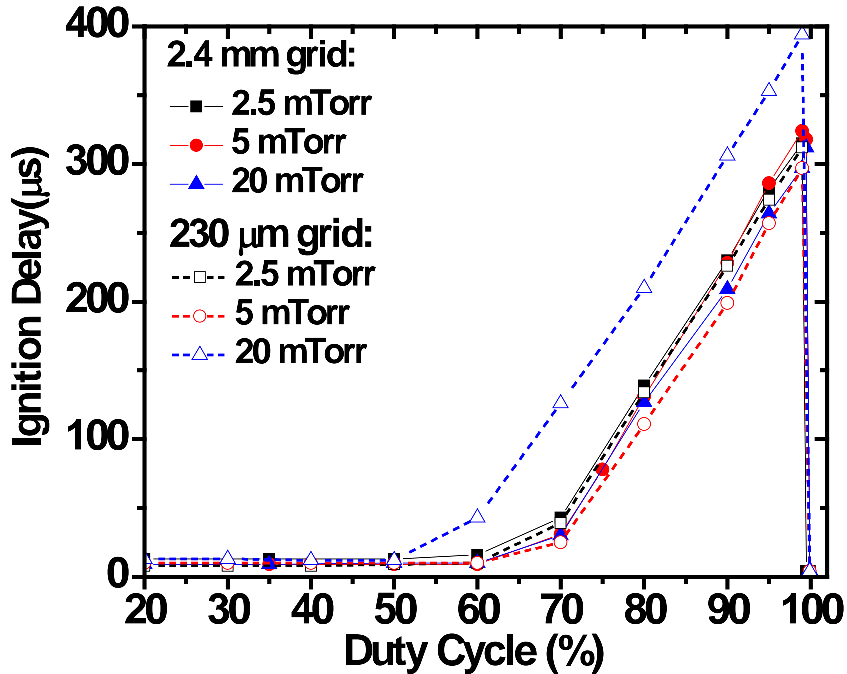

Figure 6.3 Plasma ignition delay vs. duty cycle, for three different pressures and two different grids. Other conditions were at their base case values (Table 3.1).

The increase in ignition delay with increasing duty cycle in chlorine ICPs is counter-intuitive. One would expect that, as the duty cycle increases, the shorter afterglow time (for constant pulse period) would cause the electron density at the end of the afterglow to be higher, making it easier to re-ignite the plasma, leading to a *shorter* delay time. For the same operating conditions, no ignition delays are observed in Ar plasmas, as shown by the time-resolved optical emission measurements of the Ar λ =750.4 nm line in Figure 6.4.

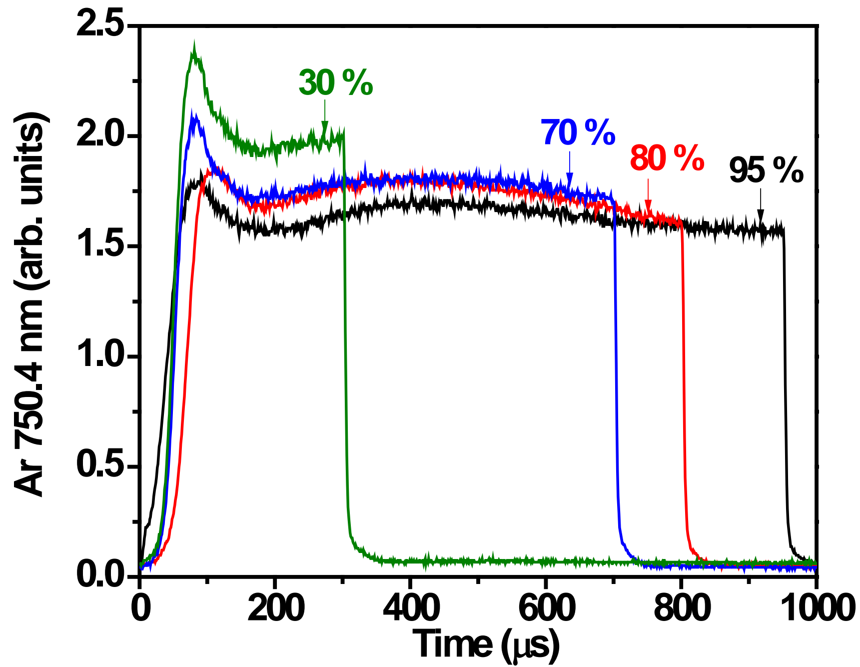

Figure 6.4 Optical emission intensity of the 750.4 nm line (Ar atoms) as a function of time during a pulse, for different duty cycles at otherwise base case conditions (Table 3.1).

Langmuir probe measurements were performed as a function of time for the same conditions and axial location used to collect optical emission. Figure 6.5 shows the electron density (n_e), positive ion density (n_+), positive ion temperature (T_+), negative ion temperature (T_-), and effective electron temperature (T_e) for a chlorine plasma, with peak main ICP power of 500 W, duty cycle of 20%, and auxiliary ICP cw power of 500 W. The dashed horizontal lines represent the electron density ($n_{e,aux}$), positive ion density ($n_{+,aux}$), and electron temperature ($T_{e,aux}$) in the main ICP, measured when *only* the auxiliary ICP is powered. For this low duty cycle, upon power turn-on of the main ICP at time t=0 μs, the electron density and electron temperature rise quickly (no ignition delay) and attain a quasi-steady value of ~ 10^{11} cm^{-3} and ~ 4 eV, respectively. At t = 200 μs,

when the main ICP power is switched off, electrons are quickly lost due to dissociative attachment to Cl_2 molecules and diffusion to the walls, as shown in Figure 6.1, causing n_e to decrease rapidly, falling below $n_{e,aux}$ at ~230 μs. T_e initially decays faster than the electron density (from its quasi steady-state value of ~4 eV to ~2 eV in about 10 μs after power is turned OFF) but, while the electron density keeps decreasing, T_e quickly turns around and reaches a relatively high value. The turnaround of T_e can be explained by the power injected into the main ICP from the auxiliary ICP. This power is distributed to a small number of electrons and the temperature heats up. This in turn causes ionization and the electron density starts increasing at t = 400 μs. The power injected from the auxiliary ICP is now distributed to a larger number of electrons, causing a decrease in the electron temperature. On the other hand, n_+ decays smoothly from the start of the afterglow and, at t~400 μs, n_+ reaches $n_{+,aux}$. When n_+ reaches $n_{+,aux}$, n_e increases sharply, before settling to its quasi-steady value of $n_{e,aux}$. At the same time T_e decreases tending to $T_{e,aux}$. It should be noted that late in a long afterglow of the main ICP, the plasma parameters are determined solely by the (cw powered) auxiliary ICP, injecting power into the main ICP.

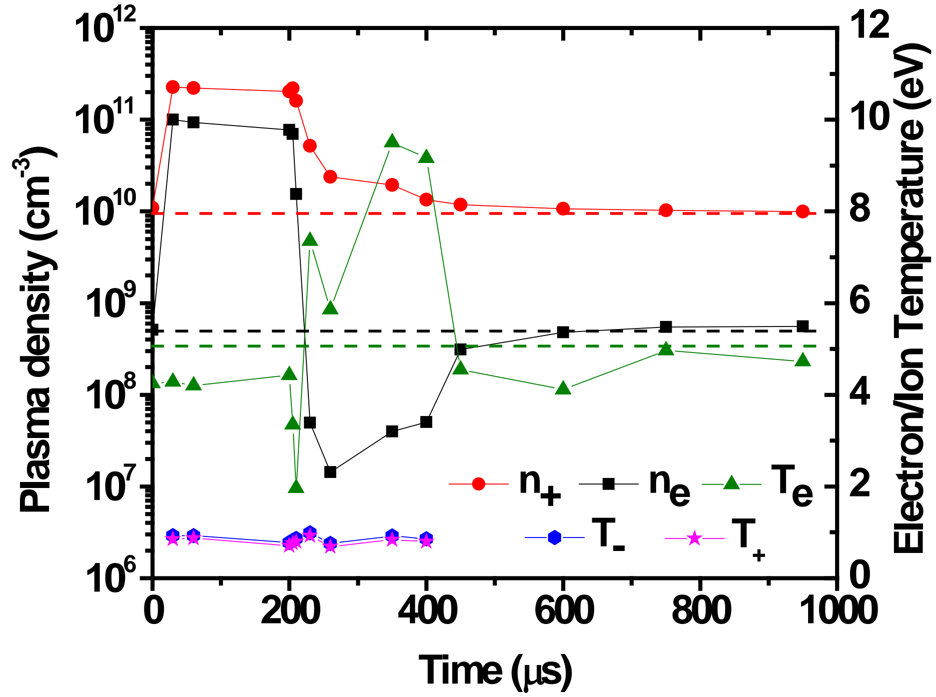

Figure 6.5 Plasma parameters as a function of time during a pulse cycle with a duty cycle of 20%. Dashed lines correspond to the positive ion density ($n_{+,aux}$), electron density ($n_{e,aux}$) and electron temperature ($T_{e,aux}$) when only the auxiliary ICP is on.

The plasma potential of the ion-ion plasma formed in the afterglow was measured to be ~ 20V for P_{aux} = 500W. Typically ion-ion plasmas have plasma potential close to zero due to: *i)* extremely low density of electrons and *ii)* positive and negative ions tend to have low similar energies. *iii)* plasma potential of ion-ion plasma is mainly determined by the ion temperature and not the electron temperature (as in conventional plasmas).

For a typical ion-ion plasma, plasma potential V_p , i.e., the potential of plasma with respect to the wall can be calculated by [1, 116, 184]

$$V_p = V_B + \Phi. \tag{6.8}$$

V_B is the Bohm criterion potential, i.e. the potential of the plasma with respect to the sheath edge, given by [184]

$$V_B = \frac{1}{2}\frac{1+\alpha_s}{1+\alpha_s\gamma_T}T_e. \tag{6.9}$$

Φ is the sheath potential, i.e., the potential of the sheath edge with respect to the wall, is calculated by the balance of electron flux Γ_e, negative ion flux Γ_- and positive ion flux Γ_+ at the sheath edge, $\Gamma_+ = \Gamma_e + \Gamma_-$ (Equation 6.2), given by

$$\Gamma_+ = \frac{h_{L,Cl^+}A_L + h_{R,Cl^+}A_R}{A_L+A_R}n_{Cl^+}u_{B,Cl^+} + \frac{h_{L,Cl_2^+}A_L + h_{R,Cl_2^+}A_R}{A_L+A_R}n_{Cl_2^+}u_{B,Cl_2^+}, \tag{6.8}$$

$$\Gamma_e = \frac{1}{4}\left(\frac{8eT_e}{\pi m_e}\right)^{\frac{1}{2}}\frac{1}{1+\alpha_s}\left(\frac{h_{L,Cl^+}A_L + h_{R,Cl^+}A_R}{A_L+A_R}n_{Cl^+} + \frac{h_{L,Cl_2^+}A_L + h_{R,Cl_2^+}A_R}{A_L+A_R}n_{Cl_2^+}\right)\exp\left(-\frac{\Phi}{T_e}\right), \text{ and} \tag{6.10}$$

$$\Gamma_- = \frac{1}{4}\left(\frac{8eT_i}{\pi m_{Cl^-}}\right)^{\frac{1}{2}}\frac{\alpha_s}{1+\alpha_s}\left(\frac{h_{L,Cl^+}A_L + h_{R,Cl^+}A_R}{A_L+A_R}n_{Cl^+} + \frac{h_{L,Cl_2^+}A_L + h_{R,Cl_2^+}A_R}{A_L+A_R}n_{Cl_2^+}\right)\exp\left(-\frac{\Phi}{T_i}\right). \tag{6.11}$$

For a typical ion-ion plasma which was discussed by Libermann er al. [116] (n_e = 1.0×10^{16}m^{-3}, n_{Cl^+} = 4.0×10^{16}m^{-3}, $n_{Cl_2^+}$ = 9.0×10^{16}m^{-3}, n_{Cl^-} = 1.2×10^{17}m^{-3}, $T^+ = T^- = 0.026$ eV, T_e = 0.1 eV, $\alpha_b \approx 12$, $\gamma_T \approx 3.84, \alpha_s \approx 7.82$), the Bohm criterion potential V_B is calculated to be 0.014 V, the sheath potential Φ is calculated to be 0.5 V. The plasma potential is calculated to be 0.514 V.

In our case, take plasma parameters at t = 230 μs in Figure 6.5 (Base case conditions (Table 3.1), except duty cycle = 20%.) as an example (n_e = 4.96×10^{13}m^{-3}, n_+ = 5.2×10^{16}m^{-3}, n_{Cl^-} = 5.2×10^{16}m^{-3}, $T_+ \approx 4.1$ eV, $T_- \approx 3.7$ eV, T_e = 7.35 eV, $\alpha_b \approx 1048$, $\gamma_T \approx 1.88, \alpha_s \approx 821$), the Bohm criterion potential V_B is calculated to be 1.95 V, the sheath potential Φ is calculated to be 0.35 V, The plasma potential with respect to the

wall is calculated to be 2.4 V. The higher Bohm criterion potential (1.95 V) in our case compared with that in normal ion-ion plasma (0.014 V) is due to higher T_e. In addition, the high measured plasma potential in the main ICP (~ 20 V) is due to the auxiliary plasma source operating continuously which may be thought of as a biased RF boundary electrode, shifting the plasma potential in the main ICP.

As seen in Figure 6.5, after t = 400 μs, plasma in the main ICP is mainly from the diffusion of auxiliary ICP. The "fitting technique" does not work well because the ion current of the I-V curve and the electronegativity is too low. We assume the ion temperatures remain constant at the value of t = 400 μs till end of afterglow. The other plasma parameters (n_e, n_+, T_e) after t = 400 μs are calculated from EEDF and Laframboise's orbital motion limited (OML) theory, as discussed in section 3.3.1.

It must be noted here that relatively high ion temperatures (up to 1 eV) were obtained by fitting the IV curves (see Figure 6.5). That is due to the high electric field near the probe tip. The Langmuir probe tip is about 2 cm away from a grounded stage (see Figure 3.1). With the measured plasma potential ~20V, the electric field near the probe tip is 10 V/cm. Under such high electric fields it is reasonable to expect high ion temperatures. The ion temperature in the presence of electric field can be calculated by [185-189]

$$k_B T_i = k_B T_g + \frac{m_i + m_g}{5m_i + 3m_g} m_g (\mu E)^2, \tag{6.12}$$

where m_i and m_g are mass of ions and neutral molecules, respectively. E is the electric field. μ is the ionic mobility, which is given by Economou et al. (Table 6.1). T_g is the gas temperature which is assumed to be 0.056 eV (650 K). T_+ and T_- are calculated to be 1.9

eV and 2.1 eV, respectively. These values are larger than measured ion temperature (~ 1eV). That's because Equation 6.12 does not take account of collisions of ions. In fact, the mean free path of ions λ_i is given by [184]

$$\frac{1}{\lambda_i} = \sum_j n_j \sigma_{ij}, \quad (6.13)$$

where n_j is the density of species j and σ_{ij} is the scattering cross section for the collision of the ion with species j which is given by Gudmundsson et al. (Table 6.2) [184] The mean free paths of Cl^+, Cl_2^+ and Cl^- calculated by Equation 6.13 are 1.06 cm, 0.74 cm and 1.06 cm, respectively. Ions will collide with other ions and neutrals and lose energies before they are collected by the Langmuir probe, resulting in a reduced T_i from Langmuir probe measurement.

Table 6.1 Ionic mobilities (N is the neutral gas density) [112].

Name	Symbol	Value
Cl_2^+ mobility	$N\mu_{Cl_2^+}$ $(cm^{-1}V^{-1}s^{-1})$	5.62×10^{19}
Cl^+ mobility	$N\mu_{Cl^+}$ $(cm^{-1}V^{-1}s^{-1})$	6.48×10^{19}
Cl^- mobility	$N\mu_{Cl^-}$ $(cm^{-1}V^{-1}s^{-1})$	6.48×10^{19}

Table 6.2 The scattering cross sections for collisions of various chlorine species (10^{-20} m^2) [184].

	Cl_2^+	Cl	Cl^+	Cl_2^+	Cl^-
Cl_2^+	100	75	150	200	150
Cl	75	50	100	150	100
Cl^+	150	100	50	75	50
Cl_2^+	200	150	75	100	75
Cl^-	150	100	50	75	50

Figure 6.6 shows n_e, n_+ and T_e for otherwise the same conditions as in Figure 6.5, but with a duty cycle of 80%. The electron density decays rapidly immediately after the main ICP power is turned-off at t=800 μs. In contrast to Figure 6.5 and consistent with Cl atomic emission intensity (Figure 6.1), the plasma continues to decay, even after the power is turned back on at t=0 μs, to start the next pulse cycle. Similar to the results in Figure 6.5, as soon as n_e decreases below $n_{e,aux}$, the rate of further n_e decay slows down. At t ~ 120 μs, when n_+ reaches $n_{+,aux}$, n_e increases rapidly, and the main ICP re-ignites at t=140 μs. The main difference between Figure 6.5 (no plasma ignition delay) and Figure 6.6 (plasma ignition delay), is that in Figure 6.6 the afterglow is not long enough for the decaying ion density to reach $n_{+,aux}$. Similar behavior was observed when the duty cycle was increased to 99% (Figure 6.7). Extinguishing power at t = 990 μs causes n_e to decay rapidly. This decay continues (even after power is re-initiated at t = 0) up to t ~320 μs, when n_+ reaches $n_{+,aux}$. At that time n_e increases sharply, and the plasma re-ignites. For a duty cycle of 99.7% (not shown), when power to the main ICP was turned ON, n_+ increased rapidly and reached a quasi-steady value of 2.5×10^{11} cm^{-3} while n_e reached a value of ~ 6 x 10^{10} cm^{-3}. During the ~3 μs afterglow (here the afterglow is not clearly defined due to the ramp up and ramp down of voltage on the coil), n_+ decreased to 1.5×10^{11} cm^{-3}, n_e decreased to 2×10^{10} cm^{-3}, and the plasma re-ignited without delay when the power was turned ON to start the next pulse cycle.

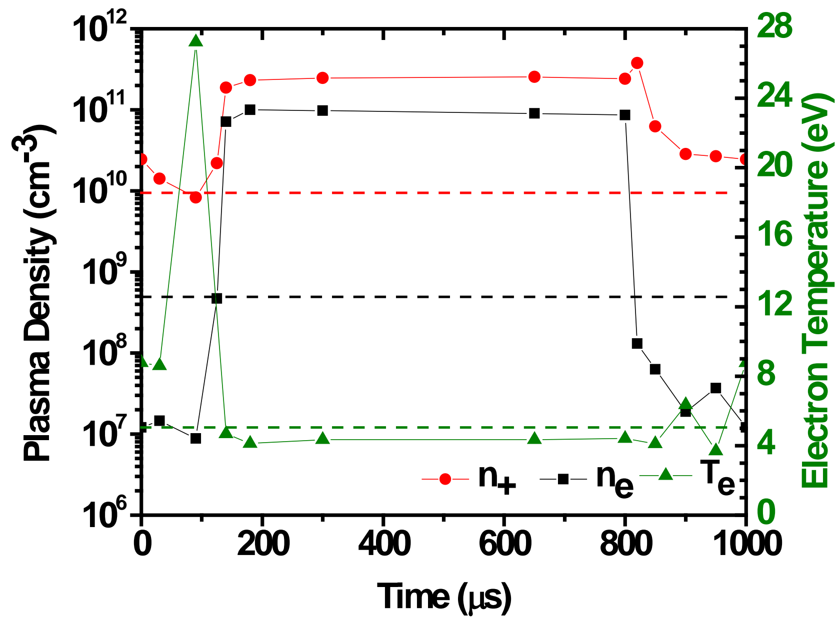

Figure 6.6 Plasma parameters as a function of time during a pulse cycle with a duty cycle of 80%. Dashed lines correspond to the positive ion density ($n_{+,aux}$), electron density ($n_{e,aux}$) and electron temperature ($T_{e,aux}$) when only the auxiliary ICP is on.

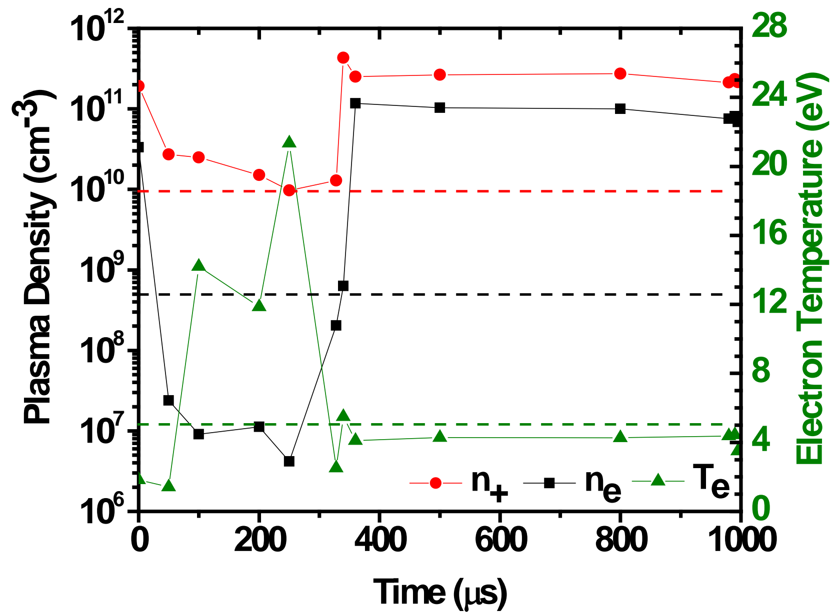

Figure 6.7 Plasma parameters as a function of time during a pulse cycle with a duty cycle of 99%. Dashed lines correspond to the positive ion density ($n_{+,aux}$), electron density ($n_{e,aux}$) and electron temperature ($T_{e,aux}$) when only the auxiliary ICP is on.

6.2 Ignition delay vs. main and auxiliary ICP power

Figure 6.8 shows the plasma density and electron temperature obtained in the main ICP with an auxiliary source power of 200 W. Other conditions were as in Figure 6.5. Immediately after the main ICP power is switched off at t=200 µs, n_e decays by three orders of magnitude in about 30 µs. Further decay of n_e is much slower compared to the case of 500 W auxiliary ICP power (Figure 6.5). At about t=700 µs (500 µs into the afterglow), n_e increases and attains a value close to $n_{e,aux}$. Meanwhile, n_+ decays until reaching $n_{+,aux}$. At this point the plasma re-ignites, as described above.

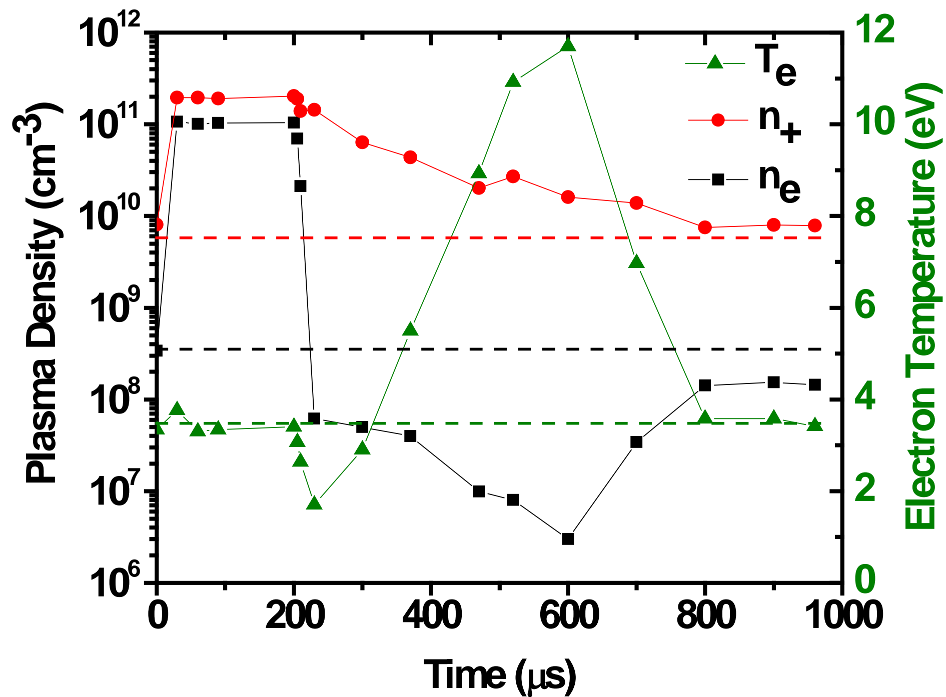

Figure 6.8 Plasma parameters as a function of time during a pulse cycle with a duty cycle of 20% and auxiliary ICP power of 200 W. Dashed lines correspond to the positive ion density ($n_{+,aux}$), electron density ($n_{e,aux}$) and electron temperature ($T_{e,aux}$) when only the auxiliary ICP is on.

The plasma ignition delay as a function of power to the auxiliary and main ICP is shown in Figure 6.9. The duty cycle of the main ICP (with a 1 kHz pulse frequency) was

kept constant at 99%, which gave the maximum ignition delay. For a peak power of 500 W delivered to the main ICP, the time delay decreases from 600 μs to 330 μs (for the 2.4 mm square grid), when the auxiliary ICP cw power is increased from 100 W to 500 W. With 500 W cw power delivered to the auxiliary ICP, the time delay increases from 210 μs to 300 μs when the time-average power to the pulsed main ICP increases from 250 W to 450 W.

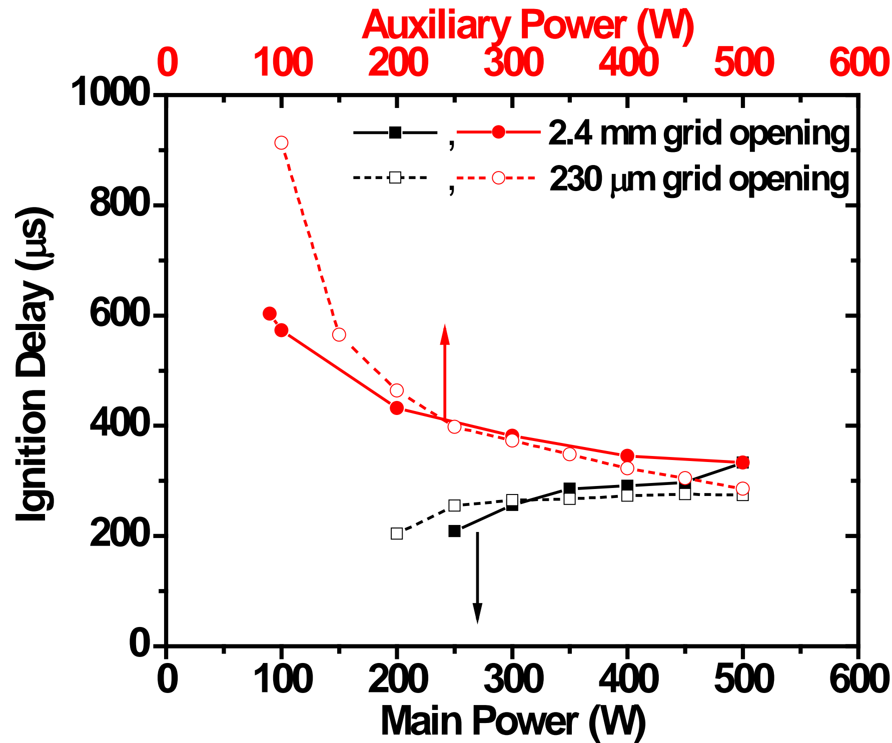

Figure 6.9 Black squares,: Ignition delay vs. time-average power of main ICP. Red circles,: Ignition delay vs. cw power of auxiliary ICP. Other conditions were at the base case values (Table 3.1). Solid and open symbols correspond to grid A and grid B, respectively.

6.3 Effect of grid hole size on ignition delay

The size of the openings of the grid separating the two plasmas can affect the plasma flux injected from the auxiliary to the main ICP. For a sheath thickness greater

that the opening size, the two plasmas will be more isolated from one another, while for a sheath thickness less than the opening size, plasma will spill through the openings, and the two plasmas will be in better "contact." The sheath thickness is assumed to be 10 times of Debye length λ_D, which is calculated by [190]

$$\frac{1}{\lambda_D} = \sqrt{\left(\frac{\alpha}{kT_n} + \frac{1-\alpha}{kT_e}\right)\frac{e^2 p}{\epsilon_0}}, \tag{6.14}$$

where $\alpha = n/p$ is the ratio of negative ion to positive ion density, and T_n, T_e are the negative ion and electron temperature, respectively. T_n and T_e were obtained from fitting the I-V curve measured by Langmuir probe, which is discussed on Appendix A. The sheath thickness calculated from Equation 6.9 ranges from 350-700 μm, for power in the 500W-100W range, at a pressure of 5 mTorr. To explore the effect of grid opening size on ignition delay, chlorine plasma experiments were conducted using tungsten grids A (2.4 mm square openings) and B (230 μm square openings), as described above. Figure 6.10 shows that the ignition delay as a function of duty cycle with 500 W auxiliary power is slightly longer for the grid with the smaller openings (grid B). The ignition delay increases linearly with duty cycle beyond a threshold value, which depends on the power applied to the auxiliary ICP.

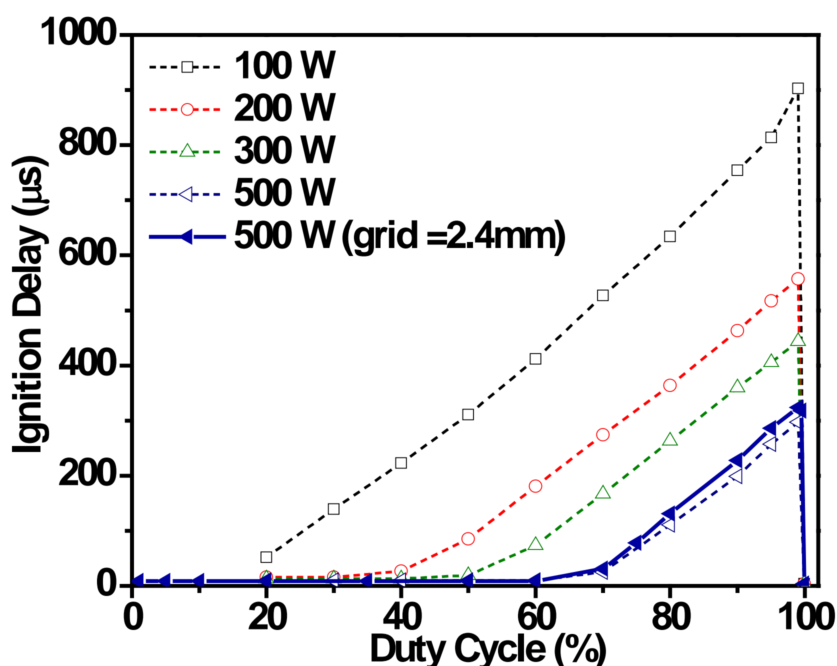

Figure 6.10 Plasma ignition delay vs. duty cycle, with different auxiliary ICP cw powers. Open symbols: grid B. Solid symbol: Grid A. Pressure, flow rates, and main ICP peak power were at base case values (Table 3.1).

Figure 6.3 shows ignition delays as a function of duty cycle at 3 pressures, for grids A and B. At 2.5 mTorr, there is little if any dependence on grid opening size. At 5 mTorr, slightly shorter delays are found for grid B. At 20 mTorr, grid B produces substantially longer delays compared to grid A. The difference in the delay times produced by the two grids at 20 mTorr is nearly constant (100 µs), for duty cycles ≥70%. Ignition delays as a function of power to the auxiliary and main ICP for grids A and B are compared in Figure 6.9. Relatively subtle differences are found with the exception of the lowest auxiliary power (100 W) for which grid B produces ~300 µs longer delays in plasma ignition. This may be a result of a thicker sheath (~700 µm) at low power,

increasing the isolation between the two plasmas and reducing the flux of electrons from the auxiliary into the main ICP.

6.4 Ignition delays in other electronegative gas plasmas

Plasma ignition delays, measured by optical emission, were also observed in other electronegative gases (SF_6, O_2, or 80%CF_4-20%O_2). Figure 6.11 shows the ignition delay as a function of duty cycle, for pulsed plasmas (1 kHz pulse frequency) in different electronegative gases. The main ICP peak power/auxiliary ICP cw power was: SF_6 (400W/110W or 400W/250W), O_2 (300W/100W), and 80% CF_4/20% O_2 (450W/110W). Similar to Cl_2 plasmas, ignition delays increase as a function of duty cycle above a threshold (with O_2 being a possible exception).

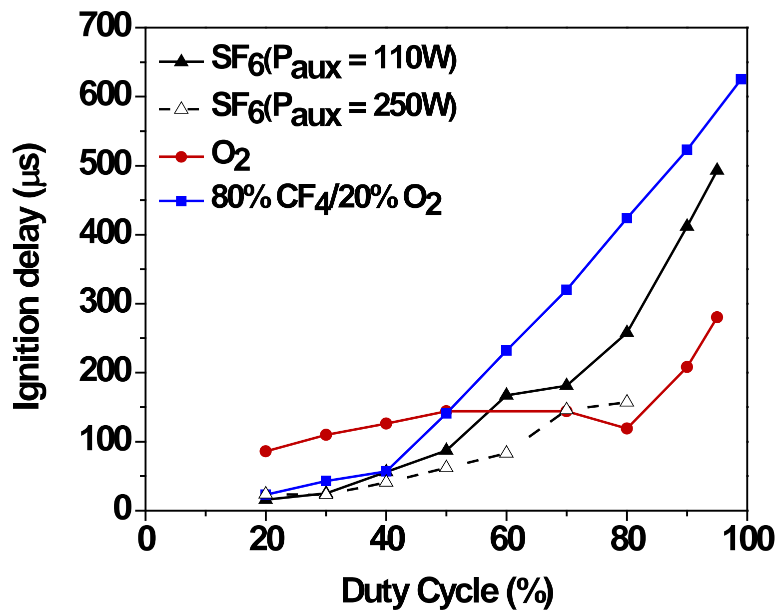

Figure 6.11 Plasma ignition delay vs. duty cycle in different electronegative gases. The main ICP was pulsed with a pulse repetition frequency of 1 kHz. Grid C was used and the pressure was 5 mTorr.

The ignition delay as a function of power to the auxiliary and main ICP in SF_6 is shown in Figure 6.12. Unfortunately, due to experimental constraints, it was not possible to operate at the duty cycle and power levels used for Cl_2 in Figure 6.9, so a direct comparison cannot be made. Nonetheless the trends are similar, in that at constant average power to the main ICP, the ignition delay decreases with increasing auxiliary ICP power, while the delay increases with increasing main ICP power. The increase in delay with main ICP power in SF_6, however, is much stronger than that in Cl_2.

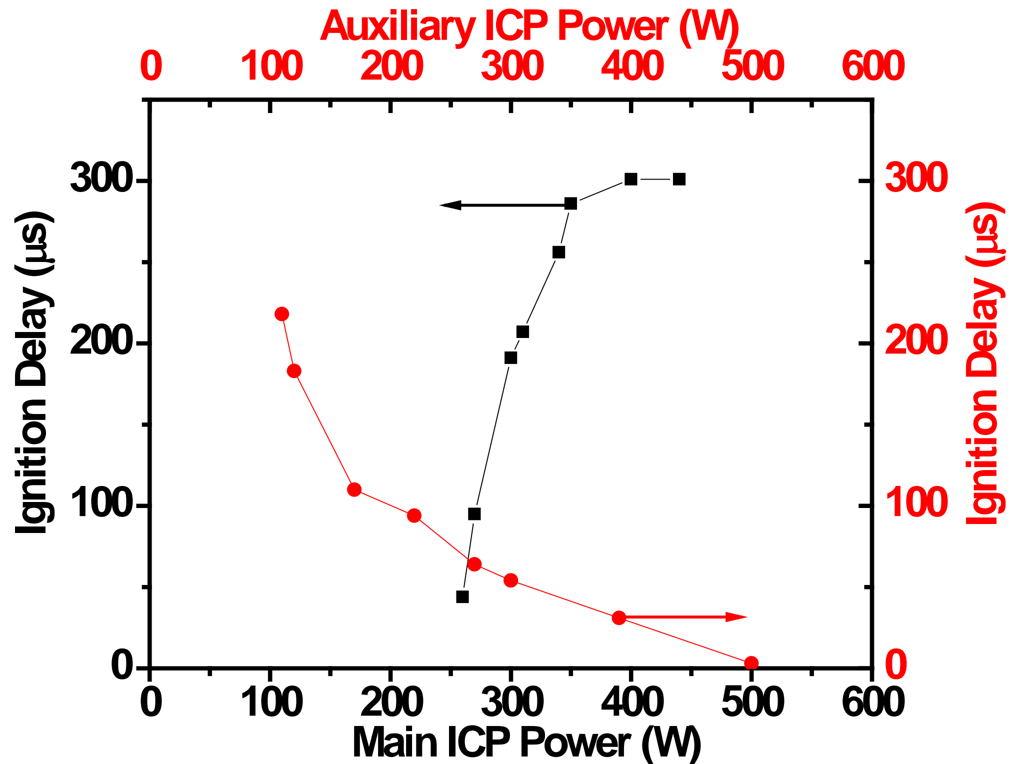

Figure 6.12 Black symbols, left axis: ignition delay vs. time-average power of main ICP in SF_6 plasmas. Red symbols, right axis: ignition delay vs. cw power of auxiliary ICP. For all data points, grid C was used, and the pressure was 5 mTorr.

The ignition delay was also found to decrease with increasing auxiliary ICP power in CF_4/O_2 plasmas (Figure 6.13) and O_2 plasmas (Figure 6.14). Contrary to Cl_2 and SF_6, however, the ignition delay *decreases* (slightly for CF_4/O_2 and drastically for O_2) with increasing average power delivered to the main ICP. If the plasma becomes less electronegative with increasing power, then the delay will be shortened (note again that Ar plasmas exhibit no ignition delay). On the other hand, if the electronegativity increases with power because a more attaching product is formed, then the ignition delay would be lengthened (see below). The relation between ignition delay and power delivered to main ICP in CF_4/O_2 plasmas and O_2 plasmas may be attributed the decreased plasma electronegativity to addition of oxygen due to the associative detachment of O^- with $O_2\,(^1\Delta_g)$ to form ozone [191] . Since the $O_2\,(^1\Delta_g)$ increases with power [192], the mechanisms mentioned above contribute substantially to the loss of O^- and O_2^- which decreases plasma electronegativity and hence the delay times decrease with increasing main ICP power.

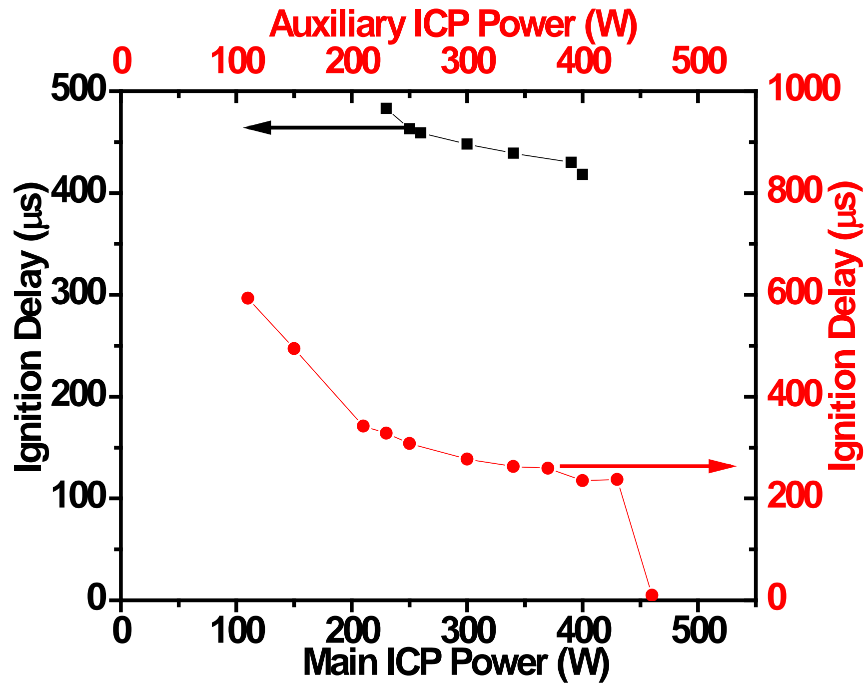

Figure 6.13 Black symbols, left axis: Ignition delay vs. time-average power of main ICP in 80%CF_4-20%O_2 plasmas. Red symbols, right axis: Ignition delay vs. cw power of auxiliary ICP. For all data points, grid C was used, and the pressure was 5 mTorr.

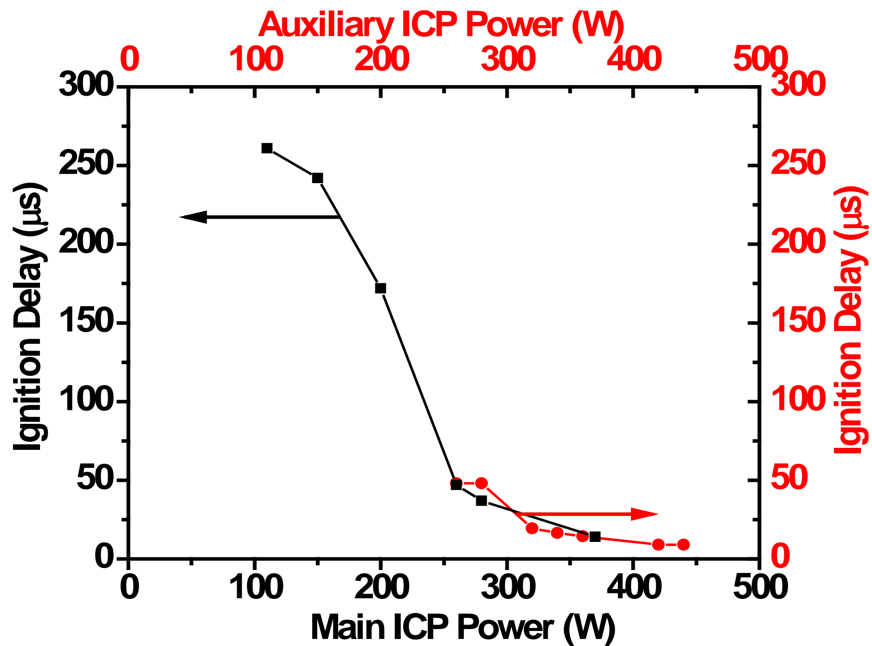

Figure 6.14 Black symbols, left axis: Ignition delay vs. time-average power of main ICP in O_2 plasmas. Red symbols, right axis: Ignition delay vs. cw power of auxiliary ICP. For all data points, grid C was used, and the pressure was 5 mTorr.

CHAPTER 7

CONCLUSIONS AND FUTURE WORK

7.1 Summary and Conclusions

The electron energy distribution function (EEDF) plays an essential role in non-equilibrium low- temperature plasmas. The EEDF governs most of the rate of electron-impact reactions and determines the plasma gas composition, which in turn determines the fluxes of radicals, ions, and photons striking the substrate. As such, control of the EEDF is of paramount importance for both fundamental plasma studies and practical applications.

A plasma reactor incorporating dual tandem inductively coupled plasma (ICP) sources (main and auxiliary source), separated by a grounded grid was used to manipulate the EEDF in the afterglow of the main pulsed plasma. By operating the auxiliary source on a cw basis, T_e during the afterglow of the main plasma source could be increased to a value (1.7 eV) above that of the afterglow plasma alone (0.7 eV) but below that of a continuous plasma (3.5 eV). Hot electron transport from the auxiliary plasma to the main plasma provided background heating that sustained the tail of the EEPF during the afterglow of the pulsed main ICP. As n_e decreased during the afterglow, a continuous influx of hot electrons produced an increase in T_e in the main plasma. This is a demonstration of *external control* of the EEPF. Simulations captured the experimentally measured trends in the EEPF and T_e, and demonstrated the importance of the *small external heating flux* in determining the properties of the main plasma.

While experimenting with the dual tandem ICP source, it was observed that, for a certain set of conditions, the plasma ignited with a time delay after the RF power to the main ICP was turned ON to start the next cycle. In pulsed chlorine plasmas, ignition delay appeared after a threshold value of the duty ratio (60% for the base case experimental conditions used) and, contrary to expectation, the ignition delay was longer with increasing duty cycle up to ~99.5% with no delay at a duty cycle of ~99.7%.

Langmuir probe diagnostics were employed to measure the time evolution of electron and positive ion densities as well as electron temperature. During the afterglow (main power off) of a pulsed chlorine plasma, it was observed that the electron density decayed rapidly. At the same time, the positive ion density decayed at a substantially slower rate. The time during the afterglow when the positive ion density (n_+) in the main ICP decayed to the value $n_{+,aux}$, obtained when *only* the auxiliary ICP was powered, was of critical importance. When n_+ reached $n_{+,aux}$, the electron loss rate was exceeded by the electron production rate due to gas ionization promoted by hot electron injection from the auxiliary plasma to the main ICP. Thus, n_e increased sharply, which also improved the inductive power coupling efficiency, igniting the plasma. If the afterglow was long enough for the decaying n_+ to reach $n_{+,aux}$ during the afterglow, then there was no plasma ignition delay. If the afterglow was too short for n_+ to reach $n_{+,aux}$ during the afterglow, then there was plasma ignition delay. These findings parallel the observations of Malyshev and Donnelly (ref.[60]**)**. The auxiliary ICP in the present experiment plays the role of an RF biased stage in M&D's separately powered ICP. The plasma ignition delay could be varied by changing the power of the auxiliary source and the main source. At higher auxiliary powers (i.e., higher $n_{+,aux}$), the ignition delay was found to be smaller

due to the shorter time required for n_+ to decay to $n_{+,aux}$. At higher main ICP powers (i.e., higher n_+), the ignition delay was found to increase due to the longer time required for n_+ to decay to $n_{+,aux}$.

Besides chlorine, ignition delays were also observed in other electronegative gases such as SF_6, 80% CF_4-20% O_2, and O_2. The ignition delay trends as a function of duty cycle, auxiliary and main power, were similar to those in chlorine. In 80% CF_4-20% O_2 and O_2 plasmas, however, the ignition delay was found to decrease with increasing main ICP power. This may be due to the role of $O_2\,(^1\Delta_g)$ in making the plasma less electronegative, by providing additional pathways (associative detachment of O^- and electron detachment from O_2^-) for negative ion loss which cause the ignition delay to decrease with increasing main ICP power. No ignition delays were observed in electropositive (e.g., argon) plasmas.

7.2 Recommendations for Future Work

7.2.1 New experimental dual tandem plasma reactor

In the current experimental setup, the aspect ratio (height/radius) of both main and auxiliary ICP is too large. In each ICP, plasma is generated around the middle of the coil. The relatively small cross sectional area of contact and the large separation between the two plasmas do not allow efficient interaction of the two ICP sources. In the proposed new experimental setup, the two ICP sources are identical with small aspect ratio, as shown in Figure 7.1. In this configuration, the two plasmas will have much more efficient

interaction. Also, using two identical ICP sources will make it easier to understand how the two plasmas interact with each other. A new experiment is to pulse both ICPs synchronously, and vary the phase difference between the two plasmas. That way plasma can be injected from the upper to the lower source when the upper ICP is in the activeglow phase of the pulse and the lower ICP is in the afterglow phase of the pulse (or vice versa). On the other hand, for electronegative plasmas, enhanced injection flux of electrons from the auxiliary cw ICP to the main pulsed ICP is expected to increase the production rate of electrons at the beginning of the active glow of the main ICP, reducing or even eliminating plasma ignition delay.

7.2.2 Langmuir probe measurements in the auxiliary ICP

So far, all Langmuir probe (LP) measurements have been taken in the main ICP. We propose to install Langmuir probe in the auxiliary ICP to measure the plasma parameters of that source as well. By measuring the plasma parameters at mirror image positions in both main and auxiliary ICPs, the direction of plasma transport between the two sources can be obtained. Also, we can measure the plasma potential profile in the auxiliary ICP. The profile of Figure 5.4 is expected to be obtained.

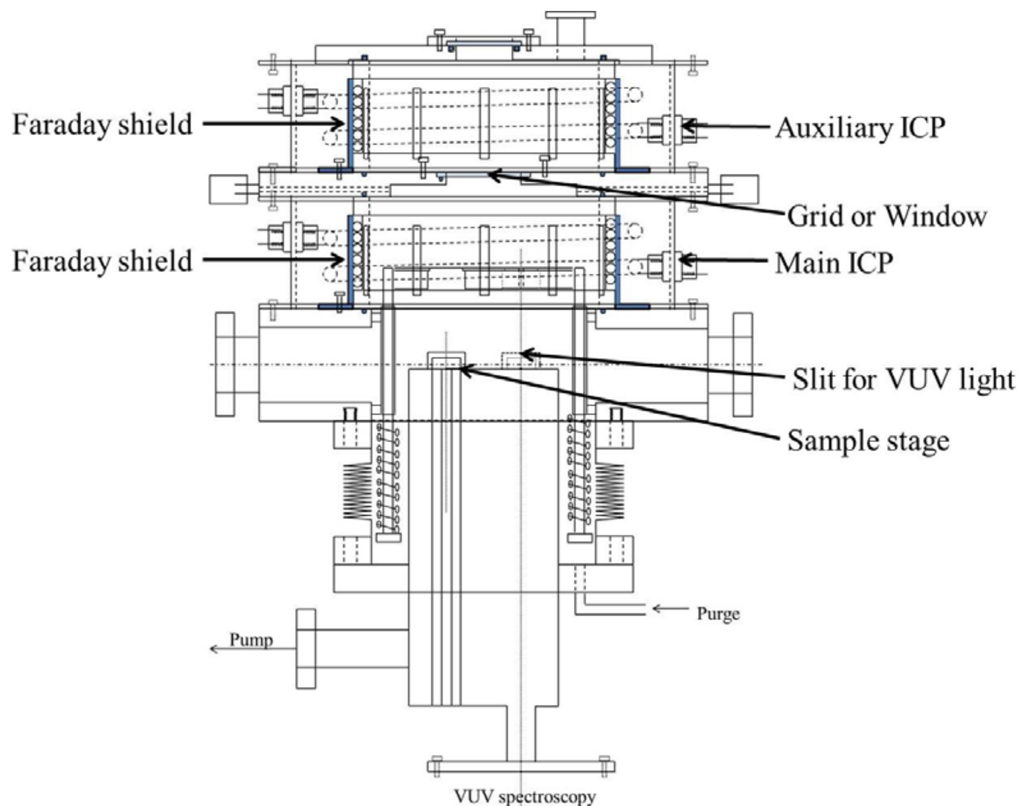

Figure 7.1 Schematic of the new experimental apparatus.

7.2.3 Dual biasable grids

By installing two parallel grids between the auxiliary and the main ICP, we should be able to obtain better separation of the two plasmas. Subsequently, we can control the species that can diffuse into the main plasma by biasing the grids. For instance, by applying appropriate potentials on the grids we can block charged species and allow only photons and neutrals to enter the main ICP. By varying the applied bias, we can also control the plasma potential close to the grids and therefore control the transport of charges between the two plasmas.

References

[1] M. A. Lieberman and A. J. Lichtenberg, *Principles of Plasma Discharges and Materials Processing* (New Jersey: Wiley, 2005).

[2] J. D. Plummer, M. D. Deal and P. D. Griffin, *Silicon VLSI Technology: Fundamentals, Practice and Modeling*, *First editon.* (Prentice Hall, Upper Saddle River, New Jersey, 2000).

[3] D. J. Economou, "*The Chemistry of Plasma Etching*," *in The Chemistry of Electronic Materials,* ed H. B. Pogge, (Marcel Dekker, Inc., New York), pp 251 (1996).

[4] F. F. Chen, *Introduction to Plasma Physics and Controlled Fusion, Vol. 1:* "*Plasma Physics*," *Second edition.* (Plenum Press, New York, 1984).

[5] W. Crookes, "On radiant matter," *Journal of the Franklin Institute*, **108**, 305 (1879).

[6] J. J. Thomson, "Cathode rays," *Philosophical Magazine*, **44**, 293 (1897).

[7] I. Langmuir, "Oscillations in ionized gases," *Proc. Natl. Acad. Sci. U.S.A.* , **14**, 627 (1928).

[8] H. M. Mott-Smith, "History of plasmas," *Nature*, **233**, 219 (1971).

[9] R. G. Poulsen, "Plasma etching in integrated circuit manufacture—A review," *J. Vac. Sci. Technol A*, **14**, 266 (1977).

[10] B. E. E. Kastenmeier, P. J. Matsuo, J. J. Beulens and G. S. Oehrlein, "Chemical dry etching of silicon nitride and silicon dioxide using $CF_4/O_2/N_2$ gas mixtures," *J. Vac. Sci. Technol A*, **14**, 2802 (1996).

[11] S. M. Irving, "Plasma oxidation process for removing photoresist films," *Solid State Technology*, **14**, 47 (1971).

[12] T. C. Penn, "Forecast of VLSI processing—A historical review of the first dry processed IC," *IEEE Transactions on Electron Devices*, **26**, 640 (1979).

[13] International Technology Roadmap for Semiconductors: 2015 update review.

[14] G. N. L. Chris, J. K. Keren and A. G. Richard, "The grand challenges of plasma etching: a manufacturing perspective," *J. Phys. D: Appl. Phys.*, **47**, 273001 (2014).

[15] T. Makabe and Z. L. Petrovic, *Plasma Electronics: Applications in Microelectronic Device Fabrication*, *Second edition* (CRC Press, 2014).

[16] V. M. Donnelly and A. Kornblit, "Plasma etching: Yesterday, today, and tomorrow," *J. Vac. Sci. Technol A*, **31**, 050825 (2013).

[17] H. Sugai, I. Ghanashev, M. Hosokawa, K. Mizuno, K. Nakamura, H. Toyoda and K. Yamauchi, "Electron energy distribution functions and the influence on fluorocarbon plasma chemistry," *Plasma Sources Sci. Technol.*, **10**, 378 (2001).

[18] S. B. Wang and A. E. Wendt, "Ion bombardment energy and SiO_2/Si fluorocarbon plasma etch selectivity," *J. Vac. Sci. Technol. A*, **19**, 2425 (2001).

[19] S. B. Wang and A. E. Wendt, "Control of ion energy distribution at substrates during plasma processing," *J. Appl. Phys.*, **88**, 643 (2000).

[20] X. V. Qin, Y. H. Ting, A. E. Wendt, "Tailored ion energy distributions at an rf biased plasma electrode," *Plasma Sources Sci. Technol.*, **19** 065014 (2010).

[21] A. Agarwal and M. J. Kushner, "Effect of nonsinusoidal bias waveforms on ion energy distributions and fluorocarbon plasma etch selectivity," *J. Vac. Sci. Technol. A*, **23**, 1440 (2005).

[22] K. J. Kanarik, T. Lill, E. A. Hudson, S. Sriraman, S. Tan, J. Marks, V. Vahedi and R. A. Gottscho, "Overview of atomic layer etching in the semiconductor industry," *J. Vac. Sci. Technol A*, **33**, 020802 (2015).

[23] L. Xu, D. J. Economou, V. M. Donnelly and P. Ruchhoeft, "Extraction of a nearly monoenergetic ion beam using a pulsed plasma," *Appl. Phys. Lett.*, **87**, 041502 (2005).

[24] H. Shin, W. Zhu, L. Xu, V. M. Donnelly and D. J. Economou, "Control of ion energy distributions using a pulsed plasma with synchronous bias on a boundary electrode," *Plasma Sources Sci. Technol.*, **20**, 055001 (2011).

[25] S. Samukawa and S. Furuoya, "Time modulated electron cyclotron resonance plasma discharge for controlling generation of reactive species," *Appl. Phys. Lett.*, **63**, 2044 (1993).

[26] S. Samukawa and K. Terada, "Pulse time modulated electron cyclotron resonance plasma etching for highly selective, highly anisotropic, and less charging polycrystalline silicon patterning," *J. Vac. Sci. Technol. B*, **12**, 3300 (1994).

[27] W. Jin, S. A. Vitale and H. H. Sawin, "Plasma surface kinetics and simulation of feature profile evolution in Cl_2 + HBr etching of polysilicon," *J. Vac. Sci. Technol A*, **20**, 2106 (2002).

[28] S. Samukawa and T. Tsukada, "Effects of electron temperature in high density Cl_2 plasma for precise etching processes," *Appl. Phys. Lett.*, **68**, 1056 (1996).

[29] J. P. Chang and H. H. Sawin, "Kinetic study of low energy ion enhanced polysilicon etching using Cl, Cl_2, and Cl^+ beam scattering," *J. Vac. Sci. Technol A*, **15**, 610 (1997).

[30] M. Balooch, M. Moalem, W. E. Wang and A. V. Hamza, "Low energy Ar ion induced and chlorine ion etching of silicon," *J. Vac. Sci. Technol A*, **14**, 229 (1996).

[31] S. A. Vitale, H. Chae and H. H. Sawin, "Silicon etching yields in F_2,Cl_2,Br_2, and HBr high density plasmas," *J. Vac. Sci. Technol A*, **19**, 2197 (2001).

[32] M. V. Malyshev, V. M. Donnelly, J. I. Colonell and S. Samukawa, "Dynamics of pulsed power chlorine plasmas," *J. Appl. Phys.*, **86**, 4813 (1999).

[33] S. Samukawa, K. Noguchi, J. I. Colonell, K. H. A. Bogart, M. V. Malyshev and V. M. Donnelly, “Reduction of plasma induced damage in an inductively coupled plasma using pulsed source power,” *J. Vac. Sci. Technol. B*, **18**, 834 (2000).

[34] M. V. Malyshev and V. M. Donnelly, “Dynamics of inductively coupled pulsed chlorine plasmas in the presence of continuous substrate bias,” *Plasma Sources Sci. Technol.*, **9**, 353 (2000).

[35] P. Subramonium and M. J. Kushner, “Two dimensional modeling of long term transients in inductively coupled plasmas using moderate computational parallelism. I. Ar pulsed plasmas,” *J. Vac. Sci. Technol. A*, **20**, 313 (2002).

[36] D. L. Flamm, “Mechanisms of silicon etching in fluorine- and chlorine-containing plasmas,” *Pure Appl. Chem.*, **62**, 1709 (1990).

[37] D. J. Economou, “Fundamentals and applications of ion-ion plasmas,” *Appl. Surf. Sci.*, **253**, 6672 (2007).

[38] J. E. Demetre, “Pulsed plasma etching for semiconductor manufacturing,” *J. Phys. D: Appl. Phys.*, **47**, 303001 (2014).

[39] S. Banna, A. Agarwal, G. Cunge, M. Darnon, E. Pargon and O. Joubert, “Pulsed high density plasmas for advanced dry etching processes,” *J. Vac. Sci. Technol A*, **30**, 040801 (2012).

[40] C. J. Mogab, A. C. Adams and D. L. Flamm, “Plasma etching of Si and SiO_2—The effect of oxygen additions to CF_4 plasmas,” *J. Appl. Phys.*, **49**, 3796 (1978).

[41] J. Hopwood, “Review of inductively coupled plasmas for plasma processing,” *Plasma Sources Sci. Technol.*, **1**, 109 (1992).

[42] S. K. Nam, D. J. Economou and V. M. Donnelly, “Particle-in-cell simulation of ion beam extraction from a pulsed plasma through a grid,” *Plasma Sources Sci. Technol.*, **16**, 90 (2007).

[43] J. L. Mauer, J. S. Logan, L. B. Zielinski, and G. C. Schwartz, “Mechanism of silicon etching by a CF_4 plasma,” *J. Vac. Sci. Technol.*, **15**, 1734 (1978).

[44] H. Shin, W. Y. Zhu, L. Xu, V. M. Donnelly and D. J. Economou, “Control of ion energy distributions using a pulsed plasma with synchronous bias on a boundary electrode,” *Plasma Sources Sci. Technol.*, **20**, (2011).

[45] J. W. Coburn, H. F. Winters and T. J. Chuang, “Ion-surface interactions in plasma etching,” *J. Appl. Phys.*, **48**, 3532 (1977).

[46] D. L. Flamm and V. M. Donnelly “The design of plasma etchants,” *Plasma. Chern. Plasma Process.*, **1**, 317 (1981).

[47] H. F. Winters, J. W. Coburn and T. J. Chuang, “Surface processes in plasma assisted etching environments,” *J. Vac. Sci. Technol. B*, **1**, 469 (1983).

[48] H. Akashi, S. Samukawa, N. Takahashi and T. Sasaki, “Dependence of frequency and pressure on electron energy distribution functions in low pressure plasma,” *Japanese J. Appl. Phys.*, **36**, L877 (1997).

[49] M. E. Barone and D. B. Graves, "Chemical and physical sputtering of fluorinated silicon," *J. Appl. Phys.*, **77**, 1263 (1995).

[50] G. A. Hebner and C. B. Fleddermann, "Characterization of pulse modulated inductively coupled plasmas in argon and chlorine," *J. Appl. Phys.*, **82**, 2814 (1997).

[51] J. P. Chang, J. C. Arnold, G. C. H. Zau, H. S. Shin and H. H. Sawin, "Kinetic study of low energy argon ion enhanced plasma etching of polysilicon with atomic/molecular chlorine," *J. Vac. Sci. Technol. A*, **15**, (1997).

[52] V. Godyak, "Ferromagnetic enhanced inductive plasma sources," *J. Phys. D: Appl. Phys.*, **46**, 283001 (2013).

[53] S. Seiji, M. D. Vincent and V. M. Mikhail "Effects of discharge frequency in plasma etching and ultrahigh frequency plasma source for high performance etching for ultralarge scale integrated circuits," *Japanese J. Appl. Phys.*, **39**, 1583 (2000).

[54] S. Samukawa and H. Akashi, "Effects of discharge frequency on plasma characteristics and etching characteristics in high density Cl_2 plasma: comparison of ultrahigh frequency plasma and radio frequency plasma," *IEEE Transactions on Plasma Science*, **26**, 1621 (1998).

[55] S. Seiji and T. Tsutomu, "Dependence of electron energy distributions on discharge pressure in ultrahigh-frequency and inductive-coupled Cl_2 plasmas," *Japanese J. Appl. Phys.*, **36**, 7646 (1997).

[56] M. V. Malyshev, V. M. Donnelly and S. Samukawa, "Ultrahigh frequency versus inductively coupled chlorine plasmas: Comparisons of Cl and Cl_2," *J. Appl. Phys.*, **84**, 1222 (1998).

[57] V. A. Godyak and R. B. Piejak, "Abnormally low electron energy and heating-mode transition in a low-pressure argon rf discharge at 13.56 MHz," *Physical Review Letters*, **65**, 996 (1990).

[58] S. H. Song, M. J. Kushner, "Control of electron energy distributions and plasma characteristics of dual frequency, pulsed capacitively coupled plasmas sustained in Ar and $Ar/CF_4/O_2$," *Plasma Sources Sci. Technol.*, **21**, 055028 (2012).

[59] P. Diomede, D. J. Economou and V. M. Donnelly, "Particle-in-cell simulation of ion energy distributions on an electrode by applying tailored bias waveforms in the afterglow of a pulsed plasma," *J. Appl. Phys.*, **109**, 083302 (2011).

[60] M. V. Malyshev and V. M. Donnelly, "Dynamics of inductively-coupled pulsed chlorine plasmas in the presence of continuous substrate bias," *Plasma Sources Sci. Technol.*, **9**, 353 (2000).

[61] X. Huang, W. C. Lee, C. Kuo, D. Hisamoto, L. Chang, J. Kedzierski, E. Anderson, H. Takeuchi, Y. K. Choi, K. Asano, V. Subramanian, T. J. King, J. Bokor and C. Hu, "Sub-50 nm P-Channel FinFET," *IEEE Trans. Electron Devices*, **48**, 880 (2001).

[62] J. I. Hong, S. H. Seo, S. S. Kim, N. S. Yoon, C. S. Chang and H. Y. Chang, "Electron temperature control with grid bias in inductively coupled argon plasma," *Phys. Plasmas*, **6**, 1017 (1999).

[63] V. A. Godyak, R. B. Piejak and B. M. Alexandrovich, "Measurement of electron energy distribution in low-pressure RF discharges," *Plasma Sources Sci. Technol.*, **1**, 36 (1992).

[64] V. A. Godyak, R. B. Piejak and B. M. Alexandrovich, "The electron-energy distribution function in a shielded argon radiofrequency inductive discharge," *Plasma Sources Sci. Technol.*, **4**, 332 (1995).

[65] S. V. Dudin and D. V. Rafalskyi, "A double-plasma source of continuous bipolar ion-ion beam," *Appl. Phys. Lett.*, **102**, 034102 (2013).

[66] N. Sato, H. Kobayashi, T. Tanabe, T. Ikehata and H. Mase, "Control of ion energy for low-damage plasma processing in RF discharge," *Japanese J. Appl. Phys.*, **34**, 2158 (1995).

[67] S. Uhm, K. H. Lee, H. Y. Chang and C. W. Chung, "On a dual inductively coupled plasma for direct and remote plasma in a reactor," *Phys. Plasmas*, **11**, 4830 (2004).

[68] K. R. MacKenzie, R. J. Taylor, D. Cohn, E. Ault and H. Ikezi, "Plasma electron heating by absorption of cold electrons," *Appl. Phys. Lett.*, **18**, 529 (1971).

[69] D. J. Economou, "Tailored ion energy distributions on plasma electrodes," *J. Vac. Sci. Technol A*, **31**, 050823 (2013).

[70] S. B. Wang and A. E. Wendt, "Ion bombardment energy and SiO_2/Si fluorocarbon plasma etch selectivity," *J. Vac. Sci. Technol A*, **19**, 2425 (2001).

[71] V. A. Godyak, "Electron energy distribution function control in gas discharge plasmas," *Phys. Plasmas*, **20**, 101611 (2013).

[72] S. Samukawa, Y. Nakagawa, T. Tsukada, H. Ueyama and K. Shinohara, "Low temperature, uniform, and high density plasma produced by a new ultra high frequency discharge with a spokewise antenna," *Appl. Phys. Lett.*, **67**, 1414 (1995).

[73] H. Shin, W. Zhu, D. J. Economou and V. M. Donnelly, "Ion energy distributions, electron temperatures, and electron densities in Ar, Kr, and Xe pulsed discharges," *J. Vac. Sci. Technol A*, **30**, 031304 (2012).

[74] A. Maresca, K. Orlov and U. Kortshagen, "Experimental study of diffusive cooling of electrons in a pulsed inductively coupled plasma," *Physical Review E*, **65**, 056405 (2002).

[75] M. A. Sobolewski, J. K. Olthoff and Y. Wang, "Ion energy distributions and sheath voltages in a radio-frequency-biased, inductively coupled, high-density plasma reactor ," *J. Appl. Phys.*, **85**, 3966 (1999).

[76] K. Kohler, D. E. Horne and J. W. Coburn, “Frequency dependence of ion bombardment of grounded surfaces in rf argon glow discharges in a planar system,” *J. Appl. Phys.*, **58**, 3350 (1985).

[77] A. D. Kuypers and H. J. Hopman, “Measurement of ion energy distributions at the powered rf electrode in a variable magnetic field,” *J. Appl. Phys.*, **67**, 1229 (1990).

[78] E. Kawamura, V. Vahedi, M. A. Lieberman and C. K. Birdsall, “Ion energy distributions in rf sheath; review, analysis and simulation,” *Plasma Sources Sci. Technol.*, **8**, R45 (1999).

[79] J. R. Woodworth, I. C. Abraham, M. E. Riley, P. A. Miller, T. W. Hamilton, B. P. Aragon, R. J. Shul and C. G. Willison, “Ion energy distributions at rf-biased wafer surfaces,” *J. Vac. Sci. Technol. A*, **20**, 873 (2002).

[80] D. Gahan, B. Dolinaj and M. B. Hopkins, “Retarding field analyzer for ion energy distribution measurements at a radio-frequency biased electrode,” *Rev. Sci. Instrum.*, **79**, 033502 (2008).

[81] A. Metze, D. W. Ernie and H. J. Oskam, “The energy distribution of ions bombarding electrode surfaces in rf plasma reactors,” *J. Appl. Phys.*, **65**, 993 (1989).

[82] U. Kortshagen and M. Zethoff, “Ion energy distribution functions in a planar inductively coupled RF discharge ,” *Plasma Sources Sci. Technol.*, **4**, 541 (1995).

[83] A. Agarwal, P. J. Stout, S. Banna, S. Rauf and K. Collins, "Recouping etch rates in pulsed inductively coupled plasmas," *J. Vac. Sci. Technol A*, **29**, 011017 (2011).

[84] O. Zabeida, A. Hallil, M. R. Wertheimer and L. Martinu, "Time-resolved measurements of ion energy distributions in dual-mode pulsed-microwave/radio frequency plasma," *J. Appl. Phys.*, **88**, 635 (2000).

[85] B. A. Smith and L. J. Overzet, "Ion energy control in an insulating inductively coupled discharge reactor," *Appl. Phys. Lett.*, **70**, 1950 (1997).

[86] J. W. Coburn and E. Kay, "Positive-ion bombardment of substrates in rf diode glow discharge sputtering," *J. Appl. Phys.*, **43** 4965 (1972).

[87] S. Panda, D. J. Economou and L. Chen, "Anisotropic etching of polymer films by high energy (~100s of eV) oxygen atom neutral beams ," *J. Vac. Sci. Technol. A*, **19**, 398 (2001).

[88] L. Xu, D. J. Economou, V. M. Donnelly and P. Ruchhoeft, "Extraction of a nearly monoenergetic ion beam using a pulsed plasma," *Appl. Phys. Lett.*, **87**, (2005).

[89] S. Hyungjoo, Z. Weiye, X. Lin, M. D. Vincent and J. E. Demetre, "Control of ion energy distributions using a pulsed plasma with synchronous bias on a boundary electrode," *Plasma Sources Sci. Technol.*, **20**, 055001 (2011).

[90] P. Diomede, D. J. Economou and V. M. Donnelly, "Rapid calculation of the ion energy distribution on a plasma electrode," *J. Appl. Phys.*, **111**, 123306 (2012).

[91] S. Ashida, C. Lee and M. A. Lieberman, “Spatially averaged (global) model of time modulated high density argon plasmas,” *J. Vac. Sci. Technol A*, **13**, 2498 (1995).

[92] D. P. Lymberopoulos, V. I. Kolobov and D. J. Economou, “Fluid simulation of a pulsed-power inductively coupled argon plasma,” *J. Vac. Sci. Technol A*, **16**, 564 (1998).

[93] P. Subramonium and M. J. Kushner, “Two-dimensional modeling of long-term transients in inductively coupled plasmas using moderate computational parallelism. I. Ar pulsed plasmas,” *J. Vac. Sci. Technol A*, **20**, 313 (2002).

[94] P. Subramonium and M. J. Kushner, “Pulsed plasmas as a method to improve uniformity during materials processing,” *J. Appl. Phys.*, **96**, 82 (2004).

[95] M. A. Lieberman and S. Ashida, “Global models of pulse-power-modulated high-density, low-pressure discharges,” *Plasma Sources Sci. Technol.*, **5**, 145 (1996).

[96] S. Behle, A. Brockhaus and J. Engemann, “Time-resolved investigations of pulsed microwave excited plasmas,” *Plasma Sources Sci. Technol.*, **9**, 57 (2000).

[97] H. Sugai, K. Nakamura, Y. Hikosaka and M. Nakamura, “Diagnostics and control of radicals in an inductively coupled etching reactor,” *J. Vac. Sci. Technol A*, **13**, 887 (1995).

[98] G. A. Hebner and C. B. Fleddermann, "Characterization of pulse-modulated inductively coupled plasmas in argon and chlorine," *J. Appl. Phys.*, **82**, 2814 (1997).

[99] M. Vikas and J. E. Demetre, "Spatio-temporal evolution of a pulsed chlorine discharge," *Plasma Sources Sci. Technol.*, **9**, 256 (2000).

[100] G. L. Rogoff, "Ambipolar diffusion coefficients for discharges in attaching gases," *J. Phys. D: Appl. Phys.*, **18**, 1533 (1985).

[101] J. T. Verdeyen, J. Beberman and L. Overzet, "Modulated discharges - effect on plasma parameters and deposition," *J. Vac. Sci. Technol A-Vacuum Surfaces and Films*, **8**, 1851 (1990).

[102] C. Grabowski and J. M. Gahl, "Pulse-modulated microwave plasma etching," *J. Appl. Phys.*, **70**, 1039 (1991).

[103] B. Ramamurthi and D. J. Economou, "Two-dimensional pulsed-plasma simulation of a chlorine discharge," *J. Vac. Sci. Technol A-Vacuum Surfaces and Films*, **20**, 467 (2002).

[104] L. J. Overzet, Y. Lin and L. Z. Luo, "Modeling and measurements of the negative-ion flux from amplitude modulated rf discharges," *J. Appl. Phys.*, **72**, 5579 (1992).

[105] S. Banna, A. Agarwal, G. Cunge, M. Darnon, E. Pargon and O. Joubert, "Pulsed high-density plasmas for advanced dry etching processes," *J. Vac. Sci. Technol A*, **30**, (2012).

[106] M. V. Malyshev, V. M. Donnelly, J. I. Colonell and S. Samukawa, "Dynamics of pulsed-power chlorine plasmas," *J. Appl. Phys.*, **86**, 4813 (1999).

[107] I. D. Kaganovich, B. N. Ramamurthi and D. J. Economou, "Self-trapping of negative ions due to electron detachment in the afterglow of electronegative gas plasmas," *Appl. Phys. Lett.*, **76**, 2844 (2000).

[108] T. H. Ahn, K. Nakamura and H. Sugai, "Negative ion measurements and etching in a pulsed-power inductively coupled plasma in chlorine," *Plasma Sources Sci. Technol.*, **5**, 139 (1996).

[109] S. K. Kanakasabapathy, L. J. Overzet, V. Midha and D. Economou, "Alternating fluxes of positive and negative ions from an ion-ion plasma," *Appl. Phys. Lett.*, **78**, 22 (2001).

[110] M. Tetsu and S. Seiji, "Time variation of plasma properties in a pulse-time-modulated electron cyclotron resonance discharge of chlorine gas," *Japanese J. Appl. Phys.*, **34**, L1079 (1995).

[111] Y. Ayumi, O. Hiroto and S. Seiji, "Simulation of a pulse time-modulated bulk plasma in Cl_2," *Japanese J. Appl. Phys.*, **35**, 2433 (1996).

[112] B. Ramamurthi and D. J. Economou, "Two-dimensional pulsed-plasma simulation of a chlorine discharge," *J. Vac. Sci. Technol A*, **20**, 467 (2002).

[113] P. Subramonium and M. J. Kushner, "Pulsed inductively coupled chlorine plasmas in the presence of a substrate bias," *Appl. Phys. Lett.*, **79**, 2145 (2001).

[114] E. G. Thorsteinsson and J. T. Gudmundsson, "A global (volume averaged) model of a Cl_2/Ar discharge: II. Pulsed power modulation," *J. Phys. D: Appl. Phys.*, **43**, 115202 (2010).

[115] M. Meyyappan, "Analysis of pulse time-modulated high-density discharges," *J. Vac. Sci. Technol A*, **14**, 2122 (1996).

[116] A. Sumio and A. L. Michael "Spatially averaged (global) model of time modulated high density chlorine plasmas," *Japanese J. Appl. Phys.*, **36**, 854 (1997).

[117] R. W. Boswell and D. Vender, "Simulation of pulsed electropositive and electronegative plasmas," *IEEE Transactions on Plasma Science*, **19**, 141 (1991).

[118] M. Meyyappan, "Modeling of a pulsed power SF_6 plasma," *Japanese J. Appl. Phys.*, **36**, 4820 (1997).

[119] D. Hayashi and K. Kadota, "Measurements of negative ion density in high-density oxygen plasmas by probe-assisted laser," *J. Appl. Phys.*, **83**, 697 (1998).

[120] H. M. Katsch, C. Manthey and H. F. Döbele, "Charge carrier dynamics in a pulsed inductive rf discharge in oxygen," *Plasma Sources Sci. Technol.*, **12**, 475 (2003).

[121] S. Panda, D. J. Economou and M. Meyyappan, "Effect of metastable oxygen molecules in high density power-modulated oxygen discharges," *J. Appl. Phys.*, **87**, 8323 (2000).

[122] S. Kim, M. A. Lieberman, A. J. Lichtenberg and J. T. Gudmundsson, "Improved volume-averaged model for steady and pulsed-power electronegative discharges," *J. Vac. Sci. Technol A*, **24**, 2025 (2006).

[123] M. Edamura, E. C. Benck and Y. Wang, "Time-resolved measurements of the E-to-H mode transition in electronegative pulse-modulated inductively coupled plasmas," *J. Vac. Sci. Technol A*, **24**, 2151 (2006).

[124] I. D. Kaganovich, D. J. Economou, B. N. Ramamurthi and V. Midha, "Negative Ion Density Fronts during Ignition and Extinction of Plasmas in Electronegative Gases," *Physical Review Letters*, **84**, 1918 (2000).

[125] I. D. Kaganovich, B. N. Ramamurthi and D. J. Economou, "Spatiotemporal dynamics of charged species in the afterglow of plasmas containing negative ions," *Physical Review E*, **64**, 036402 (2001).

[126] S. Samukawa and S. Furuoya, "Time-modulated electron-cyclotron-resonance plasma discharge for controlling generation of reactive species," *Appl. Phys. Lett.*, **63**, 2044 (1993).

[127] S. Samukawa and K. Terada, “Pulse-time modulated electron-cyclotron-resonance plasma-etching for highly selective, highly anisotropic, and less-charging polycrystalline silicon patterning,” *Journal of Vacuum Science & Technology B*, **12**, 3300 (1994).

[128] H. Ohtake and S. Samukawa, “Charge-free etching process using positive and negative ions in pulse-time modulated electron cyclotron resonance plasma with low-frequency bias,” *Appl. Phys. Lett.*, **68**, 2416 (1996).

[129] S. Samukawa, “Pulse-time-modulated electron cyclotron resonance plasma etching with low radio-frequency substrate bias,” *Appl. Phys. Lett.*, **68**, 316 (1996).

[130] P. Chabert, A. J. Lichtenberg, M. A. Lieberman and A. M. Marakhtanov, “Instabilities in low-pressure electronegative inductive discharges,” *Plasma Sources Sci. Technol.*, **10**, 478 (2001).

[131] S. Samukawa, H. Ohtake and T. Mieno, “Pulse-time-modulated electron cyclotron resonance plasma discharge for highly selective, highly anisotropic, and charge-free etching,” *J. Vac. Sci. Technol A-Vacuum Surfaces and Films*, **14**, 3049 (1996).

[132] S. Samukawa, H. Ohtake and T. Mieno, “Pulse-time-modulated ECR plasma discharge for highly selective, highly anisotropic and charge-free etching,” *Nec Research & Development*, **37**, 179 (1996).

[133] T. Mukai, H. Hada, S. Tahara, H. Yoda and S. Samukawa, “High-performance and damage-free magnetic film etching using pulse-time-modulated Cl_2 plasma,”

Japanese J. Appl. Phys. Part 1-Regular Papers Brief Communications & Review Papers, **45**, 5542 (2006).

[134] T. Mukai, N. Hshirna, H. Hada and S. Samukawa, “Reactive and anisotropic etching of magnetic tunnel junction films using pulse-time-modulated plasma,” *J. Vac. Sci. Technol A*, **25**, 432 (2007).

[135] T. Mieno and S. Samukawa, “Time-variation of plasma properties in a pulse-time-modulated electron-cyclotron-resonance discharge of chlorine gas,” *Japanese J. Appl. Phys. Part 2-Letters*, **34**, L1079 (1995).

[136] C. Steinbrüchel, “A new method for analyzing Langmuir probe data and the determination of ion densities and etch yields in an etching plasma,” *J. Vac. Sci. Technol. A*, **8**, 1663 (1990).

[137] T. H. Ahn, K. Nakamura and H. Sugai, “Negative ion measurements and etching in a pulsed-power inductively coupled plasma in chlorine,” *Plasma Sources Sci. Technol.*, **5**, 139 (1996).

[138] S. Samukawa and T. Mieno, “Pulse-time modulated plasma discharge for highly selective, highly anisotropic and charge-free etching,” *Plasma Sources Sci. Technol.*, **5**, 132 (1996).

[139] S. Seiji, “Time-Modulated Electron Cyclotron Resonance Plasma Discharge for Controlling the Polymerization in SiO 2 Etching,” *Japanese J. Appl. Phys.*, **32**, 6080 (1993).

[140] H. Sugai, K. Nakamura, Y. Hikosaka and M. Nakamura, “Diagnostics and Control of Radicals in an Inductively-Coupled Etching Reactor,” *J. Vac. Sci. Technol A-Vacuum Surfaces and Films*, **13**, 887 (1995).

[141] M. Jun, M. Kazunobu and M. Toshiaki, “Effect of aspect ratio on topographic dependent charging in oxide etching,” *J. Phys. D: Appl. Phys.*, **34**, 2950 (2001).

[142] K. Nojiri and K. Tsunokuni, “Study of gate oxide breakdown caused by charge buildup during dry etching,” *Journal of Vacuum Science & Technology B*, **11**, 1819 (1993).

[143] R. A. Gottscho, C. W. Jurgensen and D. J. Vitkavage, “Microscopic uniformity in plasma etching ,” *J. Vac. Sci. Technol. B*, **10**, 2133 (1992).

[144] S. Seiji and M. Tetsu, “Pulse-time modulated plasma discharge for highly selective, highly anisotropic and charge-free etching,” *Plasma Sources Sci. Technol.*, **5**, 132 (1996).

[145] S. Samukawa, H. Ohtake and T. Mieno, “ Pulse time modulated electron cyclotron resonance plasma discharge for highly selective, highly anisotropic, and charge free etching,” *J. Vac. Sci. Technol A*, **14**, 3049 (1996).

[146] S. Samukawa, “ Pulse time modulated electron cyclotron resonance plasma etching with low radio frequency substrate bias,” *Appl. Phys. Lett.*, **68**, 316 (1996).

[147] M. Takahiro, F. Nobuo, O. Satoshi and M. Hiroshi, "Reduction of charge build up with pulse modulated bias in pulsed electron cyclotron resonance plasma," *Japanese J. Appl. Phys.*, **37**, 2306 (1998).

[148] J. C. Arnold and H. H. Sawin, "Charging of pattern features during plasma etching," *J. Appl. Phys.*, **70**, 5314 (1991).

[149] D. J. Economou and R. C. Alkire, "Effect of potential field on ion deflection and shape evolution of trenches during plasma assisted etching," *Journal of The Electrochemical Society*, **135**, 941 (1988).

[150] P. Subramonium and M. J. Kushner, "Extraction of negative ions from pulsed electronegative inductively coupled plasmas having a radio-frequency substrate bias," *J. Vac. Sci. Technol A*, **22**, 534 (2004).

[151] S. Samukawa, "Pulse-time-modulated electron cyclotron resonance plasma etching with low radio-frequency," *Appl. Phys. Lett.*, **68**, 316 (1996).

[152] S. K. Kanakasabapathy, L. J. Overzet, V. Midha and D. Economou, "Alternating fluxes of positive and negative ions from an ion–ion plasma," *Appl. Phys. Lett.*, **78**, 22 (2001).

[153] T. Meguro, M. Hamagaki, S. Modaressi, T. Hara, Y. Aoyagi, M. Ishii and Y. Yamamoto, "Digital etching of GaAs: New approach of dry etching to atomic ordered processing," *Appl. Phys. Lett.*, **56**, 1552 (1990).

[154] P. A. Maki and D. J. Ehrlich, “Laser bilayer etching of GaAs surfaces,” *Appl. Phys. Lett.*, **55**, 91 (1989).

[155] S. Hiroyuki, I. Seiji, A. Kazushi, Y. Jirou, H. Masataka and H. Yasuhiro, “Atomic layer controlled digital etching of silicon,” *Japanese J. Appl. Phys.*, **29**, 2648 (1990).

[156] S. D. Athavale and D. J. Economou, “Realization of atomic layer etching of silicon,” *J. Vac. Sci. Technol B*, **14**, 3702 (1996).

[157] S. D. Athavale and D. J. Economou, “Molecular dynamics simulation of atomic layer etching of silicon,” *J. Vac. Sci. Technol A*, **13**, 966 (1995).

[158] S. D. Park, C. K. Oh, J. W. Bae, G. Y. Yeom, T. W. Kim, J. I. Song and J. H. Jang, “Atomic layer etching of InP using a low angle forward reflected Ne neutral beam,” *Appl. Phys. Lett.*, **89**, 043109 (2006).

[159] J. Guha, V. M. Donnelly and Y.-K. Pu, “Mass and Auger electron spectroscopy studies of the interactions of atomic and molecular chlorine on a plasma reactor wall,” *J. Appl. Phys.*, **103**, 013306 (2008).

[160] R. Khare, A. Srivastava and V. M. Donnelly, “Cl atom recombination on silicon oxy-chloride layers deposited on chamber walls in chlorine–oxygen plasmas,” *J. Vac. Sci. Technol A*, **30**, 051307 (2012).

[161] R. Khare, A. Srivastava and V. M. Donnelly, "Interactions of chlorine plasmas with silicon chloride-coated reactor walls during and after silicon etching," *J. Vac. Sci. Technol A*, **30**, 051306 (2012).

[162] S. Tan, W. Yang, K. J. Kanarik, T. Lill, V. Vahedi, J. Marks and R. A. Gottscho, "Highly selective directional atomic layer etching of silicon," *ECS Journal of Solid State Science and Technology*, **4**, N5010 (2015).

[163] D. Metzler, R. L. Bruce, S. Engelmann, E. A. Joseph and G. S. Oehrlein, "Fluorocarbon assisted atomic layer etching of SiO_2 using cyclic Ar/C_4F_8 plasma," *J. Vac. Sci. Technol A*, **32**, 020603 (2014).

[164] D. Metzler, C. Li, S. Engelmann, R. L. Bruce, E. A. Joseph and G. S. Oehrlein, "Fluorocarbon assisted atomic layer etching of SiO_2 and Si using cyclic Ar/C_4F_8 and Ar/CHF_3 plasma," *J. Vac. Sci. Technol A*, **34**, 01B101 (2016).

[165] Y. Wang, E. C. Benck, M. Misakian, M. Edamura and J. K. Olthoff, "Time-resolved measurements of ion energy distributions and optical emissions in pulsed radio-frequency discharges," *J. Appl. Phys.*, **87**, 2114 (2000).

[166] M. Tuszewski, "An electronegative inductive discharge instability," *J. Appl. Phys.*, **79**, 8967 (1996).

[167] M. A. Lieberman, A. J. Lichtenberg and A. M. Marakhtanov, "Instabilities in low-pressure inductive discharges with attaching gases," *Appl. Phys. Lett.*, **75**, 3617 (1999).

[168] E. Despiau-Pujo and P. Chabert, "Global model of instabilities in low-pressure inductive chlorine discharges," *Plasma Sources Sci. Technol.*, **18**, (2009).

[169] C. K. Kim and D. J. Economou, "Plasma molding over surface topography: energy and angular distribution of ions extractd out of large holes," *J. Appl. Phys.*, **91**, 2594 (2002).

[170] L. Liu, S. Sridhar, W. Zhu, V. M. Donnelly, D. J. Economou, M. D. Logue and M. J. Kushner, "External control of electron energy distributions in a dual tandem inductively coupled plasma," *J. Appl. Phys.*, **118**, 083303 (2015).

[171] J. Bredin, P. Chabert and A. Aanesland, "Langmuir probe analysis of highly electronegative plasmas," *Appl. Phys. Lett.*, **102**, 154107 (2013).

[172] W. R. Harshbarger, R. A. Porter, T. A. Miller and P. Norton, "A study of the optical emission from an rf plasma during semiconductor etching," *Applied Spectroscopy*, **31**, 201 (1977).

[173] B. A. Smith and L. J. Overzet, "Ion energy control in an insulating inductively coupled discharge reactor," *Appl. Phys. Lett.*, **70**, 1950 (1997).

[174] J. W. Coburn and E. Kay, "Positive ion bombardment of substrates in rf diode glow discharge sputtering," *J. Appl. Phys.*, **43**, 4965 (1972).

[175] S. Panda, D. J. Economou and L. Chen, "Anisotropic etching of polymer films by high energy (~100s of eV) oxygen atom neutral beams," *J. Vac. Sci. Technol A*, **19**, 398 (2001).

[176] I. M. El-Fayoumi, I. R. Jones and M. M. Turner, "Hysteresis in the E- to H-mode transition in a planar coil, inductively coupled rf argon discharge," *J. Phys. D: Appl. Phys.*, **31**, 3082 (1998).

[177] S. Langendorf and M. Walker, "Effect of secondary electron emission on the plasma sheath," *Phys. Plasmas*, **22**, 033515 (2015).

[178] D. L. Michael, S. Hyungjoo, Z. Weiye, X. Lin, M. D. Vincent, J. E. Demetre and J. K. Mark, "Ion energy distributions in inductively coupled plasmas having a biased boundary electrode," *Plasma Sources Sci. Technol.*, **21**, 065009 (2012).

[179] B. Ramamurthi and D. J. Economou, "Pulsed-power plasma reactors: two-dimensional electropositive discharge simulation in a GEC reference cell," *Plasma Sources Sci. Technol.*, **11**, 324 (2002).

[180] E. G. Thorsteinsson and J. T. Gudmundsson, "A global (volume averaged) model of a Cl_2 /Ar discharge: I. Continuous power," *J. Phys. D: Appl. Phys.*, **43**, 115201 (2010).

[181] C. Lee and M. A. Lieberman, "Global-Model of Ar, O_2, Cl_2, and Ar/O_2 High-Density Plasma Discharges," *J. Vac. Sci. Technol A-Vacuum Surfaces and Films*, **13**, 368 (1995).

[182] S. Ashida and M. A. Lieberman, "Spatially averaged (global) model of time modulated high density chlorine plasmas," *Japanese J. Appl. Phys. Part 1-Regular Papers Short Notes & Review Papers*, **36**, 854 (1997).

[183] L. Lei, S. Shyam, M. D. Vincent and J. E. Demetre, "Ignition delay of a pulsed inductively coupled plasma (ICP) in tandem with an auxiliary ICP," *J. Phys. D: Appl. Phys.*, **48**, 485201 (2015).

[184] E. G. Thorsteinsson and J. T. Gudmundsson, "A global (volume averaged) model of a chlorine discharge," *Plasma Sources Sci. Technol.*, **19**, 015001 (2010).

[185] G. H. Wannier, "Motion of Gaseous Ions in Strong Electric Fields," *Bell System Technical Journal*, **32**, 170 (1953).

[186] H. W. Ellis, R. Y. Pai, E. W. McDaniel, E. A. Mason and L. A. Viehland, "Transport properties of gaseous ions over a wide energy range," *Atomic Data and Nuclear Data Tables*, **17**, 177 (1976).

[187] H. W. Ellis, E. W. McDaniel, D. L. Albritton, L. A. Viehland, S. L. Lin and E. A. Mason, "Transport properties of gaseous ions over a wide energy range. Part II," *Atomic Data and Nuclear Data Tables*, **22**, 179 (1978).

[188] H. W. Ellis, M. G. Thackston, E. W. McDaniel and E. A. Mason, "Transport properties of gaseous ions over a wide energy range. Part III," *Atomic Data and Nuclear Data Tables*, **31**, 113 (1984).

[189] L. A. Viehland and E. A. Mason, "Transport properties of gaseous ions over a wide energy range IV," *Atomic Data and Nuclear Data Tables*, **60**, 37 (1995).

[190] D. J. Economou, "Fundamentals and applications of ion–ion plasmas," *Applied Surface Science*, **253**, 6672 (2007).

[191] S. G. Belostotsky, D. J. Economou, D. V. Lopaev and T. V. Rakhimova, "Negative ion destruction by O(3P) atoms and O_2 (a1Δg) molecules in an oxygen plasma," *Plasma Sources Sci. Technol.*, **14**, 532 (2005).

[192] M. Shibata, N. Nakano and T. Makabe, "Effect of O_2(a1Δg) on plasma structures in oxygen radio frequency discharges," *J. Appl. Phys.*, **80**, 6142 (1996).

[193] J. Bredin, P. Chabert and A. Aanesland, "Langmuir probe analysis in electronegative plasmas," *Phys. Plasmas*, **21**, 123502 (2014).

[194] J. Bredin, P. Chabert and A. Aanesland, "Langmuir probe analysis of highly electronegative plasmas," *Appl. Phys. Lett.*, **102**, 154107 (2013).

[195] A. Meige and R. W. Boswell, "Electron energy distribution functions in low-pressure inductively coupled bounded plasmas," *Phys. Plasmas*, **13**, 092104 (2006).

APPENDICES

Appendix A: Langmuir probe analysis for electronegative plasmas.

Langmuir probe analysis in Cl_2 plasmas employed in this work is based on a "fitting technique" which is proposed by Bredin et al. [193, 194] They used an analytical model to fit the I-V curves obtained by Langmuir probe, as well as their second derivatives above and below the plasma potential to obtain the temperatures and densities of the electrons and the positive and negative ions.

The total current collected by Langmuir probe is given by

$$I(V) = I_e(V) + I_+(V) + I_-(V), \tag{A.1}$$

where $I_e(V)$, $I_+(V)$, $I_-(V)$ is electron current, positive ion current and negative ion current, respectively. The currents depend on the probe voltage V and the expressions are different when the probe voltage is higher or lower than the plasma potential V_p.

For a probe voltage below V_p, electrons and negative ions are repelled by the probe. It is assumed that electron current $I_e(V)$ and negative current $I_-(V)$ follow Boltzmann relations

$$I_e(V) = \frac{eAn_e\bar{v}_e}{4} exp\left(\frac{V_p - V}{T_e}\right) \text{ and} \tag{A.2}$$

$$I_-(V) = I_-(V_p) exp\left(\frac{V_p - V}{T_-}\right), \tag{A.3}$$

where e is the elementary charge, $A = 2\pi la + 2\pi a^2$ is the area of probe surface, with α the probe radius and l the probe length, $\bar{v}_e = \sqrt{8eT_e/\pi m_e}$ is thermal velocity of electrons and $I_-(V_p)$ is the negative ion current at the plasma potential given by Equation A.10.

The positive ions are attracted by the probe and the positive ion current is assumed to be same as that at the sheath edge, by charge conservation:

$$I_+(V) = -h_r n_+ e u_{B+}^* S_{sh}(V), \tag{A.4}$$

where $h_r$is the ratio of the positive ion density at the sheath edge to the positive ion density in bulk plasma. It was calculated by Lieberman et al. [1, 181, 182] as

$$\mathrm{h_r} \approx \frac{1+\frac{3\alpha_s}{\gamma}}{1+\alpha_s} 0.80 \left\{4.0 + \frac{r}{\lambda} + \left(\frac{0.8 r u_{B+}^*}{2.405 J_1(2.405)\gamma D}\right)^2\right\}^{-\frac{1}{2}}, \tag{A.5}$$

where $\mathrm{D} = \mathrm{eT_i}\,\lambda/\mathrm{m}v$ is the diffusion coefficient. λ is the ion-neutral collision mean free path. v is the ion mean thermal velocity. S_{sh} is the probe effective collection area:

$$S_{sh} = 2\pi l r_{sh}(V) + 2\pi {r_{sh}}^2(V). \tag{A.6}$$

This area is different from the probe sheath because it is assumed that all the positive ions that reach the sheath will be collected by the probe. $r_{sh}(V) = s + a$ where s is the thickness of the sheath which can be calculated by a Child Law. Details of calculation of sheath thickness by Child Law will be discussed in Appendix B. u_{B+}^* is the modified Bohm speed by considering effect of negative ions for positive ions at the sheath edge.

$$u_{B+}^* = \sqrt{\frac{eT_e}{m_+}}\sqrt{\frac{1+\alpha_s}{1+\gamma\alpha_s}}, \tag{A.7}$$

where $\alpha_s = n_{Cl^-,s}/n_{e,s}$ where $n_{Cl^-,s}$ and $n_{e,s}$ are the negative ion and electron densities at the sheath edge, respectively. α_s is calculated by [1]

$$\alpha_b = \alpha_s \exp\left[\frac{(1+\alpha_s)(\gamma-1)}{2(1+\gamma\alpha_s)}\right], \tag{A.8}$$

where α_b is the bulk electronegativity and $\gamma = T_e/T_i$ is the ratio of electron temperature to ion temperature.

For a probe voltage above V_p, electrons and negative ions are attracted to the probe, while positive ions are repelled from the probe. The electron current is calculated by (give ref):

$$I_e(V) = n_e e A \bar{v}_e \sqrt{\frac{(V-V_p)/T_e}{\pi}} + n_e e A \frac{\bar{v}_e}{2} exp\left(\frac{V-V_p}{T_e}\right) erfc(\sqrt{\frac{V-V_p}{T_e}}). \quad \text{(A.9)}$$

The negative ion current is assumed to follow a Bohm relation and can be written as:[195]

$$I_{-}(V) = -h_r n_{-} e u_{B-}^{*} S_{sh}(V), \quad \text{(A.10)}$$

where $u_{B-}^{*} = \sqrt{eT_{+}/m_{-}}$, and $S_{sh}(V)$ remains the effective collection area for negative ions, which can be calculated by using Child Law but with the negative ion mass and temperature.

The positive ions are repelled from the probe and are assumed to follow a Boltzmann relation:

$$I_{+}(V) = I_{+}(V_p) exp\left(\frac{V-V_p}{T_{+}}\right), \quad \text{(A.11)}$$

where $I_{+}(\mathrm{V_p})$ is the current at the plasma potential given by Equation A.4.

This model allow us to calculate the theoretical I-V curve for given plamsa parameters such as n_e, n_+, n_-, T_e, T_+, T_-. On the other hand, By fitting the I-V curve and its second derivative, we can obtain these plasma parameters.

Figure A.1 shows an example of the fit for both the I-V characteristic and the second derivative. The I-V curve was obtained by Langmuir probe in the afterglow of

pulsed Cl_2 plasma. (t=260 μs in Figure 6.5) It can be seen that the measured curves and the corresponding fitted curve matches each other very well.

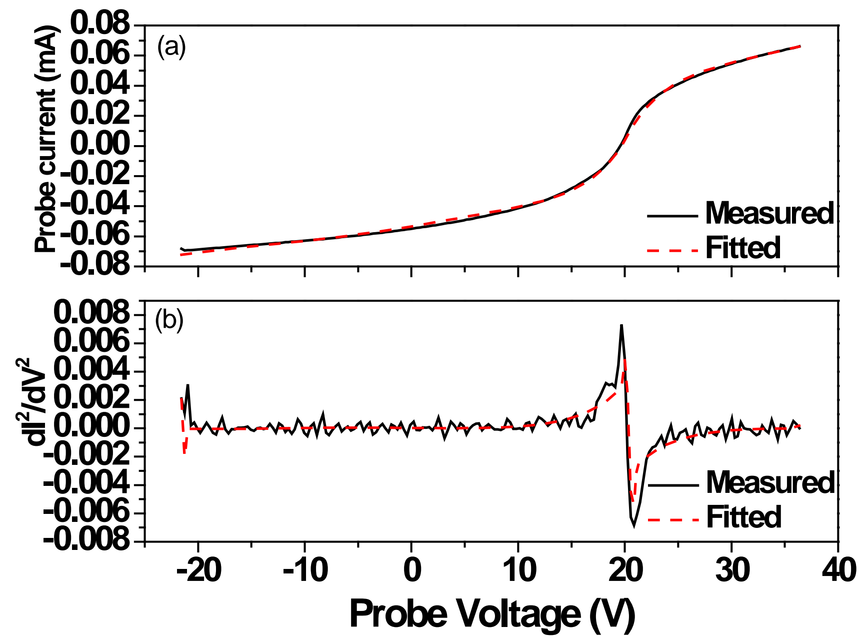

Figure A.1 Measured and fitted: (a) I-V characteristic, (b) its second derivative.

Appendix B: Child Law sheath model.

The sheath thickness as a function of voltage on the probe is calculated by a Child Law model in cylindrical coordinates [1, 193, 194]. The sheath edge is assumed to be located where then densities of ions $\mathrm{n}_s = h_r\, \mathrm{n}_0$, where n_s is the ions density at the sheath edge, h_r is the edge to center density ratio, and n_0 is the density in bulk plasma. At this location, ions have Bohm velocity $u(S_{sh}) = u_{B+}^*$,

The ion energy conservation gives:

$$\frac{1}{2} m_+ u^2(r) = -e\Phi(r) \text{ and} \tag{A.12}$$

$$J_0 = h_r neu_{B+}^* = en(r)u(r), \tag{A.13}$$

where J_0 is the ion current at sheath edge.

Solving for $n(r)$, we can get

$$n(r) = \frac{J_0}{e}\left(-\frac{2e\Phi(r)}{m_+}\right)^{-1/2}, \tag{A.14}$$

By using $E = -d\Phi/\mathrm{dr}$ and Gauss's Law yields:

$$\frac{\mathrm{d}^2\Phi}{d\mathrm{r}^2} = \frac{en(r)}{\varepsilon_0} - \frac{1}{r}\frac{d\Phi}{\mathrm{dr}}. \tag{A.15}$$

By using ion current continuity in the sheath, $rJ(r) = RJ_0$, and $J_0 = h_r neu_{B+}^*$, Equation A.15 can be written as

$$\frac{\mathrm{d}^2\Phi}{d\mathrm{r}^2} = \frac{RJ_0}{r\varepsilon_0 u(r)} - \frac{1}{r}\frac{d\Phi}{\mathrm{dr}}. \tag{A.16}$$

The boundary conditions are

$$\frac{d\Phi}{\mathrm{dr}} = -E = 0 \text{ at } \mathrm{r} = S_{sh} \text{ and} \tag{A.17}$$

$$\Phi = 0 \text{ at } \mathrm{r} = S_{sh}. \tag{A.18}$$

The numerical integration of Equation A.16 gives $S_{sh}(V)$.